Topics in Semiclassical Quantum Dynamics: Phase-Space Deformations, Energy Redistribution, and Vibrational Predissociation

A thesis presented

by

Emmanuel David Tannenbaum

to

The Department of Chemistry and Chemical Biology

in partial fulfillment of the requirements

for the degree of

Doctor of Philosophy

in the subject of

Chemical Physics

Harvard University

Cambridge, Massachusetts

May, 2002

Abstract – Topics in Semiclassical Quantum Dynamics: Phase-Space Deformations, Energy Redistribution, and Vibrational Predissociation

Emmanuel David Tannenbaum

May, 2002

Advisor: Eric J. Heller

This thesis covers three topics in semiclassical quantum dynamics. Chapters 1 and 2 are devoted to the development and application of a phase-space deformation approach to optimize the classical canonical representation of a nearly integrable Hamiltonian. Chapter 1 develops and tests the theory, while in Chapter 2 the method is successfully applied to several model Hamiltonians. Chapters 3 and 4 are devoted to studies of energy redistribution. Specifically, Chapter 3 compares dynamical tunneling to Arnol'd Diffusion in a model Hamiltonian system, in order to determine the relative importance of the two types of energy flow as a mechanism of vibrational energy redistribution in polyatomic molecules. It is concluded that dynamical tunneling is generally much faster than Arnol'd Diffusion. Chapter 4 studies an

analytically solvable stochastic model for energy dispersion due to numerous Landau-Zener transitions on a network of avoided crossings. Finally, Chapters 5 and 6 cover issues related to vibrational predissociation. In Chapter 5, a perturbative model for vibrational predissociation is developed and applied to ArHF. A number of important experimental observations regarding the ArHF system are recovered using our model. In Chapter 6 we develop a semiclassical coupling formula for bound-free dissociative couplings using only classical Fourier coefficients of the Hamiltonian. This formula is successfully applied to several test cases.

To my grandparents

Acknowledgments

Writing this thesis would not have been possible without the help of many people. First of all, I would like to thank my advisor, Rick Heller, for teaching me quantum mechanics and for always being a great source of ideas and new perspectives. I thank Bill Klemperer for the opportunity to collaborate with him on a project modelling vibrational predissociation of van der Waals complexes. The results of this work is the subject of Chapter 5 of this thesis. I also thank David Reichman for his various advice on science and other subjects.

I would also like to thank a number of friends who helped me get through graduate school: Mark Gudiksen, with whom I worked through the first semester of Rick's quantum mechanics, and Allison Kalben, who was my homework partner the second semester. Michael Sheehy, who has been a great roommate during my years here, and who, along with Mark and Katie Drake, was my homework partner in Eugene Shakhnovich's statistical mechanics class. I also thank my other roommates, Jeffrey Barton and Ha-Young Lee, who along with Michael, made our apartment a welcome place to come home to.

Rajiah Denny helped me with various facets of the Unix operating system, and gave me a great deal of help with preparing my papers (and this thesis) in LaTeX. Nikolai Dokholyan gave me very helpful advice regarding the search for postdoctoral positions, and he also gave me many useful tips on how to respond to referee criticisms when revising manuscripts. Anthony Yezzi, a professor in the Electrical and Computer Engineering Department of the Georgia Institute of Technology, gave me a number of helpful suggestions on the numerical implementation of some of the algorithms presented in the first two chapters of this thesis.

I also thank both former and current Heller group members for many helpful conversations and feedback on my work. In this vein, I especially would like to thank Doron Cohen, with whom I collaborated. The results of our collaboration may be found in Chapter 4 of this thesis. Also I would like to thank Scot Shaw and Alex Barnett for their help in dealing with computer problems, Jiri Vanicek, Areez Mody, and Troy von Voorhis for a number of helpful conversations regarding my research, and Robert Parrott for help in getting my papers and relevant programs onto the group website.

Yisroel Brumer deserves special mention, for not only is he one of the closest friends that I made during graduate school, but he also taught me

quite a bit about Judaism. During my years here, he helped me connect with my faith through our study sessions at the Harvard Hillel.

Other friends I would like to thank are David Rosmarin, Will Schoen, Jeff Urban, Jill Becker, John Krug, Guy Herzog, and (last but not least) Ravid Rovner. Your friendship during my time at Harvard helped me get through graduate school.

A special thank you goes to my parents, Allen and Rina. I would not be where I am today without all the advice and support they gave me. More than anyone else, they have helped keep me on a steady course through my life, and have shared with me the wisdom they gained through their various experiences.

Finally, I want to give a heartfelt thanks to my sister, Sarah, who is easily my best friend in the whole world, and has always been incredibly supportive through all my difficult periods. Anyone would be quite lucky to have a sibling like her.

Contents

List of Figures

List of Tables

Foreword

The research contained in this thesis originally grew out of a desire to better understand Intramolecular Vibrational Relaxation, or IVR, for short. It has been observed in high-resolution spectra of polyatomic molecules that apparently sharp, well-defined peaks (at lower resolutions) are in fact fractionated into thousands of smaller peaks within a narrow energy band. This fractionation is indicative of long-time dynamics within the polyatomic molecule, during which energy placed into an initial zeroth-order vibrational state flows into the other vibrational states of the polyatomic. An understanding of this energy flow is of interest to physical chemists, since the distribution of vibrational energy within a polyatomic molecule has a strong effect on chemical reaction rates.

Our IVR research led us to the issue of finding the appropriate zeroth-order basis from which to measure intramolecular vibrational energy flow. IVR is a basis-dependent notion, since in an appropriate basis, namely the eigenstates, there is no IVR at all. A natural basis, obtained from classical mechanics, consists of the semiclassical wavefunctions corresponding to the invariant tori of the full molecular vibrational Hamiltonian. We developed

a gradient-descent approach (GDA) to find the optimized basis of invariant tori with which to represent a nearly separable Hamiltonian. This allows the determination of energy spectra, within a given range, with a much smaller semiclassical basis than required with an initial zeroth-order representation (such as harmonic oscillators).

The GDA method was then generalized to include arbitrary canonical representations of phase space, and not just action-angle variables. It was also extended so that construction of the semiclassical wavefunctions associated with the optimized canonical basis was possible. This work falls under the category of phase-space deformations, and forms the first two chapters of this thesis.

We also sought to study the mechanism of energy flow between the invariant tori in vibrational dynamics problems. Specifically, we wished to determine whether dynamical tunneling, a quantum energy flow mechanism, or Arnol'd Diffusion, a classical energy flow mechanism, was the primary culprits leading to the fine peak splittings observed in IR spectra. In addition, the IVR work was also related to work by Brooks Pate of the University of Virginia, who was studying the deflection of molecules in external fields. It was believed that energy transfer due to Landau-Zener dynamics through a

network of avoided crossings could lead to deflection of larger molecules in electric fields. A desire to understand this energy flow mechanism led to a collaboration with Doron Cohen, then a post-doc under Rick Heller, in which we developed an analytically solvable stochastic model for energy dispersion due to numerous Landau-Zener transitions. These two subjects (dynamical tunneling vs. Arnol'd Diffusion and Landau-Zener dynamics) fall under the category of energy redistribution, and form Chapters 3 and 4 of this thesis.

Finally, another line of research that the IVR work took was a study of the vibrational predissociation of the van der Waals complex ArHF. This work was done in collaboration with Prof. Bill Klemperer and his group, here at Harvard. Our goal was to develop a quantum model for the predissociation dynamics which could predict the predissociation rates and rotational distribution of the outgoing HF. We managed to obtain rates which were within an order of magnitude or much better, in some cases, of those measured experimentally. We also managed to confirm the experimental observation that the product HF preferentially predissociates into the highest angular momentum state (j-state) accessible for the complex, which is j = 13. The main discrepancy between theory and experiment is that our rotational distribution is much more sharply peaked at j = 13 than the experimental distribution.

We also managed to develop a semiclassical coupling formula for bound-free dissociative couplings using only the classical Fourier coefficients of the Hamiltonian. This is a partial generalization of the bound-bound coupling formula using the Fourier coefficients of the Hamiltonian in an action-angle expansion. These two subjects fall under the category of vibrational predissociation, and form the last two chapters (5 and 6) of this thesis.

Chapter 1

A PDE-Based Approach to Classical Phase-Space Deformations

This chapter presents a PDE-based approach to finding an optimal canonical basis with which to represent a nearly integrable Hamiltonian. The idea behind the method is to continuously deform the initial canonical basis in such a way that the dependence of the Hamiltonian on the canonical position of the final basis is minimized. The final basis incorporates as much of the

classical dynamics as possible into an integrable Hamiltonian, leaving a much smaller non-integrable component than in the initial representation. With this approach it is also possible to construct the semiclassical wavefunctions corresponding to the final canonical basis. This optimized basis is potentially useful in quantum calculations, both as a way to minimize the required size of basis sets, and as a way to provide physical insight by isolating those effects resulting from integrable dynamics.

1.1 Introduction

Suppose we are given a nearly integrable Hamiltonian $H(\mathbf{q}, \mathbf{p})$, where $(\mathbf{q}, \mathbf{p})$ represents some canonical representation of phase space (not necessarily ordinary position and momentum). We wish to find another canonical representation $(\mathbf{Q}, \mathbf{P})$ in which H is as close as possible to being integrable. Our motivation for this is twofold, and is connected to semiclassical quantum mechanics: First of all, from a purely numerical perspective, a representation in which H is as close as possible to being integrable leads to an optimized semiclassical basis with which to perform quantum calculations. The reason for this is that we can associate with $\mathbf{P}$ a quantum state $|\mathbf{P}\rangle$. If we write

$H(\mathbf{Q},\mathbf{P}) = H^{(0)}(\mathbf{P}) + H^{(1)}(\mathbf{Q},\mathbf{P})$, then it is clear that $H^{(0)}$ is diagonal in the $\{|\mathbf{P}\rangle\}$ basis, so that only $H^{(1)}$ is available to couple the various basis states. The coupling is given semiclassically by [9],

$$\langle \mathbf{P}'|\hat{H}^{(1)}|\mathbf{P}\rangle = H^{(1)}_{\frac{\mathbf{P}'-\mathbf{P}}{2\pi\hbar}}(\frac{\mathbf{P}+\mathbf{P}'}{2}) \tag{1.1}$$

where $H^{(1)}_{\frac{\mathbf{P}'-\mathbf{P}}{2\pi\hbar}}(\frac{\mathbf{P}+\mathbf{P}'}{2})$ is the $\frac{\mathbf{P}'-\mathbf{P}}{2\pi\hbar}$ Fourier component at $\frac{\mathbf{P}+\mathbf{P}'}{2}$ of $H^{(1)}$. A representation in which $H^{(1)}$ is as small as possible will minimize the couplings in the corresponding $\{|\mathbf{P}\rangle\}$ basis, and thus will minimize the size of the basis required to perform a given calculation to some desired accuracy.

Secondly, a canonical representation in which H is as close as possible to being integrable provides physical insight. By incorporating as much of the classical dynamics as possible into an integrable Hamiltonian, this optimal canonical representation can help to isolate those classical and quantum effects resulting from integrable dynamics from those that do not. Thus this representation can isolate non-integrable quantum and classical effects such as dynamical tunneling and Arnol'd diffusion, respectively. Furthermore, we can also visualize the quantum manifestation of the integrable classical dynamics via the semiclassical prescription for constructing a wavefunction: Given the generating function $S(\mathbf{q},\mathbf{P})$ from the initial basis $(\mathbf{q},\mathbf{p})$ to the final

basis $(\mathbf{Q}, \mathbf{P})$, we have, up to normalization,

$$\langle \mathbf{q}|\mathbf{P}\rangle = |\det \frac{\partial^2 S}{\partial \mathbf{q} \partial \mathbf{P}}|^{\frac{1}{2}} \exp[iS/\hbar] \tag{1.2}$$

where $\det \frac{\partial^2 S}{\partial \mathbf{q} \partial \mathbf{P}}$ is the well-known Van Vleck determinant.

In the case of action-angle variables, the optimized representation of a nearly integrable Hamiltonian is termed an Intrinsic Resonance Representation (IRR), a term coined by Carioli, Heller, and Moller (CHM) [2, 3]. In 1997 they published a paper detailing an algorithm for the construction of such a representation. The idea behind the CHM algorithm is to eliminate all the non-resonant terms of the Hamiltonian via an appropriate canonical transformation. This canonical transformation is obtained via a modified Chapman, Garrett, and Miller (CGM) method [2, 3, 4], which is essentially a Newton-Raphson scheme to find the invariant tori with a desired set of actions for a nearly integrable system. The remaining resonant and near-resonant terms are then re-expressed in the new basis. It is impossible to reduce the angle dependence any further, since this would result in the formation of resonance zones, which prevents a global action-angle description of the Hamiltonian.

In 2001 the author published an alternative algorithm for finding the IRR

basis [2]. The method introduced is a PDE-based approach which continuously deforms the initial action-angle basis in such a way that the angle dependence of the Hamiltonian is continuously reduced. It amounts to a gradient-descent algorithm in the limit of a first-order perturbation, and was therefore called the GDA method. Formally, the method does not distinguish between resonant, nearly resonant, and non-resonant terms, that is, the evolution is performed on the entire Hamiltonian without any terms neglected. However, the evolution is such that the more non-resonant a term, the more strongly it is affected by the evolution. Thus, the non-resonant terms of the Hamiltonian are essentially killed off, the nearly resonant terms are reduced somewhat, while the resonant terms are essentially unaffected. In Ref. 2, the GDA method was used to semiclassically find the eigenvalues of 2, 4, and 6 degree-of-freedom systems, using greatly reduced basis sets.

The GDA method circumvents two main drawbacks of the CHM method. First, the CHM method requires an a priori decision as to which terms are resonant and non-resonant. This leads to an ambiguity in the case of near-resonances. It could happen that a given term in the Hamiltonian must be considered resonant in order to get the Newton-Raphson scheme to converge. This leads to a somewhat artificial cutoff criterion, since a nearly resonant

Fourier component should in principle still be reduced as much as possible, though not necessarily completely. Thus, unless the Hamiltonian has a few exact or near-resonances, it is not clear that the CHM method will give the optimized torus basis.

Second, the CHM method requires the numerical evaluation of multidimensional integrals, and the numerical inversion of a nonlinear angle map at every iteration step. Furthermore, every iteration step also requires the numerical solution of a system of linear equations. These numerical calculations slow the algorithm down. In contrast, the numerical calculations required by the GDA method are much simpler, so we believe that the GDA method is faster than the CHM approach (though in fairness it should be added that no direct speed comparisons have been made to date).

Despite its advantages, the GDA method, as described in Ref. 2, is limited to systems describable by action-angle variables. Furthermore, while the method generates the representation of the Hamiltonian in the final action-angle basis, it does not give the overall generating function $S(\mathbf{q}, \mathbf{P})$, transforming from the initial $(\mathbf{q}, \mathbf{p})$ basis to the final $(\mathbf{Q}, \mathbf{P})$ basis. Thus, we could compute the energy spectrum arising from an optimized invariant torus basis, but not the corresponding semiclassical wavefunctions "living" on the IRR

tori.

This chapter is a continuation of the work presented in Ref. 2 (and in Chapter 2), and it has several purposes: First, the presentation of the method given in Ref. 2 has been greatly simplified, and generalized to include arbitrary canonical representations of phase space. Secondly, and more importantly, the method has been extended to include the determination of the overall generating function $S(\mathbf{q}, \mathbf{P})$. This provides a powerful visualization tool which allows one to actually construct the semiclassical wavefunctions associated with the optimized canonical basis. Thus, while the full method will be developed in this chapter, the numerical examples focus on the overall generating function $S(\mathbf{q}, \mathbf{P})$. As mentioned before, numerical examples dealing with the Hamiltonian directly may be found in Ref. 2 (or in Chapter 2 of this thesis).

This chapter is organized as follows: In Section 1.2 we derive the generic evolution equations for the Hamiltonian and the overall generating function, starting from an arbitrary canonical basis $(\mathbf{q}, \mathbf{p})$. In Section 1.3 we consider the case of a nearly integrable Hamiltonian, and obtain the specific form our evolution is to take if we want to optimize the canonical basis used to represent the Hamiltonian. In Section 1.4 we consider the first-order limit of our

PDE approach. We obtain a generalized first-order classical perturbation theory which coincides with standard perturbation theory in an appropriate limit, obtained by taking the evolution parameter to ∞. However, the advantage of our first-order formula is that it remains convergent for all finite values of the evolution parameter, only possibly diverging as a result of near resonances in the limit to ∞. In Section 1.5 we work some analytical examples. In particular, we show that one-dimensional above-barrier WKB theory is contained within our PDE-based approach. Section 1.6 tests the S evolution equation with a numerical example. We continue in Section 1.7 by applying the S evolution equation to actually construct and visualize some semiclassical wavefunctions associated with optimized canonical bases. Finally, we conclude in Section 1.8 with a summary of our results and a discussion of future research plans.

1.2 The Evolution Equations

In this section we shall derive the basic evolution equations for the Hamiltonian H and the overall generating function S. The idea is as follows: We start with an initial set of canonical coordinates $(\mathbf{q}, \mathbf{p})$, which denote any global

representation of phase space, and do not necessarily refer to ordinary position and momentum, respectively (non-global representations can also work, as long as we remain well within the region of phase space they describe. An example of this is action-angle variables for a system which can dissociate. Action-angle variables should work as a valid representation as long as we remain well below any dissociation threshold). We continuously deform this system via a series of infinitesimal generating functions. The result is that our canonical representation is evolving with time, and is denoted by $(\mathbf{Q}_t, \mathbf{P}_t)$ at time t. As our canonical pair evolves, the functional dependence of H on the canonical pair changes. In addition, the overall generating function $S(\mathbf{q}, \mathbf{P}; t)$ connecting the initial $(\mathbf{q}, \mathbf{p})$ to the current $(\mathbf{Q}_t, \mathbf{P}_t)$ evolves as well. In subsection 1.2.1, we derive the PDE governing the evolution of H generated by this phase space deformation. In subsection 1.2.2, we derive the PDE governing the evolution of S.

Before continuing, it should be pointed out that t does not refer to time in the ordinary sense, but is rather a deformation or homotopy parameter. In fact, for the specific form of our PDE-based approach (which will be presented in Section 1.3), it may be shown that t has units of $[Time]^2$.

1.2.1 Evolution of the Hamiltonian

Consider an arbitrary set of canonical coordinates. At time t, we're at system $(\mathbf{Q}_t, \mathbf{P}_t)$. At time $t + dt$, we're at system $(\mathbf{Q}_{t+dt}, \mathbf{P}_{t+dt})$. These are connected by an infinitesimal generating function $F(\mathbf{Q}_t, \mathbf{P}_{t+dt}; t) = \mathbf{Q}_t \cdot \mathbf{P}_{t+dt} + dtG(\mathbf{Q}_t, \mathbf{P}_{t+dt}; t)$. Therefore,

$$\mathbf{Q}_{t+dt} = \mathbf{Q}_t + dt\nabla_{\mathbf{P}} G(\mathbf{Q}_t, \mathbf{P}_{t+dt}; t) \tag{1.3}$$

$$\mathbf{P}_t = \mathbf{P}_{t+dt} + dt\nabla_{\mathbf{Q}} G(\mathbf{Q}_t, \mathbf{P}_{t+dt}; t) \tag{1.4}$$

so to first-order, we obtain,

$$\mathbf{Q}_t = \mathbf{Q}_{t+dt} - dt\nabla_{\mathbf{P}} G(\mathbf{Q}_{t+dt}, \mathbf{P}_{t+dt}; t) \tag{1.5}$$

$$\mathbf{P}_t = \mathbf{P}_{t+dt} + dt\nabla_{\mathbf{Q}} G(\mathbf{Q}_{t+dt}, \mathbf{P}_{t+dt}; t) \tag{1.6}$$

The Hamiltonian at time $t + dt$ is therefore related to the Hamiltonian at time t via,

$$\begin{aligned} H(\mathbf{Q}_{t+dt}, \mathbf{P}_{t+dt}; t + dt) &= H(\mathbf{Q}_t, \mathbf{P}_t; t) \\ &= H(\mathbf{Q}_{t+dt} - dt\nabla_{\mathbf{P}} G(\mathbf{Q}_{t+dt}, \mathbf{P}_{t+dt}; t), \mathbf{P}_{t+dt} + \\ &\quad dt\nabla_{\mathbf{Q}} G(\mathbf{Q}_{t+dt}, \mathbf{P}_{t+dt}; t); t) \\ &= H(\mathbf{Q}_{t+dt}, \mathbf{P}_{t+dt}; t) + dt(\nabla_{\mathbf{P}} H \cdot \nabla_{\mathbf{Q}} G - \\ &\quad \nabla_{\mathbf{Q}} H \cdot \nabla_{\mathbf{P}} G) \end{aligned} \tag{1.7}$$

and so,

$$\frac{\partial H}{\partial t} = \nabla_{\mathbf{P}} H \cdot \nabla_{\mathbf{Q}} G - \nabla_{\mathbf{Q}} H \cdot \nabla_{\mathbf{P}} G = -\{H, G\} \tag{1.8}$$

which can be re-written as,

$$\frac{\partial H}{\partial t} + \{H, G\} = 0 \tag{1.9}$$

Thus, this evolution generates a one-parameter family $\{H(\mathbf{Q}, \mathbf{P}; t)\}$ of Hamiltonians, whose evolution under the action of the infinitesimal generating functions $G(\mathbf{Q}, \mathbf{P}; t)$ is given by the previous equation (Eq. (1.9)). It should also be pointed out that Eq. (1.9) is nothing more than the statement that H is invariant under the canonical transformation induced by F ($dH/dt = 0$), which follows from the fact that F is a time-independent canonical transformation [27].

For what follows in this chapter it will prove convenient to represent the dynamics in Fourier space. To this end, assume that H is periodic in each Q_i with period L_i. Then we shall choose G to also be periodic in each Q_i with period L_i. Define $V = L_1 \cdots L_D$, and let Ω denote an arbitrary D-dimensional box of side lengths $L_1, \ldots, L_D$. Then,

$$H(\mathbf{Q}, \mathbf{P}; t) = \frac{1}{V} \sum_{\mathbf{k}} H_{\mathbf{k}}(\mathbf{P}; t) e^{2\pi i \mathbf{k} \cdot \mathbf{Q}} \tag{1.10}$$

where

$$H_{\mathbf{k}}(\mathbf{P};t) \equiv \int_{\Omega} d\mathbf{Q} H(\mathbf{Q},\mathbf{P};t) e^{-2\pi i \mathbf{k}\cdot\mathbf{Q}} \tag{1.11}$$

and similarly for $G(\mathbf{Q},\mathbf{P};t)$.

The full evolution done component-wise gives,

$$\begin{aligned} \frac{1}{V}\sum_{\mathbf{k}} \frac{\partial H_{\mathbf{k}}}{\partial t} e^{2\pi i \mathbf{k}\cdot\mathbf{Q}} &= \frac{1}{V^2}\Big(\sum_{\mathbf{k}'} \nabla_{\mathbf{P}} H_{\mathbf{k}'} e^{2\pi i \mathbf{k}'\cdot\mathbf{Q}} \cdot 2\pi i \sum_{\mathbf{k}''} \mathbf{k}'' G_{\mathbf{k}''} e^{2\pi i \mathbf{k}''\cdot\mathbf{Q}} - \\ &\qquad 2\pi i \sum_{\mathbf{k}'} \mathbf{k}' H_{\mathbf{k}'} e^{2\pi i \mathbf{k}'\cdot\mathbf{Q}} \cdot \sum_{\mathbf{k}''} \nabla_{\mathbf{P}} G_{\mathbf{k}''} e^{2\pi i \mathbf{k}''\cdot\mathbf{Q}}\Big) \end{aligned} \tag{1.12}$$

which gives,

$$\begin{aligned} \sum_{\mathbf{k}} \frac{\partial H_{\mathbf{k}}}{\partial t} e^{2\pi i \mathbf{k}\cdot\mathbf{Q}} &= \frac{2\pi i}{V} \sum_{\mathbf{k}',\mathbf{k}''} [(\mathbf{k}''\cdot\nabla_{\mathbf{P}} H_{\mathbf{k}'}) G_{\mathbf{k}''} - (\mathbf{k}'\cdot\nabla_{\mathbf{P}} G_{\mathbf{k}''}) H_{\mathbf{k}'}] e^{2\pi i(\mathbf{k}'+\mathbf{k}'')\cdot\mathbf{Q}} \\ &= \frac{2\pi i}{V} \sum_{\mathbf{k}} \sum_{\mathbf{k}'} [(\mathbf{k}'\cdot\nabla_{\mathbf{P}} H_{\mathbf{k}-\mathbf{k}'}) G_{\mathbf{k}'} - \\ &\qquad ((\mathbf{k}-\mathbf{k}')\cdot\nabla_{\mathbf{P}} G_{\mathbf{k}'}) H_{\mathbf{k}-\mathbf{k}'}] e^{2\pi i \mathbf{k}\cdot\mathbf{Q}} \end{aligned} \tag{1.13}$$

Our component-wise evolution is therefore,

$$\frac{\partial H_{\mathbf{k}}}{\partial t} = 2\pi i \frac{1}{V} \sum_{\mathbf{k}'} [(\mathbf{k}'\cdot\nabla_{\mathbf{P}} H_{\mathbf{k}-\mathbf{k}'}) G_{\mathbf{k}'} - ((\mathbf{k}-\mathbf{k}')\cdot\nabla_{\mathbf{P}} G_{\mathbf{k}'}) H_{\mathbf{k}-\mathbf{k}'}] \tag{1.14}$$

Note that the evolution preserves the integration limits of our original system. Thus the topology of the original phase space is preserved.

As a final note for this subsection, it should be mentioned that degrees of freedom for which L_i is finite can be treated in an action-angle formalism

in which $L_i = 1$, while degrees of freedom for which $L_i = \infty$ have their corresponding Fourier sums replaced by integrals.

1.2.2 Evolution of the Generating Function

The above treatment tells us how the Hamiltonian evolves under the action of the infinitesimal generating functions, but it tells us nothing of the evolution of $S(\mathbf{q}, \mathbf{P}; t)$, the overall generating function from the initial system $(\mathbf{q}, \mathbf{p})$ to $(\mathbf{Q}_t, \mathbf{P}_t)$. We shall deal with this now.

At time t, our generating function is $S(\mathbf{q}, \mathbf{P}; t)$, taking us from $(\mathbf{q}, \mathbf{p})$ to $(\mathbf{Q}_t, \mathbf{P}_t)$. At time $t + dt$, our generating function is $S(\mathbf{q}, \mathbf{P}; t + dt)$, taking us from $(\mathbf{q}, \mathbf{p})$ to $(\mathbf{Q}_{t+dt}, \mathbf{P}_{t+dt})$. We know that $(\mathbf{Q}_t, \mathbf{P}_t)$ and $(\mathbf{Q}_{t+dt}, \mathbf{P}_{t+dt})$ are connected by an infinitesimal generating function $\mathbf{Q}_t \cdot \mathbf{P}_{t+dt} + dtG(\mathbf{Q}_t, \mathbf{P}_{t+dt}; t)$. We must have,

$$\mathbf{p} = \frac{\partial S}{\partial \mathbf{q}}(\mathbf{q}, \mathbf{P}_t; t) = \frac{\partial S}{\partial \mathbf{q}}(\mathbf{q}, \mathbf{P}_{t+dt}; t + dt) \tag{1.15}$$

Now,

$$\begin{aligned} \frac{\partial S}{\partial \mathbf{q}}(\mathbf{q}, \mathbf{P}_t; t) &= \frac{\partial S}{\partial \mathbf{q}}(\mathbf{q}, \mathbf{P}_{t+dt} + dt\frac{\partial G}{\partial \mathbf{Q}}(\mathbf{Q}_t, \mathbf{P}_{t+dt}; t); t) \\ &= \frac{\partial S}{\partial \mathbf{q}}(\mathbf{q}, \mathbf{P}_{t+dt}; t) + \frac{\partial^2 S}{\partial \mathbf{P} \partial \mathbf{q}}(\mathbf{q}, \mathbf{P}_{t+dt}; t) \cdot \frac{\partial G}{\partial \mathbf{Q}}(\mathbf{Q}_t, \mathbf{P}_{t+dt}; t) dt \end{aligned}$$

$$
\begin{aligned}
&= \frac{\partial S}{\partial \mathbf{q}}(\mathbf{q}, \mathbf{P}_{t+dt}; t) + \frac{\partial G}{\partial \mathbf{Q}}(\mathbf{Q}_t, \mathbf{P}_{t+dt}; t) \cdot \frac{\partial^2 S}{\partial \mathbf{q} \partial \mathbf{P}}(\mathbf{q}, \mathbf{P}_{t+dt}; t) dt \\
&= \frac{\partial S}{\partial \mathbf{q}}(\mathbf{q}, \mathbf{P}_{t+dt}; t) + \frac{\partial G}{\partial \mathbf{Q}}(\mathbf{Q}(\mathbf{q}, \mathbf{P}_t; t), \mathbf{P}_{t+dt}; t) \cdot \frac{\partial \mathbf{Q}}{\partial \mathbf{q}}(\mathbf{q}, \mathbf{P}_{t+dt}; t) dt \\
&= \frac{\partial S}{\partial \mathbf{q}}(\mathbf{q}, \mathbf{P}_{t+dt}; t) + \frac{\partial G}{\partial \mathbf{Q}}(\mathbf{Q}(\mathbf{q}, \mathbf{P}_{t+dt}; t), \mathbf{P}_{t+dt}; t) \cdot \frac{\partial \mathbf{Q}}{\partial \mathbf{q}}(\mathbf{q}, \mathbf{P}_{t+dt}; t) dt \\
&= \frac{\partial S}{\partial \mathbf{q}}(\mathbf{q}, \mathbf{P}_{t+dt}; t) + \frac{\partial G}{\partial \mathbf{q}}(\mathbf{Q}(\mathbf{q}, \mathbf{P}_{t+dt}; t), \mathbf{P}_{t+dt}; t) dt \qquad (1.16)
\end{aligned}
$$

The transformation between the second and third lines in the above derivation was obtained by switching from column vectors to row vectors.

We also have,

$$
\frac{\partial S}{\partial \mathbf{q}}(\mathbf{q}, \mathbf{P}_{t+dt}; t + dt) = \frac{\partial S}{\partial \mathbf{q}}(\mathbf{q}, \mathbf{P}_{t+dt}; t) + \frac{\partial^2 S}{\partial t \partial \mathbf{q}}(\mathbf{q}, \mathbf{P}_{t+dt}; t) dt \qquad (1.17)
$$

and so,

$$
\frac{\partial^2 S}{\partial t \partial \mathbf{q}} = \frac{\partial G}{\partial \mathbf{q}}(\mathbf{Q}(\mathbf{q}, \mathbf{P}_{t+dt}; t), \mathbf{P}_{t+dt}; t) \qquad (1.18)
$$

We also have,

$$
\begin{aligned}
\mathbf{Q}_t &= \frac{\partial S}{\partial \mathbf{P}}(\mathbf{q}, \mathbf{P}_t; t) \\
&= \frac{\partial S}{\partial \mathbf{P}}(\mathbf{q}, \mathbf{P}_{t+dt} + dt \frac{\partial G}{\partial \mathbf{Q}}(\mathbf{Q}_t, \mathbf{P}_{t+dt}; t); t) \\
&= \frac{\partial S}{\partial \mathbf{P}}(\mathbf{q}, \mathbf{P}_{t+dt}; t) + \frac{\partial^2 S}{\partial \mathbf{P}^2}(\mathbf{q}, \mathbf{P}_{t+dt}; t) \cdot \frac{\partial G}{\partial \mathbf{Q}}(\mathbf{Q}_t, \mathbf{P}_{t+dt}; t) dt \qquad (1.19)
\end{aligned}
$$

and

$$
\mathbf{Q}_{t+dt} = \frac{\partial S}{\partial \mathbf{P}}(\mathbf{q}, \mathbf{P}_{t+dt}; t + dt)
$$

$$= \frac{\partial S}{\partial \mathbf{P}}(\mathbf{q}, \mathbf{P}_{t+dt}; t) + \frac{\partial^2 S}{\partial t \partial \mathbf{P}}(\mathbf{q}, \mathbf{P}_{t+dt}; t)dt \tag{1.20}$$

and

$$\begin{aligned}
\mathbf{Q}_{t+dt} &= \mathbf{Q}_t + \frac{\partial G}{\partial \mathbf{P}}(\mathbf{Q}_t, \mathbf{P}_{t+dt}; t)dt \\
&= \frac{\partial S}{\partial \mathbf{P}}(\mathbf{q}, \mathbf{P}_{t+dt}; t) + \frac{\partial^2 S}{\partial \mathbf{P}^2}(\mathbf{q}, \mathbf{P}_{t+dt}; t) \cdot \frac{\partial G}{\partial \mathbf{Q}}(\mathbf{Q}_t, \mathbf{P}_{t+dt}; t)dt + \\
&\quad \frac{\partial G}{\partial \mathbf{P}}(\mathbf{Q}_t, \mathbf{P}_{t+dt}; t)dt
\end{aligned} \tag{1.21}$$

and so,

$$\begin{aligned}
\frac{\partial^2 S}{\partial t \partial \mathbf{P}}(\mathbf{q}, \mathbf{P}_{t+dt}; t) &= \frac{\partial^2 S}{\partial \mathbf{P}^2}(\mathbf{q}, \mathbf{P}_{t+dt}; t) \cdot \frac{\partial G}{\partial \mathbf{Q}}(\mathbf{Q}_t, \mathbf{P}_{t+dt}; t) + \\
&\quad \frac{\partial G}{\partial \mathbf{P}}(\mathbf{Q}_t, \mathbf{P}_{t+dt}; t) \\
&= \frac{\partial G}{\partial \mathbf{Q}}(\mathbf{Q}(\mathbf{q}, \mathbf{P}_t; t), \mathbf{P}_{t+dt}; t) \cdot \frac{\partial \mathbf{Q}}{\partial \mathbf{P}}(\mathbf{q}, \mathbf{P}_{t+dt}; t) + \\
&\quad \frac{\partial G}{\partial \mathbf{P}}(\mathbf{Q}(\mathbf{q}, \mathbf{P}_t; t), \mathbf{P}_{t+dt}; t) \\
&= \frac{\partial G}{\partial \mathbf{Q}}(\mathbf{Q}(\mathbf{q}, \mathbf{P}_{t+dt}; t), \mathbf{P}_{t+dt}; t) \cdot \frac{\partial \mathbf{Q}}{\partial \mathbf{P}}(\mathbf{q}, \mathbf{P}_{t+dt}; t) + \\
&\quad \frac{\partial G}{\partial \mathbf{P}}(\mathbf{Q}(\mathbf{q}, \mathbf{P}_{t+dt}; t), \mathbf{P}_{t+dt}; t) \\
&= \frac{\partial G}{\partial \mathbf{P}}(\mathbf{Q}(\mathbf{q}, \mathbf{P}_{t+dt}; t), \mathbf{P}_{t+dt}; t) \Big|_{\mathbf{q}}
\end{aligned} \tag{1.22}$$

Once again, a switch from column to row vectors gives us the equality between the first and second lines of the above derivation. Therefore, we see that,

$$\frac{\partial^2 S}{\partial \mathbf{q} \partial t} = \frac{\partial G}{\partial \mathbf{q}}(\frac{\partial S}{\partial \mathbf{P}}(\mathbf{q}, \mathbf{P}; t), \mathbf{P}; t) \tag{1.23}$$

and

$$\frac{\partial^2 S}{\partial \mathbf{P} \partial t} = \frac{\partial G}{\partial \mathbf{P}}(\frac{\partial S}{\partial \mathbf{P}}(\mathbf{q}, \mathbf{P}; t), \mathbf{P}; t) \Big|_{\mathbf{q}} \tag{1.24}$$

so we obtain,

$$\frac{\partial S}{\partial t}(\mathbf{q}, \mathbf{P}; t) = G(\frac{\partial S}{\partial \mathbf{P}}(\mathbf{q}, \mathbf{P}; t), \mathbf{P}; t) + C(t) \tag{1.25}$$

Since we only care about $(\mathbf{Q}_t, \mathbf{P}_t)$ and not about S itself, we can drop the $C(t)$ term, giving us, finally,

$$\frac{\partial S}{\partial t} = G(\frac{\partial S}{\partial \mathbf{P}}, \mathbf{P}; t) \tag{1.26}$$

1.3 Choosing G

We want an approach that minimizes the dependence of H on $\mathbf{Q}$. The condition that H be independent of $\mathbf{Q}$ is equivalent to the vanishing of the nonzero Fourier components $H_{\mathbf{k}}(\mathbf{P})$. We therefore seek to minimize the dependence of H on $\mathbf{Q}$ by choosing G in such a way that the $|H_{\mathbf{k}}(\mathbf{P}; t)|$ are continuously decreasing for all $\mathbf{k} \neq 0$.

At some time t, we can write $H(\mathbf{Q}, \mathbf{P}; t) = H^{(0)}(\mathbf{P}; t) + H^{(1)}(\mathbf{Q}, \mathbf{P}; t)$. The idea is that $H^{(0)}$ contains the piece of the Hamiltonian which is only

dependent on $\mathbf{P}$, and $H^{(1)}$ contains the remainder. Then,

$$\begin{aligned}\frac{\partial H}{\partial t} &= (\nabla_{\mathbf{P}} H^{(0)} + \nabla_{\mathbf{P}} H^{(1)}) \cdot \nabla_{\mathbf{Q}} G - \nabla_{\mathbf{Q}} H^{(1)} \cdot \nabla_{\mathbf{P}} G \\ &= \nabla_{\mathbf{P}} H^{(0)} \cdot \nabla_{\mathbf{Q}} G + \nabla_{\mathbf{P}} H^{(1)} \cdot \nabla_{\mathbf{Q}} G - \nabla_{\mathbf{Q}} H^{(1)} \cdot \nabla_{\mathbf{P}} G \\ &= \nabla_{\mathbf{P}} H^{(0)} \cdot \nabla_{\mathbf{Q}} G - \{H^{(1)}, G\} \end{aligned} \tag{1.27}$$

In the limit of a first-order perturbation on an integrable Hamiltonian, the relevant equation is,

$$\frac{\partial H}{\partial t} = \nabla_{\mathbf{P}} H^{(0)} \cdot \nabla_{\mathbf{Q}} G \tag{1.28}$$

In Fourier space, this becomes,

$$\frac{\partial H}{\partial t} = \frac{1}{V} \sum_{\mathbf{k}} \frac{\partial H_{\mathbf{k}}}{\partial t} e^{2\pi i \mathbf{k} \cdot \mathbf{Q}} = \nabla_{\mathbf{P}} H^{(0)} \cdot \frac{2\pi i}{V} \sum_{\mathbf{k}} \mathbf{k} G_{\mathbf{k}} e^{2\pi i \mathbf{k} \cdot \mathbf{Q}} \tag{1.29}$$

so

$$\frac{\partial H_{\mathbf{k}}}{\partial t} = 2\pi i (\mathbf{k} \cdot \nabla_{\mathbf{P}} H^{(0)}) G_{\mathbf{k}} \tag{1.30}$$

Then $\frac{\partial H_{\mathbf{k}} \bar{H}_{\mathbf{k}}}{\partial t} = H_{\mathbf{k}} \frac{\partial \bar{H}_{\mathbf{k}}}{\partial t} + \bar{H}_{\mathbf{k}} \frac{\partial H_{\mathbf{k}}}{\partial t} = 2\pi i (\mathbf{k} \cdot \nabla_{\mathbf{P}} H^{(0)})(\bar{H}_{\mathbf{k}} G_{\mathbf{k}} - H_{\mathbf{k}} \bar{G}_{\mathbf{k}})$. Therefore, in the first-order limit, the gradient-descent prescription for minimizing $|H_{\mathbf{k}}|^2 = H_{\mathbf{k}} \bar{H}_{\mathbf{k}}, \mathbf{k} \neq 0$ is to set $G_{\mathbf{k}} = 2\pi i (\mathbf{k} \cdot \nabla_{\mathbf{P}} H^{(0)}) H_{\mathbf{k}}$. Then $\bar{G}_{\mathbf{k}} = -2\pi i (\mathbf{k} \cdot \nabla_{\mathbf{P}} H^{(0)}) \bar{H}_{\mathbf{k}}$, so in the first-order limit we obtain that,

$$\frac{\partial H_{\mathbf{k}} \bar{H}_{\mathbf{k}}}{\partial t} = -8\pi^2 (\mathbf{k} \cdot \nabla_{\mathbf{P}} H^{(0)})^2 H_{\mathbf{k}} \bar{H}_{\mathbf{k}} \tag{1.31}$$

which is clearly negative. For stronger perturbations, this is no longer the gradient-descent prescription. However, for nearly integrable systems (the ones of interest to us in this chapter) the perturbation should still be sufficiently weak that the above choice for $G_{\mathbf{k}}$ will shrink the $H_{\mathbf{k}}\bar{H}_{\mathbf{k}}, \mathbf{k} \neq 0$. Therefore, we take,

$$G_{\mathbf{k}} = 2\pi i(\mathbf{k} \cdot \nabla_{\mathbf{P}} H^{(0)})H_{\mathbf{k}} \tag{1.32}$$

This gives,

$$\begin{aligned} G(\mathbf{Q},\mathbf{P}) &= \frac{1}{V}\sum_{\mathbf{k}} G_{\mathbf{k}}(\mathbf{P})e^{2\pi i\mathbf{k}\cdot\mathbf{Q}} = \frac{1}{V}2\pi i\nabla_{\mathbf{P}}H^{(0)} \cdot \sum_{\mathbf{k}} \mathbf{k}H_{\mathbf{k}}e^{2\pi i\mathbf{k}\cdot\mathbf{Q}} \\ &= \frac{2\pi i}{V}\nabla_{\mathbf{P}}H^{(0)} \cdot \frac{1}{2\pi i}\nabla_{\mathbf{Q}}\sum_{\mathbf{k}} H_{\mathbf{k}}e^{2\pi i\mathbf{k}\cdot\mathbf{Q}} \\ &= \nabla_{\mathbf{P}}H^{(0)} \cdot \nabla_{\mathbf{Q}}H \end{aligned} \tag{1.33}$$

so $G(\mathbf{Q},\mathbf{P}) = \nabla_{\mathbf{P}}H^{(0)} \cdot \nabla_{\mathbf{Q}}H = \nabla_{\mathbf{P}}H^{(0)} \cdot \nabla_{\mathbf{Q}}H^{(1)}$. Note that the Fourier expansion of G involves terms of the form $\mathbf{k} \cdot \nabla_{\mathbf{P}}H^{(0)}$. A $\mathbf{k}$ for which $\mathbf{k} \cdot \nabla_{\mathbf{P}}H^{(0)} = 0$ is a generalized resonance at $\mathbf{P}$. The integrability of $H^{(0)}$ is destroyed by the resonant terms in $H^{(1)}$.

Our evolution does not formally distinguish between resonances, near-resonances, and non-resonances. The evolution is done on the entire Hamiltonian without any terms neglected. However, the closer a term is to being resonant, the smaller the corresponding Fourier component of G, and so the

less that term is affected by the evolution.

In the first-order limit, $H^{(0)}(\mathbf{P};t)$ differs from $H^{(0)}(\mathbf{P};0)$ by a correction which is at most first-order in $H^{(1)}$. Therefore, if we use $H^{(0)}(\mathbf{P};0)$ instead of $H^{(0)}(\mathbf{P};t)$ in our prescription for choosing G in Eq. (1.33), we get a discrepancy of at most second-order in $H^{(1)}$, so that the two formulations are equivalent to first-order. Since our prescription for choosing G was derived from the first-order limit of the evolution of H, we see that it is equivalent to use $H^{(0)}(\mathbf{P};0)$ or $H^{(0)}(\mathbf{P};t)$ in Eq. (1.33). Finally, our $t=0$ Hamiltonian is usually given as $H(\mathbf{q},\mathbf{p}) = H_0(\mathbf{p}) + V(\mathbf{q},\mathbf{p})$, where H_0 is the zeroth-order, integrable Hamiltonian, and V is the perturbation. We can extract the $\mathbf{k}=0$ Fourier component of V, writing $V(\mathbf{q},\mathbf{p}) = V_0(\mathbf{p}) + \tilde{V}(\mathbf{q},\mathbf{p})$. Then $H(\mathbf{Q},\mathbf{P};0) = H_0(\mathbf{P}) + V_0(\mathbf{P}) + \tilde{V}(\mathbf{Q},\mathbf{P})$, so that $H^{(0)}(\mathbf{P};0) = H_0(\mathbf{P}) + V_0(\mathbf{P})$, and $H^{(1)}(\mathbf{Q},\mathbf{P};0) = \tilde{V}(\mathbf{Q},\mathbf{P})$. Therefore, note that in the first-order limit it is equivalent to use $H^{(0)}(\mathbf{P};0)$ or $H_0(\mathbf{P})$ in the prescription for choosing G. Once again, this means that it is equivalent to use $H^{(0)}(\mathbf{P};0)$ or $H_0(\mathbf{P})$. In what follows $H^{(0)}(\mathbf{P};t)$, $H^{(0)}(\mathbf{P};0)$, and $H_0(\mathbf{P})$ will all be denoted by $H^{(0)}$, or $H^{(0)}(\mathbf{P})$. When required, we will specify to which $H^{(0)}$ we are referring. Very often, one of the three choices will result in a formulation of the PDEs which is considerably simpler to implement than the others.

We conclude this section by deriving the PDE governing the evolution of S, given our prescription for choosing G. We have,

$$\frac{\partial S}{\partial t}(\mathbf{q},\mathbf{P};t) = G(\mathbf{Q}(\mathbf{q},\mathbf{P};t),\mathbf{P};t) = \nabla_{\mathbf{P}} H^{(0)} \cdot \nabla_{\mathbf{Q}} H(\mathbf{Q}(\mathbf{q},\mathbf{P};t),\mathbf{P};t) \quad (1.34)$$

Now, we know that $H(\mathbf{Q},\mathbf{P};t) = H(\mathbf{q},\mathbf{p};0) = H(\mathbf{q},\frac{\partial S}{\partial \mathbf{q}}(\mathbf{q},\mathbf{P};t);0)$. We also have,

$$\frac{\partial}{\partial \mathbf{q}} = \frac{\partial}{\partial \mathbf{Q}} \cdot \frac{\partial \mathbf{Q}}{\partial \mathbf{q}} = \frac{\partial}{\partial \mathbf{Q}} \frac{\partial^2 S}{\partial \mathbf{q} \partial \mathbf{P}} \quad (1.35)$$

Switching from row to column vectors gives $\frac{\partial}{\partial \mathbf{q}} = \frac{\partial^2 S}{\partial \mathbf{P} \partial \mathbf{q}} \frac{\partial}{\partial \mathbf{Q}}$, and so,

$$\frac{\partial}{\partial \mathbf{Q}} = (\frac{\partial^2 S}{\partial \mathbf{P} \partial \mathbf{q}})^{-1} \frac{\partial}{\partial \mathbf{q}} \quad (1.36)$$

and so the dynamics of S is governed by,

$$\frac{\partial S}{\partial t} = \frac{\partial H^{(0)}}{\partial \mathbf{P}} \cdot (\frac{\partial^2 S}{\partial \mathbf{P} \partial \mathbf{q}})^{-1} \frac{\partial H(\mathbf{q},\frac{\partial S}{\partial \mathbf{q}};0)}{\partial \mathbf{q}} \Big|_{\mathbf{P}} \quad (1.37)$$

Now, $\frac{\partial H(\mathbf{q},\frac{\partial S}{\partial \mathbf{q}};0)}{\partial \mathbf{q}} \Big|_{\mathbf{P}} = \frac{\partial H}{\partial \mathbf{q}} \Big|_{\mathbf{p}} (\mathbf{q},\frac{\partial S}{\partial \mathbf{q}};0) + \frac{\partial H}{\partial \mathbf{p}} \Big|_{\mathbf{q}} (\mathbf{q},\frac{\partial S}{\partial \mathbf{q}};0) \cdot \frac{\partial^2 S}{\partial \mathbf{q}^2}$. Once again, switching from row to column vectors gives,

$$\frac{\partial H(\mathbf{q},\frac{\partial S}{\partial \mathbf{q}};0)}{\partial \mathbf{q}} \Big|_{\mathbf{P}} = \frac{\partial H}{\partial \mathbf{q}} \Big|_{\mathbf{p}} (\mathbf{q},\frac{\partial S}{\partial \mathbf{q}};0) + \frac{\partial^2 S}{\partial \mathbf{q}^2} \frac{\partial H}{\partial \mathbf{p}} \Big|_{\mathbf{q}} (\mathbf{q},\frac{\partial S}{\partial \mathbf{q}};0) \quad (1.38)$$

Note that since $H(\mathbf{q},\mathbf{p};0)$ is simply our initial Hamiltonian, this PDE for S involves S only. We do not need the evolution of H in order to get the evolution of S.

The numerical evolution of S is described in Appendix A. Since the case for arbitrary canonical pairs is handled similarly, we do not give numerical details for the H evolution in this chapter.

1.4 The First-Order Limit

From our choice of G in the previous section, it follows that in the limit of a first-order perturbation on an integrable Hamiltonian,

$$\frac{\partial H_{\mathbf{k}}}{\partial t} = -4\pi^2(\mathbf{k}\cdot\nabla_{\mathbf{P}}H^{(0)})^2 H_{\mathbf{k}} \tag{1.39}$$

Our first-order solution yields $H_{\mathbf{k}}(\mathbf{P};t) = H_{\mathbf{k}}(\mathbf{P};0)\exp[-4\pi^2(\mathbf{k}\cdot\nabla_{\mathbf{P}}H^{(0)})^2 t]$. Note that the more non-resonant a term, the faster the exponential decay. In particular, resonances are not affected at all. It may also be noted that the first-order evolution equation amounts to running the Hamiltonian through a heat equation.

We now turn to the evolution of S in the first-order limit. To this end, write $S(\mathbf{q},\mathbf{P};t) = \mathbf{q}\cdot\mathbf{P} + \tilde{G}(\mathbf{q},\mathbf{P};t)$. In what follows we shall work to first-order in $\tilde{G}$ and $H^{(1)}$. Then,

$$\frac{\partial H}{\partial \mathbf{q}}\Big|_{\mathbf{p}}(\mathbf{q},\frac{\partial S}{\partial \mathbf{q}};0) = \frac{\partial H}{\partial \mathbf{q}}(\mathbf{q},\mathbf{P};0) + \frac{\partial^2 H}{\partial \mathbf{P}\partial \mathbf{q}}(\mathbf{q},\mathbf{P};0)\frac{\partial \tilde{G}}{\partial \mathbf{q}} \tag{1.40}$$

and

$$\frac{\partial^2 S}{\partial \mathbf{q}^2}\frac{\partial H}{\partial \mathbf{p}}\Big|_{\mathbf{q}}(\mathbf{q},\frac{\partial S}{\partial \mathbf{q}};0)=\frac{\partial^2 \tilde{G}}{\partial \mathbf{q}^2}\frac{\partial H}{\partial \mathbf{p}}\Big|_{\mathbf{q}}(\mathbf{q},\mathbf{P}+\frac{\partial \tilde{G}}{\partial \mathbf{q}};0)=\frac{\partial^2 \tilde{G}}{\partial \mathbf{q}^2}\frac{\partial H}{\partial \mathbf{P}}(\mathbf{q},\mathbf{P};0) \quad (1.41)$$

Now, $H(\mathbf{q},\mathbf{p};0)=H^{(0)}(\mathbf{p};0)+H^{(1)}(\mathbf{q},\mathbf{p};0)$. Then $\frac{\partial H}{\partial \mathbf{q}}(\mathbf{q},\mathbf{P};0)=\frac{\partial H^{(1)}}{\partial \mathbf{q}}(\mathbf{q},\mathbf{P};0)$. To first-order, $\frac{\partial^2 H}{\partial \mathbf{P}\partial \mathbf{q}}(\mathbf{q},\mathbf{P};0)\frac{\partial \tilde{G}}{\partial \mathbf{q}}=\frac{\partial^2 H^{(1)}}{\partial \mathbf{P}\partial \mathbf{q}}(\mathbf{q},\mathbf{P};0)\frac{\partial \tilde{G}}{\partial \mathbf{q}}=0$. Finally, to first-order, $\frac{\partial^2 \tilde{G}}{\partial \mathbf{q}^2}\frac{\partial H}{\partial \mathbf{P}}\Big|_{\mathbf{q}}(\mathbf{q},\mathbf{P};0)=\frac{\partial^2 \tilde{G}}{\partial \mathbf{q}^2}\frac{\partial H^{(0)}}{\partial \mathbf{P}}(\mathbf{P};0)$. Since each of these terms are either first-order in $H^{(1)}$ or $\tilde{G}$, in the first-order limit we take $(\frac{\partial^2 S}{\partial \mathbf{P}\partial \mathbf{q}})^{-1}=\mathbf{1}$.

Putting everything together gives us that our first-order equation is,

$$\frac{\partial \tilde{G}}{\partial t}=\frac{\partial H^{(0)}}{\partial \mathbf{P}}\cdot(\frac{\partial H^{(1)}}{\partial \mathbf{q}}+\frac{\partial^2 \tilde{G}}{\partial \mathbf{q}^2}\frac{\partial H^{(0)}}{\partial \mathbf{P}}) \quad (1.42)$$

In Fourier space, this becomes,

$$\frac{\partial \tilde{G}_{\mathbf{k}}}{\partial t}=2\pi i(\mathbf{k}\cdot\nabla_{\mathbf{P}}H^{(0)})H^{(1)}_{\mathbf{k}}-4\pi^2(\mathbf{k}\cdot\nabla_{\mathbf{P}}H^{(0)})^2\tilde{G}_{\mathbf{k}} \quad (1.43)$$

Since $\tilde{G}_{\mathbf{k}}(\mathbf{P};0)=0\ \forall\ \mathbf{k}$, we obtain,

$$\tilde{G}_{\mathbf{k}}(\mathbf{P};t)=\frac{iH^{(1)}_{\mathbf{k}}}{2\pi(\mathbf{k}\cdot\nabla_{\mathbf{P}}H^{(0)})}(1-e^{-4\pi^2(\mathbf{k}\cdot\nabla_{\mathbf{P}}H^{(0)})^2t}) \quad (1.44)$$

Note that $\tilde{G}_{\mathbf{k}}(\mathbf{P};t)=0$ for all resonant terms. This can be seen by looking at the original ODE from which the solution is derived, or equivalently by noting that $\lim_{\mathbf{k}\cdot\nabla_{\mathbf{P}}H^{(0)}\to 0}\ (1-\exp[-4\pi^2(\mathbf{k}\cdot\nabla_{\mathbf{P}}H^{(0)})^2t])/(\mathbf{k}\cdot\nabla_{\mathbf{P}}H^{(0)})=0$. We can write,

$$\tilde{G}(\mathbf{q},\mathbf{P};t)=\frac{1}{V}\frac{i}{2\pi}\sum_{\mathbf{k}\neq 0}\frac{H^{(1)}_{\mathbf{k}}}{\mathbf{k}\cdot\nabla_{\mathbf{P}}H^{(0)}}(1-e^{-4\pi^2(\mathbf{k}\cdot\nabla_{\mathbf{P}}H^{(0)})^2t})e^{2\pi i\mathbf{k}\cdot\mathbf{q}} \quad (1.45)$$

This series is convergent, because the exponential term prevents resonances and near resonances in the denominator from causing the series to diverge. We can let $t \to \infty$ to get the first-order perturbation theory result,

$$\tilde{G}(\mathbf{q}, \mathbf{P}; \infty) = \frac{1}{V} \frac{i}{2\pi} \sum_{\mathbf{k} \neq \mathbf{0}} \frac{H^{(1)}_{\mathbf{k}}}{\mathbf{k} \cdot \nabla_{\mathbf{P}} H^{(0)}} e^{2\pi i \mathbf{k} \cdot \mathbf{q}} \tag{1.46}$$

where the sum is over all non-resonant $\mathbf{k}$. Note, however, that the convergence of the various Fourier components to their $t \to \infty$ limits is not uniform, because the time constant for the exponential term is proportional to $1/(\mathbf{k} \cdot \nabla_{\mathbf{P}} H^{(0)})^2$. This goes to infinity as $\mathbf{k}$ approaches a resonance. The above equation must be solved for finite t, and then take the $t \to \infty$ limit. This prevents any ambiguities in $\tilde{G}$, something which will be illustrated in the next section.

We should point out that we have not derived a first-order classical perturbation theory that is necessarily convergent. The standard first-order formula is obtained by taking the $t \to \infty$ limit of our expression, and as can be clearly seen, the presence of near-resonances can result in a divergent series. However, the advantage of our formula is that for all finite t, the near-resonances are attenuated by the exponential term in such a way that the series does converge. Thus, this method does not require any a priori

removal of terms which are assigned as "resonant". Rather, all terms may be included in the first-order expression, and t may be chosen to be as large as possible without any Fourier term exceeding some cutoff criterion. In this way, the non-resonant Fourier terms will essentially have their standard first-order values, while the more nearly resonant terms will still have a non-negligible exponential term present which keeps the overall series convergent. The corresponding non-resonant Fourier terms in the Hamiltonian will then have been essentially killed off, while the more nearly resonant terms will have been reduced somewhat, but not completely.

1.5 Analytical Examples

1.5.1 1-D Example

Consider the case of free propagation perturbed by a weak, localized potential. Our Hamiltonian is,

$$H(q,p) = \frac{p^2}{2m} + V(q) \tag{1.47}$$

where $V(q)$ is finite in $\mathbf{R}$ and decays to 0 as $q \to \pm\infty$. For above-barrier energies we can construct an action function defined everywhere in coordinate

space, given by,

$$S(q,P) = P\int^{q}(1-\frac{2mV(q')}{P^2})^{\frac{1}{2}}dq' \tag{1.48}$$

where $P \equiv p(\pm\infty)$. Along a classical trajectory, we have $\frac{p^2}{2m} + V(q) = H(q,p) = \frac{p_\infty^2}{2m} = \frac{P^2}{2m}$, so the representation of H in the corresponding (Q,P) system is simply $H(q,p) = H^{(0)}(P) = \frac{P^2}{2m}$.

Because $S(q,P)$ is only determined up to some (possibly P-dependent) constant term, all we can uniquely specify is $p = \frac{\partial S}{\partial q} = P(1-\frac{2mV(q)}{P^2})^{\frac{1}{2}}$. In the first-order limit, we know from the previous section that our PDE method converges to a steady-state. Our method should still come close to a steady-state beyond the first-order, yet still weakly perturbed, regime. For the strongly perturbed case, we don't know what our method will do. Nevertheless, we can show that for all above-barrier energies, our method has a unique steady-state solution, and is given by the formula for $p(q,P)$ given above. To prove this, we note that in one dimension the evolution equation for S becomes,

$$\frac{\partial S}{\partial t} = \frac{P}{m}\frac{1}{\frac{\partial^2 S}{\partial P \partial q}}\frac{\partial H}{\partial q}\Big|_P \tag{1.49}$$

Setting $\frac{\partial S}{\partial t} = 0$, and remembering that for energies above the barrier we have

$P \neq 0$, we get the steady-state equation,

$$\frac{\partial H(q, \frac{\partial S}{\partial q})}{\partial q} \Big|_P = 0 \tag{1.50}$$

Note that this assumes that $\frac{\partial^2 S}{\partial P \partial q} \neq 0, \infty$, something that we will only be able to check once we solve our equation. The steady-state equation can be integrated at constant P to give $H(q, \frac{\partial S}{\partial q}) = C(P)$. Letting $q \to \pm\infty$ gives us that H becomes $\frac{p_\infty^2}{2m} = \frac{P^2}{2m}$, so $C(P) = \frac{P^2}{2m}$. Therefore, $\frac{1}{2m}(\frac{\partial S}{\partial q})^2 + V(q) = \frac{P^2}{2m} \Rightarrow \frac{\partial S}{\partial q} = P(1 - \frac{2mV(q)}{P^2})^{\frac{1}{2}}$.

Note that $\frac{\partial^2 S}{\partial P \partial q} \neq 0, \infty$ for all energies above the barrier, so our PDE approach does yield the appropriate steady-state solution. Below the barrier, we cannot construct a real action function defined for all q, since the momentum p becomes imaginary in the classically forbidden region. At a turning point, $\frac{\partial^2 S}{\partial P \partial q} = \infty$, so in any event our method for finding the steady-state breaks down below the barrier. Thus, both approaches to finding a real action function S presented in this section have an equal range of validity, namely, for all energies above the barrier. Semiclassically, this means that our PDE approach recovers WKB theory for above-barrier energies. Maitra and Heller [11] developed a method to compute above-barrier reflection coefficients using the WKB wavefunctions as a distorted-wave basis. The above

derivation shows that this approach is contained as a subcase within our PDE-based approach.

1.5.2 2-D Example

Consider the Hamiltonian,

$$H(x, y, p_x, p_y) = \frac{p_x^2 + p_y^2}{2m} + \lambda e^{-\alpha(x^2+y^2)} \tag{1.51}$$

We wish to construct an action function $S(x, y, P_x, P_y)$ in the first-order limit. By the symmetry of this problem, we need only consider $P_y = 0$. So, let's write $S(x, y, P_x, P_y) = xP_x + yP_y + G(x, y, P_x, P_y)$, where G is our first-order correction. We substitute into the time-independent Hamilton-Jacobi equation (HJE) to get,

$$\begin{aligned} E &= H(x, y, P_x + \frac{\partial G}{\partial x}, P_y + \frac{\partial G}{\partial y}) \\ &= \frac{1}{2m}(P_x^2 + P_y^2) + \frac{P_x}{m}\frac{\partial G}{\partial x} + \frac{P_y}{m}\frac{\partial G}{\partial y} + \lambda e^{-\alpha(x^2+y^2)} \end{aligned} \tag{1.52}$$

Set $P_y = 0$, $E = \frac{P_x^2}{2m}$ to get,

$$\frac{\partial G}{\partial x} = -\frac{\lambda m}{P_x} e^{-\alpha(x^2+y^2)} \tag{1.53}$$

which can be integrated to give $G(x, y, P_x, 0) = -\frac{\lambda m}{P_x} e^{-\alpha y^2} \int_{-\infty}^{x} e^{-\alpha x'^2} dx' + C(y, P_x)$. Now, C is determined by the boundary conditions which we impose

on this system. The first set of boundary conditions we will consider is the requirement that $p_y = 0$ at $x = -\infty$. We have,

$$\frac{\partial G}{\partial y} = \frac{2\lambda m\alpha}{P_x} y e^{-\alpha y^2} \int_{-\infty}^{x} e^{-\alpha x'^2} dx' + \frac{\partial C}{\partial y} \tag{1.54}$$

Then at $x = -\infty$ we get $p_y = \frac{\partial C}{\partial y} = 0$, so $C = C(P_x)$. Since the HJE only depends on the momentum field generated by S and not on S itself, a P_x-dependent constant term is unimportant, so we can set it to 0. Therefore, one first-order solution is,

$$\begin{aligned} G_1(x, y, P_x, 0) &= -\frac{\lambda m}{P_x} e^{-\alpha y^2} \int_{-\infty}^{x} e^{-\alpha x'^2} dx' \\ &= -\frac{\lambda m}{P_x \sqrt{\alpha}} e^{-\alpha y^2} \int_{-\infty}^{\sqrt{\alpha} x} e^{-u^2} du \end{aligned} \tag{1.55}$$

An alternative solution is obtained from the boundary condition that $p_y \Big|_{x=-\infty} = -p_y \Big|_{x=\infty}$. Plugging into our expression for $\frac{\partial G}{\partial y}$ gives $\frac{\partial C}{\partial y} = -\frac{2\lambda m\alpha}{P_x} \sqrt{\frac{\pi}{\alpha}} y e^{-\alpha y^2} - \frac{\partial C}{\partial y}$, which can be solved for $\frac{\partial C}{\partial y}$ and integrated to yield,

$$C(y, P_x) = \frac{\lambda m}{2P_x} \sqrt{\frac{\pi}{\alpha}} e^{-\alpha y^2} + \tilde{C}(P_x) \tag{1.56}$$

As before, we drop the P_x-dependent constant term. The result is another first-order solution,

$$G_2(x, y, P_x, 0) = -\frac{\lambda m}{P_x \sqrt{\alpha}} e^{-\alpha y^2} \left(\int_{-\infty}^{\sqrt{\alpha} x} e^{-u^2} du - \frac{\sqrt{\pi}}{2} \right)$$

$$= -\frac{\lambda m}{P_x\sqrt{\alpha}}e^{-\alpha y^2}(\int_{-\infty}^{\sqrt{\alpha}x} e^{-u^2}du - \int_{-\infty}^{0} e^{-u^2}du)$$
$$= -\frac{\lambda m}{P_x\sqrt{\alpha}}e^{-\alpha y^2}\int_{0}^{\sqrt{\alpha}x} e^{-u^2}du \quad (1.57)$$

Figures 1.1a,b plot the momentum fields generated by G_1 and G_2. Note that G_1 produces the more physically intuitive manifold of trajectories, since they first head straight toward the Gaussian bump, and are only deflected as they approach it. The G_2 trajectories, in contrast, are symmetrical to the left and right of the bump. This is accomplished by initially angling the trajectories inward toward the bump. The trajectories curve in and then curve away as they reach the bump.

We now turn to a first-order treatment using the approach derived from our PDE method. We begin by using the position formulation of our PDE in the first-order limit, given by Eq. (1.42). We know that the evolution of G goes to a steady-state, so setting $\frac{\partial G}{\partial t} = 0$, and plugging in the terms for our specific potential, yields,

$$-\frac{2\alpha\lambda}{m}e^{-\alpha(x^2+y^2)}(P_x x+P_y y)+\frac{1}{m^2}(\frac{\partial^2 G}{\partial x^2}P_x^2+2\frac{\partial^2 G}{\partial x\partial y}P_x P_y+\frac{\partial^2 G}{\partial y^2}P_y^2) = 0 \quad (1.58)$$

At $P_y = 0$ we get $\frac{\partial^2 G}{\partial x^2} = \frac{2\alpha\lambda m}{P_x}xe^{-\alpha(x^2+y^2)}$. Integrating gives,

$$\frac{\partial G}{\partial x} = -\frac{\lambda m}{P_x}e^{-\alpha(x^2+y^2)} + C(y, P_x) \quad (1.59)$$

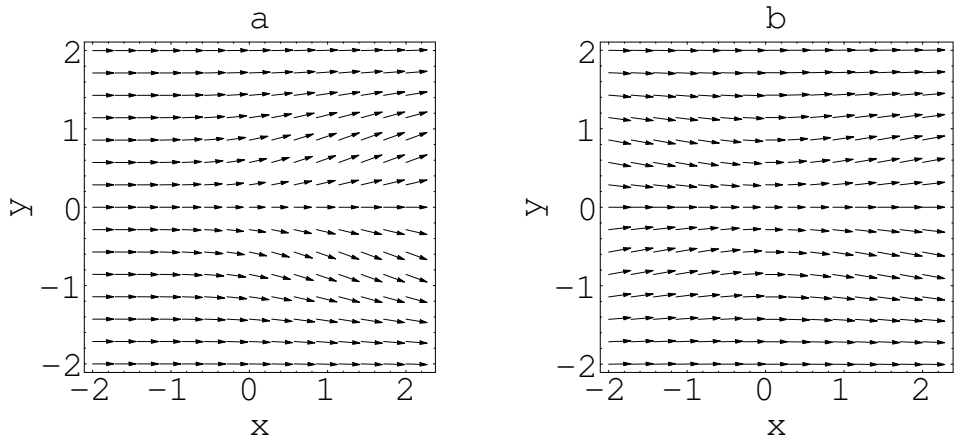

Figure 1.1: The first-order momentum fields generated by the G_1 and G_2 manifold of trajectories, where $m = 1.0$, $\alpha = 1.0$, $\lambda = 1.0$, and $P_x = 2$. (a) The G_1 manifold. (b) The G_2 manifold.

If we require $p_x \Big|_{x=-\infty} = P_x$, then $\frac{\partial G}{\partial x} \Big|_{x=-\infty} = 0 \Rightarrow C(y, P_x) = 0$. Our resulting differential equation for G is therefore identical to the one obtained via the HJE in the first-order limit.

We now use the Fourier formulation of our first-order, PDE-based approach, by applying Eq. (1.45). The Fourier components of $e^{-\alpha(x^2+y^2)}$ are given by $\lambda \frac{\pi}{\alpha} e^{-\frac{\pi^2}{\alpha}(k_x^2+k_y^2)}$. Therefore, we obtain,

$$G(x,y,P_x,P_y;t) = \frac{i\lambda}{2\pi}\frac{\pi}{\alpha}\int_{-\infty}^{\infty}\int_{-\infty}^{\infty}dk_xdk_y\frac{\exp[-\frac{\pi^2}{\alpha}(k_x^2+k_y^2)]}{k_x\frac{P_x}{m}+k_y\frac{P_y}{m}}\times$$
$$(1-e^{-4\pi^2\frac{(k_xP_x+k_yP_y)^2}{m^2}t})e^{2\pi i(k_xx+k_yy)} \qquad (1.60)$$

We now set $P_y = 0$, giving

$$G(x,y,P_x,0;t) = \frac{i\lambda m}{2\alpha P_x}\int_{-\infty}^{\infty}\int_{-\infty}^{\infty}dk_xdk_y\frac{\exp[-\frac{\pi^2}{\alpha}k_x^2]\exp[-\frac{\pi^2}{\alpha}k_y^2]}{k_x}\times$$
$$(1-e^{-4\pi^2k_x^2P_x^2t/m^2})e^{2\pi ik_xx}e^{2\pi ik_yy}$$
$$= \frac{i\lambda m}{2\alpha P_x}\sqrt{\frac{\alpha}{\pi}}e^{-\alpha y^2}\int_{-\infty}^{\infty}dk_x\frac{\exp[-\frac{\pi^2}{\alpha}k_x^2]}{k_x}(1-e^{-4\pi^2k_x^2P_x^2t/m^2})e^{2\pi ik_xx}$$
$$= \frac{i\lambda m}{2P_x\sqrt{\alpha\pi}}e^{-\alpha y^2}\int_{-\infty}^{\infty}dk_xe^{-\frac{\pi^2}{\alpha}k_x^2}(1-e^{-4\pi^2k_x^2P_x^2t/m^2})\times$$
$$(2\pi i\int_0^x e^{2\pi ik_xx'}dx'+\frac{1}{k_x})$$
$$= -\frac{\lambda m}{P_x}\sqrt{\frac{\pi}{\alpha}}e^{-\alpha y^2}\int_0^x dx'\int_{-\infty}^{\infty}dk_xe^{-\frac{\pi^2}{\alpha}k_x^2}(1-e^{-4\pi^2k_x^2P_x^2t/m^2})e^{2\pi ik_xx'}+$$
$$\frac{i\lambda m}{2P_x\sqrt{\alpha\pi}}e^{-\alpha y^2}\int_{-\infty}^{\infty}\frac{dk_x}{k_x}e^{-\frac{\pi^2}{\alpha}k_x^2}(1-e^{-4\pi^2k_x^2P_x^2t/m^2}) \qquad (1.61)$$

The second integral vanishes, because the integrand is an odd function of k_x.

This gives us,

$$G(x,y,P_x,0;t) = -\frac{\lambda m}{P_x}\sqrt{\frac{\pi}{\alpha}}e^{-\alpha y^2}\int_0^x dx'\int_{-\infty}^{\infty}dk_xe^{-\frac{\pi^2}{\alpha}k_x^2}(1-e^{-4\pi^2k_x^2P_x^2t/m^2})e^{2\pi ik_xx'}$$
$$= -\frac{\lambda m}{P_x}\sqrt{\frac{\pi}{\alpha}}e^{-\alpha y^2}\int_0^x dx'\int_{-\infty}^{\infty}dk_x(\exp[-\frac{\pi^2}{\alpha}k_x^2]-$$
$$\exp[-\frac{\pi^2}{\frac{1}{\frac{1}{\alpha}+4P_x^2t/m^2}}k_x^2])e^{2\pi ik_xx'}$$

$$= -\frac{\lambda m}{P_x}\sqrt{\frac{\pi}{\alpha}}e^{-\alpha y^2}\int_0^x dx'(\sqrt{\frac{\alpha}{\pi}}\exp[-\alpha x'^2] - \frac{1}{\sqrt{\pi(\frac{1}{\alpha}+4P_x^2t/m^2)}}\exp[-\frac{x'^2}{\frac{1}{\alpha}+4P_x^2t/m^2}]) \quad (1.62)$$

We can break this integral into two pieces. First let's note the following change of variable: Setting $u = \sqrt{\alpha}\lambda$ gives, $\int_0^x d\lambda\sqrt{\frac{\alpha}{\pi}}e^{-\alpha\lambda^2} = \frac{1}{\sqrt{\pi}}\int_0^{\sqrt{\alpha}x} due^{-u^2}$. Therefore,

$$\begin{aligned} G(x,y,P_x,0;t) &= -\frac{\lambda m}{P_x\sqrt{\alpha}}e^{-\alpha y^2}(\int_0^{\sqrt{\alpha}x} e^{-u^2}du - \int_0^{\frac{x}{\sqrt{\frac{1}{\alpha}+4P_x^2t/m^2}}} e^{-u^2}du) \\ &= -\frac{\lambda m}{P_x\sqrt{\alpha}}e^{-\alpha y^2}\int_{\frac{\sqrt{\alpha}x}{\sqrt{1+4P_x^2\alpha t/m^2}}}^{\sqrt{\alpha}x} e^{-u^2}du \quad (1.63) \end{aligned}$$

Letting $t \to \infty$ gives us,

$$G(x,y,P_x,0) = -\frac{\lambda m}{P_x\sqrt{\alpha}}e^{-\alpha y^2}\int_0^{\sqrt{\alpha}x} e^{-u^2}du \quad (1.64)$$

Thus, the Fourier space approach yields the G_2 function obtained previously. Note that it was necessary to take the $t \to \infty$ limit only at the end, in order to avoid any ambiguities in evaluating the integrals.

1.6 A Numerical Example

We chose to test the S evolution numerically on the two-dimensional Pullen-Edmonds Hamiltonian [8], given by,

$$H(x, y, p_x, p_y) = \frac{p_x^2 + p_y^2}{2} + \frac{1}{2}(\omega_x^2 x^2 + \omega_y^2 y^2) + \epsilon x^2 y^2 \tag{1.65}$$

This was the two-dimensional system studied numerically in Ref. 2 in testing the GDA method. The results there were compared with those obtained in Ref. 3 using the CHM method. However, while in Ref. 2 the evolution was done on H in the context of obtaining a semiclassical quantum spectrum, in this case it is the PDE for S that is being tested.

We set $\omega_x = \omega_y = 1$. The $t = 0$ canonical representation is simply the harmonic oscillator action-angle basis, denoted by $(\theta_x, \theta_y, J_x, J_y)$. The arbitrary t canonical representation is denoted by $(\phi_x, \phi_y, I_x, I_y)$, so that $S = S(\theta_x, \theta_y, I_x, I_y; t)$, with $J_x = \frac{\partial S}{\partial \theta_x}$, and $J_y = \frac{\partial S}{\partial \theta_y}$. The transformation to the harmonic representation is obtained by setting $x = \sqrt{\frac{J_x}{\pi}} \cos 2\pi\theta_x$, $p_x = -\sqrt{\frac{J_x}{\pi}} \sin 2\pi\theta_x$, and similarly for y, p_y. The result is,

$$\begin{aligned} H(\theta_x, \theta_y, J_x, J_y) &= \frac{1}{2\pi}(J_x + J_y) + \frac{\epsilon J_x J_y}{4\pi^2}(1 + \cos 4\pi\theta_x + \cos 4\pi\theta_y + \\ &\quad \frac{1}{2}(\cos 4\pi(\theta_x + \theta_y) + \cos 4\pi(\theta_x - \theta_y))) \end{aligned} \tag{1.66}$$

The only nonvanishing Fourier components are $\pm(2,0), \pm(0,2), \pm(2,2)$, and $\pm(2,-2)$. Note in particular that $\pm(2,-2)$ is a resonance.

Of the three prescriptions for choosing G, the simplest one to use is $H^{(0)} = H_0 = \frac{1}{2\pi}(1,1)\cdot(I_x, I_y)$, so that $\nabla_{\mathbf{P}} H^{(0)}$ is taken to be $\frac{1}{2\pi}(1,1)$. In addition, for this Hamiltonian it is readily verified that,

$$\begin{aligned}\frac{\partial H}{\partial \mathbf{q}}\Big|_{\mathbf{P}}(\mathbf{q}, \frac{\partial S}{\partial \mathbf{q}}; 0) &= -\frac{\epsilon}{\pi}\frac{\partial S}{\partial \theta_x}\frac{\partial S}{\partial \theta_y}(\sin 4\pi\theta_x + \frac{1}{2}(\sin 4\pi(\theta_x+\theta_y) + \sin 4\pi(\theta_x-\theta_y)), \\ &\quad \sin 4\pi\theta_y + \frac{1}{2}(\sin 4\pi(\theta_x+\theta_y) - \sin 4\pi(\theta_x-\theta_y))) \qquad (1.67)\end{aligned}$$

and,

$$\begin{aligned}\frac{\partial H}{\partial \mathbf{p}}\Big|_{\mathbf{q}} &= \frac{1}{2\pi}(1,1) + \frac{\epsilon}{4\pi^2}(1 + \cos 4\pi\theta_x + \cos 4\pi\theta_y + \\ &\quad \frac{1}{2}(\cos 4\pi(\theta_x+\theta_y) + \cos 4\pi(\theta_x-\theta_y)))(\frac{\partial S}{\partial \theta_y}, \frac{\partial S}{\partial \theta_x}) \qquad (1.68)\end{aligned}$$

We substitute into Eq. (1.38) and then into Eq. (1.37) to get the PDE for S.

We set $\epsilon = 0.05$, and $I_x = I_y = 9\pi$. This corresponds to a torus with zeroth-order energy $E = 9$ at $t = 0$. The system is nearly integrable in this regime [3], yet a study of the semiclassically obtained energy spectrum [2, 3] shows clear differences with first-order perturbation theory. We therefore test our PDE beyond the first-order limit with this example.

We set $N = 20$, $DX = 0.1$, $DT = 0.034$, and $GDSZ = 9$, which allowed us to propagate the PDE out to a time of 0.306 (the meaning of these parameters is given in Appendix A). The rate of change of S on the grid reaches a minimum at this point (which was determined by tracking $\sqrt{\langle(\partial S/\partial t)^2\rangle}$ on the grid), so the evolution was stopped here. Because our PDE approach is only the gradient-descent prescription in the first-order limit, for finite perturbations there is no reason to expect the evolution to reach steady-state. We discuss this issue further in Appendix A.

Figures 1.2a-d show the results of the evolution at times $t = 0.0, 0.1, 0.2,$ and 0.3. It should be noted that we are not plotting S in these graphs. Rather, we plot $H(\theta_x, \theta_y, \frac{\partial S}{\partial \theta_x}, \frac{\partial S}{\partial \theta_y})$. There are two reasons for this: First, because we are working in the weakly perturbed, though still beyond first-order, regime, S remains fairly close to the identity transformation. The effect on $H(\theta_x, \theta_y, \frac{\partial S}{\partial \theta_x}, \frac{\partial S}{\partial \theta_y})$, however, is dramatic, and so it is much more convenient to represent the evolution of S in this indirect fashion. Second, even if the perturbation were sufficiently strong to significantly deform S, the only way to determine if the deformation of S is correct is to look at its effect on H.

Using the formula derived in Appendix B, it is readily shown that the

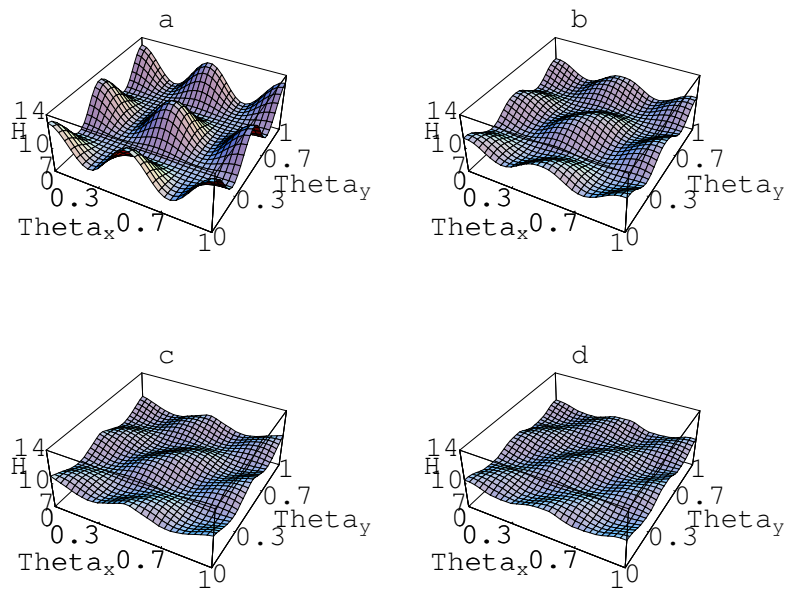

Figure 1.2: Plot of $H(\theta_x, \theta_y, \frac{\partial S}{\partial \theta_x}, \frac{\partial S}{\partial \theta_y})$ at various times for the Pullen-Edmonds Hamiltonian. (a) $t = 0.0$. (b) $t = 0.1$. (c) $t = 0.2$. (d) $t = 0.3$.

first-order solution to $H(\theta_x, \theta_y, \frac{\partial S}{\partial \theta_x}, \frac{\partial S}{\partial \theta_y})$ is,

$$H(\theta_x, \theta_y, \frac{\partial S}{\partial \theta_x}, \frac{\partial S}{\partial \theta_y}) = \frac{1}{2\pi}(I_x + I_y) + \frac{\epsilon I_x I_y}{4\pi^2}(1 + e^{-4t}(\cos 4\pi\theta_x + \cos 4\pi\theta_y) + \frac{1}{2}(\cos 4\pi(\theta_x - \theta_y) + e^{-16t}\cos 4\pi(\theta_x + \theta_y))) \quad (1.69)$$

While the perturbation is sufficiently strong that there are clear differences with first-order perturbation theory, the perturbation is still sufficiently weak

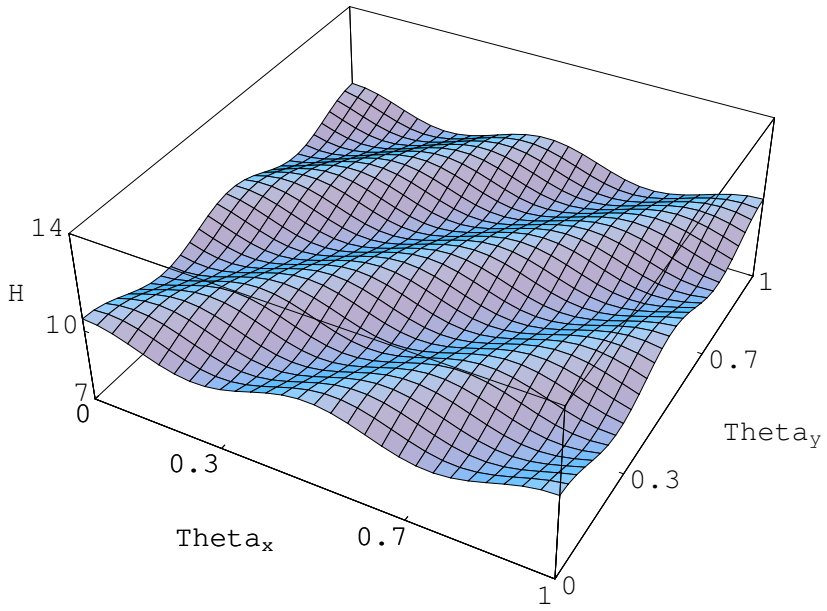

Figure 1.3: Plot of $H(\theta_x, \theta_y, \frac{\partial S}{\partial \theta_x}, \frac{\partial S}{\partial \theta_y})$ for the Pullen-Edmonds Hamiltonian for $t = \infty$ in the first-order limit.

that the first-order result provides a qualitative and semiquantitative picture of how the evolution should proceed.

Letting $t \to \infty$, we see that the long-time limit of the evolution gives,

$$H(\theta_x, \theta_y, \frac{\partial S}{\partial \theta_x}, \frac{\partial S}{\partial \theta_y}) \Big|_{t=\infty} = \frac{1}{2\pi}(I_x + I_y) + \frac{\epsilon I_x I_y}{4\pi^2}(1 + \frac{1}{2}\cos 4\pi(\theta_x - \theta_y)) \quad (1.70)$$

This is plotted for our specific set of parameters in Figure 1.3. Note that the numerical evolution does indeed deform S in such a way that the graphs in

Figures 1.2a-d evolve to look like the graph in Figure 1.3. Without the $(2,-2)$ resonance, H is integrable at this energy [3], so it is possible to transform to a basis in which H only depends on (I_x, I_y). Instead, the evolution eliminates as much of the nonresonant behavior as possible, but the resonant angle dependence arising from the $(2,-2)$ term remains. In Figures 1.4a-d we present the results of the evolution on the Hamiltonian obtained by removing the $(2,-2)$ resonance from the Pullen-Edmonds term. We changed DT to 0.033 and $GDSZ$ to 11. All other parameters are otherwise unchanged. In this case, the evolution should flatten H, and as Figures 1.4a-d confirm, this is exactly what happens.

1.7 Construction of Semiclassical Wavefunctions

We applied this PDE-based approach to construct optimized semiclassical wavefunctions for gaussian bump potentials. Thus, we considered a Hamiltonian of the form,

$$H(x, y, p_x, p_y) = \frac{p_x^2 + p_y^2}{2} + \lambda \exp[-(ax^2 + 2cxy + by^2)] \tag{1.71}$$

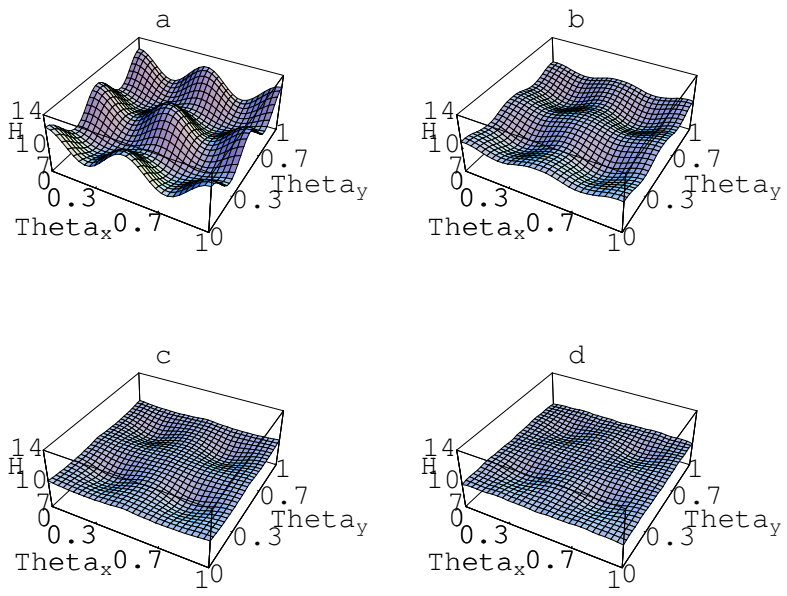

Figure 1.4: Plot of $H(\theta_x, \theta_y, \frac{\partial S}{\partial \theta_x}, \frac{\partial S}{\partial \theta_y})$ at various times for the Pullen-Edmonds Hamiltonian with the $(2, -2)$ resonance removed. (a) $t = 0.0$. (b) $t = 0.1$. (c) $t = 0.2$. (d) $t = 0.3$.

We considered two different potentials. For Potential I, we took $\lambda_1 = 1, a = b = 1, c = 0$. For Potential II, we took $\lambda_2 = 1, a = b = 3, c = 2$. This corresponds to the potential $\exp[-(x^2 + 5y^2)]$, with the xy-axis rotated clockwise by 45°.

The S evolution was solved for $P_x = 1.5, P_y = 0.0$, corresponding to

a particle momentum of $(1.5, 0.0)$ far away from the potential. Thus, the particle energy is above the bump height for both potentials. We worked on the spatial grid $[-4, 4] \times [-4, 4]$ with a step size of 0.2. We used a momentum step size of 0.05. Starting at time $t = 0$, we propagated out to $t = 0.2$ for Potential I and $t = 0.15$ for Potential II using a time step of 0.01. In both cases, the rate of change of S on the grid was at least 50% smaller at the end of the evolution than at the beginning.

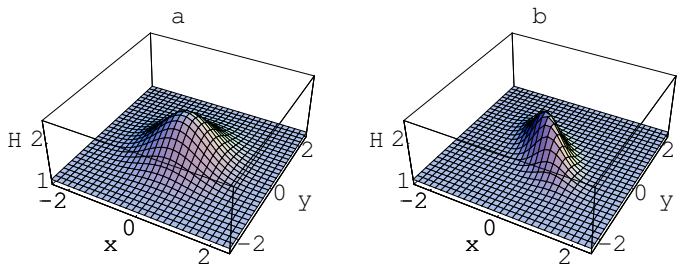

Figure 1.5: Plot of $H(\theta_x, \theta_y, \frac{\partial S}{\partial \theta_x}, \frac{\partial S}{\partial \theta_y})$ at $t = 0.0$ for Potentials I and II. (a) Potential I. (b) Potential II.

Figures 1.5a,b plot $H(x, y, \frac{\partial S}{\partial x}, \frac{\partial S}{\partial y})$ for the two potentials at the start of their respective evolutions, while Figures 1.6a,b are probability density plots of the corresponding wavefunctions. White regions correspond to enhanced probability density, while dark regions correspond to depleted probability

density. In both cases, the maximum probability density change from the background value of 1 is from $20-30\%$. Note how the wavefunctions reveal some of the underlying classical dynamics. For the symmetric gaussian bump of Potential I, classical trajectories are deflected around the bump. Thus, there should be a depletion of probability in the center of the bump, and an enhancement in the region around the bump. As Figure 1.6a illustrates, this is exactly what happens. A similar situation occurs in Figure 1.6b. This time, however, the distribution is angled somewhat along the direction of the potential, which should be expected classically.

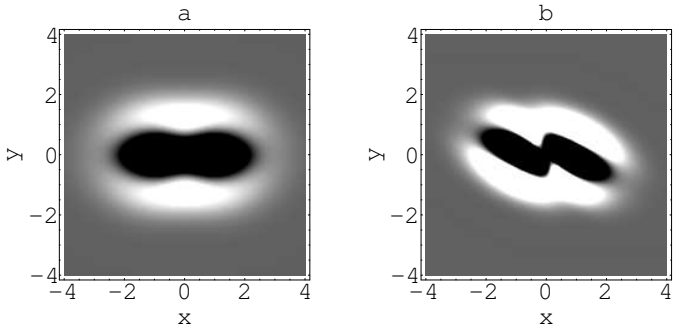

Figure 1.6: Probability density plots of the semiclassical wavefunctions generated from the evolution on Potentials I and II. (a) The wavefunction for Potential I. (b) The wavefunction for Potential II.

The one feature that may not be physically intuitive is the symmetry of the probability distribution. However, we may recall from subsection 1.5.2, in which we constructed first-order momentum fields for the symmetric gaussian bump, that the generating function S is not necessarily unique. Our method happens to select that S which gives rise to a symmetric momentum field.

1.8 Conclusions and Future Research

This chapter presented a PDE-based, phase-space deformation approach to optimize the canonical basis with which to globally represent a nearly integrable Hamiltonian. Because this method reduces to a gradient-descent approach for optimizing the canonical basis in the first-order limit, it was called the GDA method in Ref. 2, where it was initially applied to determine the eigenenergies of 2, 4, and 6 degree of freedom systems. The GDA method is compatible with any canonical representation of phase space, and allows the construction and visualization of the semiclassical wavefunctions corresponding to the optimized canonical basis for the given Hamiltonian.

As was mentioned in the Introduction, the motivation for this work is derived from semiclassical quantum mechanics. In light of the results for the

H evolution in Ref. 2 (and Chapter 2), this method may be useful in understanding vibrational dynamics in polyatomic molecules. It may also be useful as a way to construct distorted-wave basis sets for scattering calculations, and hence may find application in mesoscopic physics. It should be noted in this regard that this PDE-based approach contains other methods as subcases. For example, in Ref. 11, Maitra and Heller used one-dimensional WKB wavefunctions as a distorted-wave basis for computing above-barrier reflection coefficients. It was shown, in subsection 1.5.1, that our PDE method has a unique steady-state, which exactly coincides with the one-dimensional WKB wavefunctions, for all above-barrier energies. Thus, the Maitra-Heller method is contained within the GDA method. In their paper, Maitra and Heller raised the issue of generalizing their technique to higher dimensions, and to action-angle systems. Our PDE-based approach is exactly this generalization.

At this point, we have not yet applied the GDA method to actual systems. The main difficulty in dealing with vibrational calculations for polyatomics is that it is currently difficult to obtain accurate vibrational potential energy surfaces, even for few-atom polyatomics. However, it would be useful to apply the GDA method to actual systems at some point. In addition, while we write

in the Introduction that we believe the GDA approach is significantly faster than previous canonical basis optimization algorithms (at least for the H evolution), we also wrote that in fairness no speed comparisons have been made to date. Thus, another potentially useful study would be to compare the GDA method with the various other methods on the market.

To conclude, we should add that Heller has often made the comparison between the separatrix region generated by a local potential bump in one dimension to the resonance zone structure in a Poincare surface of section of a nearly integrable Hamiltonian [7, 11]. Indeed, Heller regards the above-barrier reflection problem as a prototype for the more complicated case of dynamical tunneling between invariant tori facilitated by resonance zones. Because both types of systems can be treated within the same PDE-based approach, they are, in fact, formally equivalent phenomena.

Chapter 2

Semiclassical Quantization Using Invariant Tori: A Gradient-Descent Approach

This chapter applies the GDA phase-space deformation method developed in the previous chapter to the problem of determining the energy spectra of bound Hamiltonians. For such systems, the GDA method finds an optimal semiclassical basis of invariant tori which minimizes the angular dependence of the Hamiltonian. This representation of the Hamiltonian is termed an

Intrinsic Resonance Representation (IRR), and it gives the smallest possible basis obtainable from classical mechanics. We demonstrate the GDA method by first reproducing results from a 2 degree-of-freedom system used to demonstrate the previous Carioli, Heller, and Moller (CHM) implementation of the IRR approach. We then go on to show that our method can be applied to higher dimensional Hamiltonians than previously studied by using it to EBK quantize a 6 degree-of-freedom system.

2.1 Introduction

The semiclassical quantization of D-dimensional non-separable Hamiltonians is an old and difficult problem. Before the discovery of the Schrodinger Equation, the standard procedure was essentially what is known today as the Einstein-Brillouin-Keller (EBK) quantization method. In this method, one looks for canonical momenta $I_1, \ldots, I_D$ which are invariants of the Hamiltonian, known as the action variables, and then sets these invariants equal to $2\pi\hbar(n_i + \frac{\alpha_i}{4})$, where the α_i are the Maslov indices. (A system for which such invariants can be found everywhere in phase space is said to be integrable.) The Hamiltonian H depends exclusively on the D actions $I_1, \ldots, I_D$, and

so the semiclassical energies of the Hamiltonian are characterized by good quantum numbers via $E(n_1, \ldots, n_D) = H(I_1, \ldots, I_D)$, with $I_i = 2\pi\hbar(n_i + \frac{\alpha_i}{4})$. Usually $\alpha_i = 2$, which is obtained from the WKB theory.

In one-dimension, this procedure is straightforward. There is only one action variable I, and it is given by,

$$I = \oint p dq \tag{2.1}$$

where the contour integral denotes integration over one period of the motion, and $p = \pm\sqrt{2m(E - V(q))}$ is the momentum of the particle. It is usually not possible to obtain $I = I(E)$ analytically, and in the case of multiple wells there is more than one I for a given E. Nevertheless, with today's powerful computers, the implementation of this method is relatively straightforward.

This simple scheme fails in higher dimensions. The problem is that for a general non-separable Hamiltonian, the classical motion may very well be chaotic. No other invariants other than the energy can be found, and so the energies cannot be characterized by good actions. On the other hand, if the Hamiltonian is separable, then the problem can be broken down into a series of one dimensional problems. Because for each degree of freedom the phase space motion traces out a closed curve topologically equivalent to

a circle, the overall motion of the whole system lies on what is called an invariant torus. The invariant tori fill out the entire phase space (or at least the region within any kind of dissociation energy of the system). The tori are each characterized by an action vector $I = (I_1, \ldots, I_D)$, and our system is quantized in the manner described above.

If an integrable system is perturbed, and the perturbation is sufficiently weak, then most of the phase space is still covered by invariant tori [26]. This is essentially the content of the KAM Theorem. Thus, it is still possible to find the semiclassical energies using the EBK approach. The complication that arises is the presence of resonances or near-resonances which lead to the formation resonance zones. Invariant tori still exist inside the resonance zones; however, they are described by a set of action-angle variables which cannot be analytically continued outside the zones. Thus there is no longer any kind of global action-angle description of the Hamiltonian (the angles being the canonical coordinates). The integrable regions of phase space are therefore covered by a collection of action-angle variables, each of which is only locally valid within a certain region of phase space. Still, each of the sets of local actions may be quantized, and by doing so it is possible to construct the full EBK spectrum. The problem with this approach is

that quantum-mechanically, tori in the different regions of phase space, i.e., separated by resonance zones, are still coupled to each other. (As evidence for this, the Hamiltonian can be evaluated in the EBK states, and the off-diagonal elements are non-vanishing). The energy flow between such tori is known as Dynamical Tunneling, and it leads to the breaking of degeneracies or near-degeneracies in the EBK energies. The above method of quantizing the local sets of actions fails to take this into account.

An alternative approach is to remain in a global action-angle basis, and to transform to a set of action-angle variables which minimizes the angle dependence of the Hamiltonian. Such a representation is termed an *Intrinsic Resonance Representation* (IRR), a term coined by Carioli et al. [3]. The angular dependence of a Hamiltonian is minimized when the angular terms are all resonant terms of the zeroth-order Hamiltonian. It is impossible to reduce the angular dependence further, since the resonant terms lead to the formation of resonance zones which prevent a global action-angle description of the Hamiltonian.

We then use the IRR tori as a semiclassical basis with which to represent our Hamiltonian in matrix form. Because much of the classical dynamics has already been absorbed into the IRR tori, leaving only the quantum trans-

port across resonance zones, it is possible to obtain the semiclassical energies using a much smaller basis than required with a zeroth-order action-angle representation. Furthermore, physical insight is obtained, since the resulting basis is derived from the underlying dynamics of the system, while the original basis (e.g. harmonic oscillators) is often chosen for computational convenience.

Carioli, Heller, and Moller (CHM) published an algorithm in 1997 to construct the IRR basis from a given Hamiltonian [3]. Their method was a generalization of the Chapman, Garrett, and Miller (CGM) [4] method for finding invariant tori of a nearly separable system. One drawback with the CHM method is that it requires a priori knowledge of which terms in the Hamiltonian are to be considered resonances, and which aren't. The CHM method transforms away the non-resonant terms using an iterative scheme that updates the full Hamiltonian at every iteration step. Convergence only requires a few iterations, and the final Hamiltonian contains only the resonant terms. However, often the terms are not exactly resonant, but nearly resonant. In principle, near-resonances are to be treated like resonances. Unfortunately, this is a perturbation-dependent term, and thus there is a certain ambiguity in the transition from regarding a term as non-resonant to

resonant.

Another drawback with the CHM method is that at each step, it is necessary to evaluate a multidimensional integral and to invert a nonlinear angle map. These features slow the algorithm down, making it difficult to study systems with more than 2 or 3 degrees of freedom.

The previous chapter presented an alternative approach to finding the IRR basis, namely, the GDA method. This method does not require any a priori assignment of potential terms as resonant or non-resonant. At each iteration step every term in the Hamiltonian is adjusted depending on how close it is to being resonant. The method, as implemented in this chapter, is as accurate as the CHM algorithm in obtaining the semiclassical energies. Its main advantage is that it avoids evaluating multidimensional integrals or inverting nonlinear angle maps. Thus, we believe that it is much faster than the CHM method, making it possible to find IRR tori in higher degrees of freedom than previously studied.

This chapter is organized as follows: In Section 2.2, we give a brief review of the CGM method for finding the invariant tori of a non-resonant system. In Section 2.3, we describe the CHM generalization of the CGM method, which allows one to find the IRR tori of a Hamiltonian. In Section 2.4, we write

down the specific form of the H evolution equation for the systems of interest in this chapter. In Section 2.5, we describe the numerical implementation of our method. Finally, in Section 2.6 we present our numerical results. We first begin by demonstrating our method using the same 2-dimensional Hamiltonian which Carioli et al. used to demonstrate the CHM method [3]. We then go on to show that our method can be used to study higher dimensional systems than previously studied, by looking at a 6 dimensional example.

2.2 The CGM Method

The CGM method is an iterative algorithm that finds the invariant tori of some Hamiltonian $H(\theta, \mathbf{J})$. It does this by finding a generating function $S(\theta, \mathbf{I})$, transforming from the action-angles $(\theta, \mathbf{J})$ to $(\phi, \mathbf{I})$, so that $H(\theta, \mathbf{J}) = \tilde{H}(\mathbf{I})$, where $\tilde{H}$ denotes the representation of H in the new action-angle coordinates.

We start with some integrable D - dimensional Hamiltonian $H_0(\mathbf{J})$, to which we add a small perturbation $V(\mathbf{J}, \theta)$, where we can expand V in a

Fourier Series via,

$$V(\theta, \mathbf{J}) = \sum_{\mathbf{k} \neq \mathbf{0}} V_{\mathbf{k}}(\mathbf{J}) e^{2\pi i \mathbf{k} \cdot \theta} \tag{2.2}$$

where $\mathbf{k} = (k_1, \cdots, k_D)$, is a vector of integers [27]. We don't include the zero vector, since this can be absorbed into H_0. Since our perturbation is small, we write $S(\theta, \mathbf{I})$ as $S(\theta, \mathbf{I}) = \mathbf{I} \cdot \theta + G(\theta, \mathbf{I})$, where $G(\mathbf{I}, \theta) = \sum_{\mathbf{k} \neq \mathbf{0}} G_{\mathbf{k}}(\mathbf{I}) e^{2\pi i \mathbf{k} \cdot \theta}$. The new and old action-angle variables are related to each other via,

$$\mathbf{J} = \mathbf{I} + \nabla_\theta G(\theta, \mathbf{I}) \tag{2.3}$$

$$\phi = \theta + \nabla_{\mathbf{I}} G(\theta, \mathbf{I}) \tag{2.4}$$

Therefore, $H(\theta, \mathbf{J}) = H(\mathbf{I} + \nabla_\theta G(\theta, \mathbf{I}), \theta) = \tilde{H}(\theta, \mathbf{I})$. We can expand $\tilde{H}$ in a Fourier Series in θ, writing,

$$\tilde{H}(\theta, \mathbf{I}) = \sum_{\mathbf{n}} \tilde{H}_{\mathbf{n}}(\mathbf{I}) e^{2\pi i \mathbf{n} \cdot \theta} \tag{2.5}$$

where,

$$\tilde{H}_{\mathbf{n}} \equiv \tilde{H}_{\mathbf{n}}[\{G_{\mathbf{k}}\}](\mathbf{I}) = \int H(\theta, \mathbf{I} + \nabla_\theta G(\theta, \mathbf{I})) e^{-2\pi i \mathbf{n} \cdot \theta} d\theta \tag{2.6}$$

where each θ_i is integrated from 0 to 1. The goal of the CGM method is to then choose our $G_{\mathbf{k}}(\mathbf{I})$ so that,

$$\tilde{H}_{\mathbf{n}}[\{G_{\mathbf{k}}\}](\mathbf{I}) = 0, \mathbf{n} \neq \mathbf{0} \tag{2.7}$$

This is done using a Newton-Raphson iteration scheme, at the end of which we have $H(\theta, \mathbf{J}) = \tilde{H}_0(\mathbf{I})$, assuming we obtain convergence.

The beauty of this method is that the actions $\mathbf{I}$ of the final torus are fixed at the start of the algorithm by the user. By setting $\mathbf{I} = 2\pi\hbar(\mathbf{n} + \frac{1}{2})$, we readily obtain the EBK spectrum of the Hamiltonian.

2.3 The CHM Method

The CGM method fails when there are resonances in the Hamiltonian. Because of the formation of resonance zones in the phase space, the CGM representation of the Hamiltonian is a local one, and thus cannot handle quantum effects such as dynamical tunneling. The CHM method, on the other hand, remains in a global action-angle basis even in the presence of resonances. It does this by reducing the angular dependence of the Hamiltonian as much as possible, but not completely, leaving only those angular terms corresponding to resonances and active fast terms.

We illustrate the method in the simplest case, that of a single resonance $\mathbf{r}$. (If $\nu(\mathbf{J})$ denotes the zeroth-order frequencies of the Hamiltonian, then a resonance $\mathbf{r}$ at zeroth-order action $\mathbf{J}$ means that $\nu(\mathbf{J}) \cdot \mathbf{r} = 0$. A two-

dimensional example is if $\nu_1(J_1, J_2) = 2\nu_2(J_1, J_2)$, then $\mathbf{r} = (1, -2)$ is a resonance at (J_1, J_2).) The trick is to break the Hamiltonian into two pieces. The first piece consists of all the non-resonant terms, and may be expressed as,

$$H_{nr}(\theta, \mathbf{J}) = \sum_{\mathbf{n} \neq p\mathbf{r}, p \neq 0} H_{\mathbf{n}}(\mathbf{J}) e^{2\pi i \mathbf{n} \cdot \theta} \tag{2.8}$$

The second piece consists of the resonant terms, and may be expressed as,

$$H_r(\theta, \mathbf{J}) = \sum_{p \neq 0} H_{p\mathbf{r}}(\mathbf{J}) e^{2\pi i p \mathbf{r} \cdot \theta} \tag{2.9}$$

In the CHM method, we apply a modified CGM method to H_{nr} as follows: The Fourier components of H in the new action-angle variables are given by,

$$\tilde{H}_{\mathbf{n}}(\mathbf{I}) \equiv \tilde{H}_{\mathbf{n}}[\{G_{\mathbf{k}}\}](\mathbf{I}) = \int H(\mathbf{I} + \nabla_\theta G(\theta, \mathbf{I}), \theta(\phi, \mathbf{I})) e^{-2\pi i \mathbf{n} \cdot \phi} d\phi \tag{2.10}$$

We use the Newton-Raphson method to solve $\tilde{H}_{\mathbf{n}}[\{G_{\mathbf{k}}\}](\mathbf{I}) = 0, \mathbf{n} \neq p\mathbf{r}, p \neq 0$. At each step of the iteration, the map $\phi^{(n)} = \theta + \nabla_{\mathbf{I}} G^{(n)}(\theta, \mathbf{I})$ is inverted using a procedure developed by Warnock and Ruth [6]. The program is stopped when the non-resonant Fourier components are smaller than some specified error. The resultant Hamiltonian may then be written as,

$$\tilde{H}(\phi, \mathbf{I}) = \sum_p \tilde{H}_{p\mathbf{r}} e^{2\pi i p \mathbf{r} \cdot \phi} \tag{2.11}$$

We then use the resulting tori as a semiclassical basis with which to construct our matrix representation of the Hamiltonian. If we let $|\mathbf{n}\rangle$ denote a basis state corresponding to the torus with actions $\mathbf{I_n} = 2\pi\hbar(\mathbf{n} + \frac{1}{2})$, then the semiclassical coupling $\langle\mathbf{m}|\hat{H}|\mathbf{n}\rangle$ is given by,

$$\hat{H}_{\mathbf{mn}} = H_{\mathbf{m-n}}(\frac{\mathbf{I_m} + \mathbf{I_n}}{2}) \tag{2.12}$$

where $H_{\mathbf{m-n}}$ denotes the $\mathbf{m-n}$ Fourier component of H [9]. This expression neglects contributions from the classically forbidden region; however, if we're working in a regime in which a semiclassical analysis gives accurate results, then we expect such contributions to be small (since the EBK wavefunctions decay rapidly outside the classically allowed region).

In the more general case of multiple resonances, these terms must be included into H_r in order to achieve convergence. It may also be necessary to include near-resonances or even fast terms (in the case of chaotic dynamics).

2.4 The Gradient-Descent Approach

2.4.1 Problems with the CHM Method

There are two main drawbacks to the CHM method: First, the trick of removing resonant terms from the Hamiltonian runs into trouble in the case of near-resonances. For a stronger perturbation, near-resonances and sometimes even fast terms need to be removed in order for the Newton-Raphson method to converge. However, these excluded terms should still be reduced as much as possible, though not necessarily completely. Because the CHM method fails to do this, it is not clear that it will always give the optimal Hamiltonian with a minimized angular dependence. Only in cases where there are few exact or near-resonances, with the other terms highly non-resonant, will the minimized angular dependence be obtained.

The second disadvantage to the CHM method is that at each iteration step it is necessary to invert the angle map and then to evaluate a multi-dimensional integral in order to obtain the updated Fourier components of the Hamiltonian. This feature slows the CHM method down, making it difficult to apply to systems with more than 2 or 3 degrees of freedom.

The way around all these drawbacks is to continuously deform the original

action-angle system via a series of infinitesimal generating functions. Each Fourier component of the Hamiltonian is continuously evolved from some initial value to some final value. The more non-resonant a term, the closer it is brought to zero (where a "resonance" can also mean a fast term that has become active due to the size of the perturbation). Furthermore, by avoiding the need to invert nonlinear functions and to evaluate multidimensional integrals, we can get to the IRR basis much faster than with the CHM method, making it possible to study higher degree of freedom systems (up to $D = 6$ in this chapter and possibly higher).

2.4.2 The Evolution Equation

For what follows, it will prove more convenient to work in an action-angle system in which the angles range from 0 to 2π instead of 0 to 1. The actions $(I_1, \ldots, I_D)$ corresponding to some set of quantum numbers $(n_1, \ldots, n_D)$ are then given by $I_i = \hbar(n_i + \frac{1}{2})$. These values for the actions are more convenient for quantum calculations, since we do not have to deal with an extra factor of 2π, and are thus already in essentially "quantum number" units.

From the previous chapter, the evolution of H in Fourier space for our

action-angle representation is given by,

$$\frac{\partial H_{\mathbf{k}}}{\partial t} = i \sum_{\mathbf{k}'} [(\mathbf{k}' \cdot \nabla_{\mathbf{I}} H_{\mathbf{k}-\mathbf{k}'}) G_{\mathbf{k}'} - ((\mathbf{k} - \mathbf{k}') \cdot \nabla_{\mathbf{I}} G_{\mathbf{k}'}) H_{\mathbf{k}-\mathbf{k}'}] \tag{2.13}$$

where in our modified action-angle system we write,

$$H(\phi, \mathbf{I}) = \sum_{\mathbf{k}} H_{\mathbf{k}} e^{i\mathbf{k}\cdot\phi} \tag{2.14}$$

and similarly for G.

The systems we study are harmonic-oscillator Hamiltonians which are perturbed by some anharmonic terms, since the target systems of this chapter are model vibrational Hamiltonians of polyatomic molecules. As with the example in the previous chapter, the simplest prescription for choosing G is to use $H^{(0)} = H_0 = \mathbf{I} \cdot \omega$, where ω denotes the vector of harmonic-oscillator frequencies. The resulting equation is then,

$$\frac{\partial H_{\mathbf{k}}}{\partial t} = -\sum_{\mathbf{k}'} (\mathbf{k}' \cdot \omega)[(\mathbf{k}' \cdot \nabla_{\mathbf{I}} H_{\mathbf{k}-\mathbf{k}'}) H_{\mathbf{k}'} - ((\mathbf{k} - \mathbf{k}') \cdot \nabla_{\mathbf{I}} H_{\mathbf{k}'}) H_{\mathbf{k}-\mathbf{k}'}] \tag{2.15}$$

2.5 Numerical Implementation of the PDE

2.5.1 Overall Structure of the Algorithm

We begin by choosing our basis of quantum number vectors $\{|\mathbf{n}\rangle\}$. With this basis we generate our Hamiltonian matrix via the semiclassical prescription

$\langle \mathbf{m}|\bar{H}|\mathbf{n}\rangle = H_{\mathbf{m}-\mathbf{n}}(\frac{\mathbf{I_m}+\mathbf{I_n}}{2})$, as described in Eq. (2.12). We thus construct a list $\mathbf{I_r}$ of the actions $\frac{\mathbf{I_m}+\mathbf{I_n}}{2}$ involved in our semiclassical matrix. It is on this discrete set of actions that we will apply our gradient-descent algorithm. At the end of the program, the $H_{\mathbf{n}}(\mathbf{I_r})$ will have been changed to their final values. For each $\mathbf{I_r}$ we also store all the associated $\mathbf{s} \equiv \mathbf{m} - \mathbf{n}$. The final values of $H_{\mathbf{s}}(\mathbf{I_r})$ are then placed into their appropriate positions in the semiclassical matrix, thereby giving us our final Hamiltonian matrix, which we then diagonalize to determine the semiclassical spectrum.

2.5.2 Dynamics at a Given Action

We solve this system of PDEs on a grid of actions about the central action $\mathbf{I}_0$, where our grid consists of all actions $\mathbf{I_k} = \mathbf{I}_0 + DX\mathbf{k}$, with $\mathbf{k} = (k_1, \ldots, k_D)$ satisfying $|k_1| + \ldots + |k_D| \leq GDSZ$. Let us denote this set of grid points as $\Omega(\mathbf{I}_0, GDSZ)$. $GDSZ$ and DX are user-input parameters. At the beginning of evolution, we first compute all the $H_{\mathbf{k}}$ on all the grid points about the action $\mathbf{I}_0$. We can't compute $H_{\mathbf{k}}$ for all vectors $\mathbf{k}$, so we make a user-input cutoff $MAXK$. Thus, we only track those $\mathbf{k}$ for which $|k_1| + \ldots + |k_D| \leq MAXK$. All other $H_{\mathbf{k}}$ are set to 0 throughout the evolution. Furthermore, to

eliminate tracking negligible fast terms we introduce a resonance half-width RHW, and further restrict ourselves to those $\mathbf{k}$ for which $|\mathbf{k} \cdot \omega| < RHW$, where ω is the vector of the zeroth-order harmonic frequencies.

The initial $H_{\mathbf{k}}$ are computed analytically. We start with an initial, zeroth-order action-angle basis of harmonic oscillators. Our Hamiltonian is,

$$H(\mathbf{x}, \mathbf{p}) = \frac{\mathbf{p}^2}{2} + \frac{1}{2}(\omega_1^2 x_1^2 + \ldots + \omega_D^2 x_D^2) + \sum_{N=3}^{M} \sum_{n_1+\ldots+n_D=N} \frac{\alpha_{(n_1,\ldots,n_D)}}{n_1! \cdots n_D!} x_1^{n_1} \cdots x_D^{n_D} \tag{2.16}$$

We take all our masses to be 1, since in a polyatomic molecule, a normal-mode analysis involves a transformation to a system of mass-scaled coordinates in which all the masses become 1. The transformation to harmonic-oscillator action-angle coordinates is then accomplished via

$$x_k = \sqrt{\frac{I_k}{\pi \omega_k}} \cos 2\pi\theta_k \tag{2.17}$$

$$p_k = -\sqrt{\frac{\omega_k I_k}{\pi}} \sin 2\pi\theta_k \tag{2.18}$$

Once the $H_{\mathbf{k}}$ have been determined, we compute all gradients using centered differences, giving us an $O(DX^2)$ accurate estimate. We then propagate forward by one time step of length DT, which is also user-specified. This propagation step is described in Appendix A. Note that we cannot evaluate $\nabla_{\mathbf{I}} H_{\mathbf{k}}$ at the boundary of our grid. Thus, we cannot change the values at

the boundary points. However, all grid points in $\Omega(\mathbf{I}_0, GDSZ-1)$ have been propagated correctly, and so after the first iteration step we only continue propagation at those grid points. Note that after the second iteration we only continue propagating on $\Omega(\mathbf{I}_0, GDSZ-2)$. Continuing this process, we get that after the i^{th} iteration we only continue propagating on $\Omega(\mathbf{I}_0, GDSZ-i)$, and so the total number of iterations cannot exceed $GDSZ$. This scheme avoids the need for imposing artificial boundary conditions on our system. Rather, around each $\mathbf{I}_0$ we have a collapsing boundary inside of which the $H_{\mathbf{k}}$'s are propagated correctly at each time step. Furthermore, since we only care about the values of the $H_{\mathbf{k}}$ at $\mathbf{I}_0$ we may as well set the number of iterations and $GDSZ$ to be equal. For a desired number of iterations, this gives the minimum value of $GDSZ$ possible, which increases the algorithm's speed and minimizes memory requirements.

2.6 Numerical Examples

2.6.1 Two Degrees of Freedom

We first demonstrate our method using the Pullen-Edmonds Hamiltonian [8]

$$H = \frac{p_x^2 + p_y^2}{2} + \frac{1}{2}(\omega_x^2 x^2 + \omega_y^2 y^2) + \epsilon x^2 y^2 \tag{2.19}$$

where we set $\omega_x = \omega_y = 1$ and $\epsilon = 0.05$. This is the system studied by Carioli et. al. [3] in illustrating the CHM method, which is why we shall also use it to illustrate our method, so that there is a frame of reference for comparison.

In Figure 2.1 we give a contour plot of this Hamiltonian at energies $E = 5, 10, \ldots 50$. This system has four symmetry axes, giving rise to four modes of oscillation: Two "local" modes, corresponding to oscillation along the x and y axes, and two "normal" modes, corresponding to oscillation along the lines $y = \pm x$. There is strong dynamical tunneling between the "local" modes in the quasi-integrable regime that leads to a quantum-mechanical breaking of the degeneracy in the spectrum.

Following Carioli et al., we looked at those quantum states (n_1, n_2) satisfying $n_1 + n_2 = 8$. This gives us nine-fold degenerate states with zeroth-order energy $E = 9$. The system is in the quasi-integrable regime at this energy. If

we count up from the ground-state $(0,0)$, then we find that these nine states are states 37 to 45 of our system.

Upon introducing the anharmonic coupling term to our system, the degeneracy of these states is broken, giving the quantum-mechanical energies listed in the second column of Table 2.1. These energies were obtained by diagonalizing all states from the ground state up to a total of sixteen quanta.

We next diagonalized only the 9×9 block of our nine-fold degenerate states using the harmonic-oscillator tori as our semiclassical basis. The results are listed in the third column of Table 2.1. Note the significant discrepancy between these energies and the exact semiclassical energies. (By exact semiclassical energies we mean the energies obtained using the same harmonic basis used to obtain the quantum energies, but using the semiclassical couplings instead of the quantum ones.) We applied our GDA method to these nine degenerate states, using $DT = 0.02$, $DX = 0.02$, $MAXK = 8$, $RHW = 8.1$ and $GDSZ = 17$. The results are listed in the fourth column of Table 2.1. Note that the discrepancy with the exact semiclassical energies has been drastically reduced.

Carioli et al. also performed a sweep of ω_x from 0.99 to 1.01 to look at the avoided crossing between states 39 and 40. In Figure 2.1 we show the semi-

State	QM	Harmonic Basis	IRR Basis
37	9.15484	9.17307	9.15260
38	9.15772	9.18118	9.15589
39	9.38058	9.41995	9.37790
40	9.42650	9.50448	9.42591
41	9.51662	9.59045	9.51677
42	9.68594	9.84382	9.69006
43	9.69868	9.85193	9.70200
44	10.01294	10.27364	10.01958
45	10.01330	10.27399	10.01964

Table 2.1: 2 Degree-of-Freedom Example. Energies of states 37 to 45 obtained by various methods. Column 2: Quantum-mechanical. Column 3: 9 X 9 block diagonalization in the harmonic-oscillator torus basis. Column 4: 9 X 9 block diagonalization in the IRR basis.

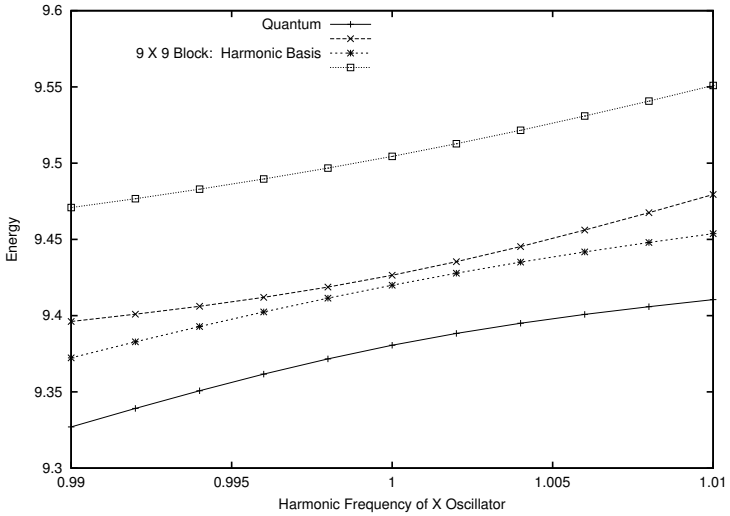

Figure 2.1: Avoided crossing between states 39 and 40 as a function of ω_x. The curves here are the quantum energies and the energies obtained by diagonalizing the 9 X 9 block in the harmonic-oscillator torus basis.

classical energy curves for the two states, along with the curves obtained by diagonalizing the 9×9 block using the harmonic-oscillator tori as our basis. In Figure 2.2 we also show the semiclassical energy curves for the two states, along with the curves obtained by applying our gradient-descent method to our zeroth-order nine-fold degenerate basis (with the same program parameters as before). Note that the discrepancy present in Figure 2.1 has been eliminated. To be sure, the match is not exact, but the differences cannot be

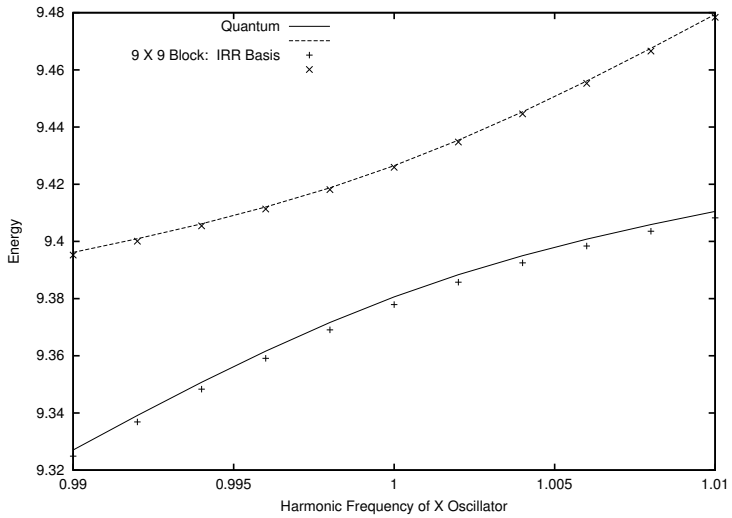

Figure 2.2: Avoided crossing between states 39 and 40 as a function of ω_x. The curves here are the quantum energies and the energies obtained by diagonalizing the 9 X 9 block in the IRR torus basis.

seen at the resolution level of the plot.

2.6.2 Six Degrees of Freedom

We conclude this section by looking at a 6 degree-of-freedom example. As with the 4-dimensional example, the Hamiltonian we chose was a generalization of the Pullen-Edmonds system. We took,

$$H = \frac{1}{2}\sum_{k=1}^{6}(x_k^2 + p_k^2) +$$

$$0.05(0.93x_1^2x_2^2 + 0.94x_1^2x_3^2 + 0.95x_2^2x_3^2 +$$
$$0.96x_1^2x_4^2 + 0.97x_2^2x_4^2 + 0.98x_3^2x_4^2 +$$
$$0.99x_1^2x_5^2 + 1.00x_2^2x_5^2 + 1.01x_3^2x_5^2 +$$
$$1.02x_4^2x_5^2 + 1.03x_1^2x_6^2 + 1.04x_2^2x_6^2 +$$
$$1.05x_3^2x_6^2 + 1.06x_4^2x_6^2 + 1.07x_5^2x_6^2) \tag{2.20}$$

We initially tried to obtain the exact quantum and semiclassical energies of the states with a total of 8 quanta in the unperturbed limit. While applying our method to this basis would not have been a problem, we would not have been able to generate the exact quantum and semiclassical energies required for comparison. As with the 2 and 4-dimensional cases, we would have had to diagonalize all states up to a total of sixteen quanta to get the higher-order accuracy desired. The resulting basis was simply too large for our computer to handle, and so we had to retreat to a more manageable example. We thus looked at those quantum states $(n_1, n_2, n_3, n_4, n_5, n_6)$ satisfying $n_1+n_2+n_3+n_4+n_5+n_6 = 4$, giving us 126 degenerate states with a zeroth-order energy of $E = 7$. Counting from the ground-state as before, we get that these are states 85 to 210 of our system.

The quantum energies were then obtained by diagonalizing all states up

to a total of eight quanta. The results are listed in the second column of Table 2.2, respectively. We don't list all 126 energies, but rather only a representative sample. Proceeding as before, we then diagonalized only the 126×126 block of degenerate states, using the zeroth-order harmonic oscillator tori as our basis. The results are given in the third column of Table 2.2. Finally, we applied our gradient-descent algorithm to this degenerate basis. Using $MAXK = 8$ gave us so many resonances and fast terms that the run-time was prohibitively slow. So, we sacrificed accuracy for speed and used the parameters $DT = 0.04$, $DX = 0.02$, $MAXK = 4$, $RHW = 4.1$, and $GDSZ = 3$ (we did not make $GDSZ$ sufficiently large to reach the optimal basis, because the run-time would have again been prohibitively slow). The results are given in the fourth column of Table 2.3. Notice that although we significantly reduced the number of available resonances and fast terms, we still managed to cut the initial energy discrepancy from an average of 2.0% to an average of 0.3%. This corresponds to an average reduction in the initial error by 84%.

State	QM	Harmonic Basis	IRR Basis
85	7.51738	7.60062	7.52752
86	7.53165	7.62199	7.54476
87	7.53514	7.62543	7.54754
88	7.54076	7.62990	7.55114
89	7.54968	7.63708	7.55695
90	7.56073	7.64847	7.56620
205	7.88131	8.11856	7.92644
206	7.88220	8.12106	7.92820
207	7.88444	8.12353	7.92994
208	7.88726	8.12685	7.93226
209	7.88783	8.13189	7.93579
210	7.92544	8.19989	7.98158

Table 2.2: 6 Degree-of-Freedom Example. A sample of energies of states 85 to 210 obtained by various methods. Column 2: Quantum-mechanical. Column 3: 126 X 126 block diagonalization in the harmonic-oscillator torus basis. Column 4: 126 X 126 block diagonalization in the IRR basis.

2.6.3 Discussion

Notice that in all our examples, just using the degenerate basis of harmonic-oscillator tori did not give us a good estimate of the semiclassical energies. It was necessary to diagonalize all states within a much wider energy band to do so. Although harmonic oscillators are probably the easiest basis states to use for the potentials of interest to us in this chapter, it is generally a mistake to attach a mechanism to the energy flow associated with this basis. In Stuchebrukhov and Marcus [10], using a harmonic-oscillator basis to study $0.01 - 0.1$ cm^{-1} energy splittings in a polyatomic molecule with 42 vibrational degrees of freedom, they had to diagonalize all states within an energy band of 10 cm^{-1} or more. They invoked the concept of a "superexchange" mechanism, whereby energy flow between nearly degenerate states, but distantly separated in the quantum number space, occurred via energy flow between states closer to each other in the quantum number space but with a larger energy gap between them. This "superexchange" mechanism is a basis-dependent notion, however, as is most simply illustrated by our 2 degree-of-freedom example. To obtain the semiclassical energies of states 37 to 45, with a total energy range < 1, we had to diagonalize a much larger

basis of 153 states with a total energy range of > 20. We could also invoke a "superexchange" mechanism for this energy flow. Indeed, shrinking our basis did give a small change in the energies (though only in the last one or two decimal places), so that one could argue that our perturbation is sufficiently strong to allow for such a mechanism. However, as is clear by applying our GDA method, a more accurate explanation is while a superexchange mechanism is required to account for energy flow in the harmonic basis, there exists a basis obtainable from the underlying classical dynamics of the system, namely the IRR tori, in which the superexchange mechanism need not be invoked. Using the IRR tori we were able to obtain our nine semiclassical energies using a much smaller basis which also lies within the energy range of our semiclassical spectrum. The "superexchange" mechanism is thus an artifact, coming from the fact that our zeroth-order basis of harmonic-oscillators is not the optimal basis of IRR tori.

Carioli et al. made one additional plot in their paper, in which they applied their CHM method in the chaotic regime, with $E = 50$. To obtain convergence of their method, they had to also include the fast terms arising from the vector $\mathbf{s} = (1, 1)$. The IRR representation of the Hamiltonian was no longer block diagonal, though the coupling structure was still simplified

somewhat. For this reason, we decided to forgo our own study at $E = 50$. At best, our algorithm would simplify the coupling structure as well, so that a smaller basis would be required to obtain the semiclassical spectrum. In the chaotic regime, however, semiclassical quantization no longer occurs only on the invariant tori (due to ergodic regions of phase space of area significantly larger than $(2\pi\hbar)^D$), so that the IRR basis is no longer optimal. Another way of looking at this is that since our matrix is no longer block diagonal (though with a simplified coupling structure), we have to invoke the "superexchange" mechanism in order to account for the observed energies. At this point, we may as well use harmonic oscillators.

In the end, the use of invariant tori as a semiclassical basis for quantum calculations is most useful at relatively low energy, where the dynamics is quasi-integrable. It is in this regime that the IRR basis is expected to be most physically motivatived, and consequently leads to a significantly smaller basis, as well as giving physical insight.

2.7 Conclusions and Future Research

In this chapter we applied the GDA method for finding the IRR basis of a Hamiltonian system. We started in a harmonic action-angle representation of the Hamiltonian, and continuously deformed our initial action-angle basis into an optimal basis of tori in which the angular dependence of the Hamiltonian was minimized. The advantage of the gradient-descent approach is that formally it does not distinguish between resonances and fast terms, so that all potential terms are evolved in a uniform fashion and reduced as much as possible. The CHM method, on the other hand, requires an a priori decision as to which terms are to be treated as resonances and which are going to be incorporated into creating the final tori. In the case of near-resonances this distinction is blurred, and depends on the strength of the perturbation. In the chaotic regime, even fast terms may need to be treated as resonances. Although no speed comparisons were made, we believe that our method is also faster, since we don't have to evaluate any integrals or invert the angle map. Thus, our method can be used to study higher dimensional systems (up to $D = 6$ and maybe even higher). However, like the CHM method, our method, as currently implemented, assumes a small perturbation on a

zeroth-order integrable Hamiltonian.

Our future goal is to determine the structure of the matrices in the IRR basis. The greatest advantage of the IRR representation is that it incorporates much of the classical mechanics into the invariant tori, thereby making possible the isolation of residual quantum effects such as dynamical tunneling. An understanding of the couplings between the IRR tori will reveal how the tunnel couplings behave. This could in turn be used to understand phenomena such as localization of the tunneling, or if the perturbation is sufficiently strong, ergodicity over the energy hypersurface due to dynamical tunneling.

It has been mentioned in this chapter that in the quasi-integrable regime, the couplings between the IRR tori correspond to dynamical tunneling in the semiclassical limit. Because the presence of resonances prevent the elimination of the IRR couplings $H_{\mathbf{m-n}}$, it has been argued in Ref. 7 that it is the formation of resonance zones in the phase space which facilitates the tunneling. In a Poincare surface of section, the phase space surrounding a hyperbolic fixed point in the resonance zone looks much like the phase space for the one-dimensional above-barrier reflection problem [7, 11], which is a prime example of dynamical tunneling.

Classically, however, in 3 or more dimensions, Arnol'd Diffusion can cause energy transport between the tori. A trajectory can travel along the Arnol'd Web in the chaotic interstices between the tori, and may very well be ergodic over the energy hypersurface. Thus, in higher dimensions, a numerical study to determine whether the IRR couplings are primarily due to tunneling or to Arnol'd Diffusion is necessary. The general consensus is that Arnol'd Diffusion is slow and localizes quantum-mechanically [7, 13]. A numerical study of this phenomenon is still warranted before making the claim that the IRR tori are coupled by dynamical tunneling with certainty.

Before concluding, it seems appropriate to briefly discuss the utility of the IRR approach in general, and the PDE implementation of it in particular, as a numerical method for quantum calculations. After all, it is usually easier and faster to use a convenient zeroth-order basis and simply diagonalize a large basis set. The PDE method is cumbersome by comparison, requiring more sophisticated mathematical and numerical machinery.

As the dimensionality of a system increases, the basis set required for a direct zeroth-order diagonalization could be too large for the computer to handle. As mentioned in subsection 2.6.2, we already encountered this problem in our numerical tests. The IRR approach can significantly reduce the

size of the basis required to obtain the desired energies, to a point where this basis can easily be stored and diagonalized on the computer. Thus, while slower than direct diagonalization, this approach may be useful as a numerical method in cases where the required zeroth-order basis set size is simply too large for the computer to handle. The IRR approach has the additional advantage that the reduced basis is more physically motivated than the zeroth-order basis, since the IRR basis is extracted from the underlying classical dynamics of the system.

Chapter 3

Dynamical Tunneling Versus Arnol'd Diffusion: A Comparison of Quantum and Classical Energy Flow Rates

This chapter attempts to resolve the issue of the nature of the $0.01-0.1$ cm^{-1} peak splittings observed in high-resolution IR spectra of polyatomic molecules. It is believed that these splittings are caused by dynamical tunneling, a

quantum-mechanical phenomenon whereby energy flows between two regions of phase-space at a rate generally much faster than predicted by classical mechanics. However, a possible classical mechanism for the energy flow is Arnol'd Diffusion, which connects different regions on the energy hypersurface by a resonance network known as the Arnol'd Web. Using a simple, yet physically relevant, Hamiltonian, we compare dynamical tunneling rates with Arnol'd Diffusion, which is shown to be much slower than dynamical tunneling.

3.1 Introduction

An unresolved question in the physical chemistry community is the nature of the $0.01 - 0.10\ \mathrm{cm}^{-1}$ peak splittings that have been observed in high-resolution IR spectra of polyatomic molecules [7, 10]. These splittings are indicative of energy flow in the phase space of the molecule, induced by weak residual anharmonic couplings, and contain information on the long-time dynamics of the molecules. One hypothesis has been that the mechanism for this peak splitting is due to dynamical tunneling, though no definitive proof has yet been given [7].

Part of the problem in elucidating the mechanism of Intramolecular Vibrational Redistribution (IVR) is that it is first necessary to define a set of structures between which the energy redistribution occurs. Indeed, it may be argued that redistribution of energy is an artifact, since in the quantum-mechanical eigenbasis of the system, no redistribution occurs at all. This can be seen by noting than an eigenstate $|\psi\rangle$ of energy E of some Hamiltonian evolves according to $|\psi\rangle_t = e^{-iEt/\hbar}|\psi\rangle$. Thus, redistribution is a basis-dependent notion.

A natural basis from which to define energy redistribution is given by the invariant tori of the Hamiltonian. The vibrational Hamiltonians of polyatomics are given by harmonic-oscillators plus anharmonic terms. The anharmonicities are small in the low quantum-number regime, which is generally the regime probed by experimentalists in IR spectroscopy. Thus, the KAM Theorem assures that almost all of the phase-space is filled with invariant tori [26, 28]. Semiclassically, one may associate quantum-mechanical wavefunctions with the invariant tori of actions $(I_1, \ldots, I_D) = 2\pi\hbar(n_1 + \alpha_1/4, \ldots, n_D + \alpha_D/4)$. Here the n_i are nonnegative integers, and the α_i are the Maslov indices, which are usually equal to 2. The semiclassical energy spectrum is then obtained by setting $E(n_1, \ldots, n_D) = H(I_1, \ldots, I_D)$, where H denotes

the Hamiltonian.

The method just described is the Einstein-Brillouin-Keller (EBK) quantization method, and the point is that, even for nearly integrable systems, it is still possible to semiclassically find a set of good quantum numbers $(n_1, \ldots, n_D)$ characterizing the energy spectrum. Spectroscopists attempt to determine the functional form of the energy dependence on the quantum numbers by fitting the spectral peaks to an expansion,

$$E(n_1, \ldots, n_D) = E_0 + \sum_{i=1}^{D} a_i n_i + \sum_{i,j \geq i} a_{ij} n_i n_j + \sum_{i,j \geq i, k \geq j} a_{ijk} n_i n_j n_k + \ldots \quad (3.1)$$

What happens for medium-sized polyatomics is that energy flow between the tori destroys the good quantum numbers and leads to spectroscopically unassignable peaks. The peak splittings are sufficiently narrow that they are the result of long-time dynamics, on the order of thousands to hundreds of thousands of vibrational periods of the molecule. One possible culprit is mode mixing, whereby the peak splittings are the result of the formation of new "normal" modes. The relative strength of the different peaks is a measure of the relative contribution of the different "local" modes to the overall "normal" modes. In the language of classical mechanics, one would say that the peak splittings indicate that the vibrational dynamics reside on

invariant tori lying inside resonance zones generated by the Hamiltonian. The main problem with this analysis is that these peak splittings are ubiquitous, and are already seen at low quantum numbers (3 and often less). At such low quantum numbers the anharmonicities in the vibrational Hamiltonian are sufficiently small that the resonance zones should occupy only a small fraction of the total phase-space volume. Thus, it is improbable that invariant tori residing in the resonance zones could support a significant fraction of the vibrational eigenstates.

By similar reasoning, classical chaos is likely also an insufficient mechanism accounting for the peak splittings. While such a mechanism would be expected to dominate for large quantum numbers, the quasi-integrable regime is the regime of interest in this paper. The remaining mechanism accounting for the peak splittings is flow between the invariant tori residing outside the resonance zones. Because the splittings are indicative of long-time dynamics, they are believed to be quantum-mechanical in nature, i.e., dynamical tunneling. However, for systems with more than two degrees of freedom, another type of long-time classical transport between invariant tori is possible: Arnol'd Diffusion. Arnol'd Diffusion occurs when a trajectory moves along a resonance until it intersects a second resonance, at which point it

moves along the second resonance. In general, the resonance structure of the Hamiltonian forms a network known as the Arnol'd Web. In principle, by navigating the Arnol'd Web, a trajectory can ergodically traverse the entire energy hypersurface [7, 26].

Nevertheless, it is believed that dynamical tunneling dominates Arnol'd Diffusion, for several reasons. First of all, dynamical tunneling already occurs in systems with two degrees of freedom, while Arnol'd Diffusion is only a possible mechanism in three degrees of freedom and higher. Second, Arnol'd Diffusion has been shown analytically to be rather slow, with a diffusion coefficient that scales as $e^{-c|\Delta\omega_{\mathbf{m}}|/\sqrt{\epsilon}}$, where ϵ denotes the perturbation strength, and $\Delta\omega_{\mathbf{m}}$ is known as the resonance detuning [35, 37]. Finally, studies by Wolynes and co-workers on a quantized stochastic pump model of Arnol'd Diffusion suggest that Arnol'd Diffusion localizes quantum-mechanically [13, 26, 32, 33, 34, 36].

It should be emphasized here that comparisons between dynamical tunneling and Arnol'd Diffusion must be made in the few quantum-number regime. The reason for this is that for sufficiently high quantum numbers, quantum effects become unimportant, so Arnol'd Diffusion would be expected to dominate any tunneling effects. An excellent example of this is

the solar system, where it is believed that Arnol'd Diffusion is responsible for certain aspects of the structure of the asteroid belt between Mars and Jupiter. Dynamical tunneling is not expected to be important in explaining macroscopic features of our solar system. However, for IR studies on polyatomic molecules, the few quantum-number regime is exactly the regime being probed. It is expected that quantum effects are important for these types of systems, and so a comparison between dynamical tunneling and Arnol'd Diffusion rates is warranted.

However, in comparing quantum and classical energy flow rates, two key issues need to be properly addressed. First of all, does one include zero-point energy into the classical calculations? The problem is that in order to have a proper semiclassical simulation, zero-point energy must be taken into account. However, for a sufficiently large number of vibrational degrees of freedom, the zero-point energy may be so large that classically the molecule can dissociate, even in its ground state. Secondly, it is necessary to develop a criterion which can distinguish between genuine Arnol'd Diffusion and energy flow which is simply due to mode mixing. This is not necessarily a trivial point, since realistic systems have such a large density of states that it becomes difficult to track which resonances are active at any given time.

The solution to both problems is the construction of a synthetic Hamiltonian which does not classically dissociate with the inclusion of the zero-point energy, and which has an easily constructible Arnol'd Web, making it a simple matter to detect Arnol'd Diffusion. In this paper we present numerical studies on a such a Hamiltonian, which support the consensus view that dynamical tunneling is likely significantly faster than Arnol'd Diffusion, and hence the main cause of the fine peak splittings observed in IR spectra. Though constructed by hand, the Hamiltonian we present has a number of characteristics in common with vibrational Hamiltonians.

This chapter is organized as follows: In Section 3.2 we present the Hamiltonian which we will use for our subsequent calculations, and show how to construct its Arnol'd Web. In Section 3.3 we describe both the classical and quantum calculations, and how we compare dynamical tunneling and Arnol'd Diffusion rates with the results of the calculations. In Section 3.4 we present the Results and Discussion. In Section 3.5 we discuss the quantum analogue of Arnol'd Diffusion as a mechanism for the quantum energy flow. In Section 3.6 we consider the issue of localization in our model. Finally, we conlude in Section 3.7 with a summary of our main results and a discussion of future research plans.

3.2 The Hamiltonian

3.2.1 Equation and Definition of Parameters

We will work with the D-dimensional Hamiltonian, given in action-angle variables by,

$$H(\phi_1, \ldots, \phi_D, I_1, \ldots, I_D) = H_0(I_1, \ldots, I_D) + \lambda V(\phi_1, \ldots, \phi_D, I_1, \ldots, I_D) \tag{3.2}$$

where

$$H_0(I_1, \ldots, I_D) = \sum_{i=1}^{D} (\alpha_i I_i - \beta_i I_i^2) \tag{3.3}$$

and

$$V(\phi_1, \ldots, \phi_D, I_1, \ldots, I_D) = \sum_{i<j} \gamma_{ij}(I_i, I_j) \cos(\phi_i - \phi_j) \tag{3.4}$$

We then define,

$$\alpha_{2n-1} = \alpha + 2\beta I_0 \tag{3.5}$$

$$\alpha_{2n} = \alpha - 2\beta(I_0 + \Delta I) \tag{3.6}$$

$$\beta_{2n-1} = \beta \tag{3.7}$$

$$\beta_{2n} = -\beta \tag{3.8}$$

where α, β, I_0 and ΔI are specified constants.

The above Hamiltonian resembles a Morse-Oscillator Hamiltonian with nonlinear coupling between the local modes. Following this analogy, we define $\alpha = \omega$, where ω is some specified harmonic frequency, and $\beta \equiv \omega^2/4D_e$, where D_e denotes a dissociation energy. We also consider three different forms for the γ_{ij}. We begin by defining $\gamma(I_1, I_2) = (1 - e^{-I_1/I_c})(1 - e^{-I_2/I_c})$. Then Coupling Scheme I is defined by setting $\gamma_{ij}(I_i, I_j) = \gamma(I_i, I_j)$ if and only if $|i - j| = 1$. Coupling Scheme II is defined by setting $\gamma_{ij}(I_i, I_j) = \gamma(I_i, I_j)$ if and only if i, j are of different parity, i.e., if $i + j$ is odd. Finally, Coupling Scheme III is defined by setting $\gamma_{ij}(I_i, I_j) = \gamma(I_i, I_j)$ for all $i \neq j$.

The motivation for the definition of the γ_{ij} is as follows: We want the resonance structure of the full Hamiltonian to be essentially dictated by the zeroth-order Hamiltonian. Thus, we want $\dot{\phi} \approx \nabla_{\mathbf{I}} H_0$, which means that we need $\nabla_{\mathbf{I}} V \approx 0$. At the same time, we want the dynamics to be such that the $I_i \geq 0$ at all times. Thus, we want $\dot{I}_i = 0$ if $I_i = 0$. Note that $\gamma(I_1, I_2)$ satisfies these requirements. If $I_1, I_2 >> I_c$, then $\gamma(I_1, I_2) \approx 1$, so $\nabla_{\mathbf{I}} V \approx 0$, while if I_1 or I_2 are equal to 0, then $\gamma(I_1, I_2) = 0$, so for the corresponding I_i we get $\dot{I}_i = 0$. By choosing I_c sufficiently small compared to the characteristic actions of our simulations, we can make the region of phase-space whose resonance structure is dictated by the zeroth-order Hamiltonian as large as

possible.

3.2.2 The Arnol'd Web

We may now use the zeroth-order Hamiltonian to construct the Arnol'd Web for our system. Letting $\{\hat{\mathbf{e}}_1, \ldots, \hat{\mathbf{e}}_D\}$ denote the canonical basis of $\mathbf{R}^D$, we obtain that $I_0\mathbf{1} + (\Delta I - I)\hat{\mathbf{e}}_{2m} + I\hat{\mathbf{e}}_{2n+1}$ is a $(1, -1)$ resonance line. To be specific, $(I_0 + \Delta I - I, I_0 + I, I_0, \ldots, I_0)$ is a $(1, -1)$ resonance. Thus, starting at $(I_0 + \Delta I, I_0, \ldots, I_0)$, the system can evolve until the ΔI units of action have been resonantly transferred into mode 2. At this point, the system is in state $(I_0, I_0 + \Delta I, I_0, \ldots, I_0)$, and now the $(I_0, I_0 + \Delta I - I, I_0 + I, I_0, \ldots, I_0)$ resonance line has become active. The system can now proceed to transfer energy to mode 3, in principle evolving to the state $(I_0, I_0, I_0 + \Delta I, I_0, \ldots, I_0)$. This energy transfer from mode 1 to mode 3 is accomplished via Arnol'd Diffusion, because the energy transfer occurs first along the resonance between modes 1 and 2. During this resonant energy transfer, $H, I_1 + I_2, I_3, \ldots, I_D$ are conserved. Once ΔI units of action have been transferred to mode 2, the mode 1 - mode 2 and the mode 2 - mode 3 resonance lines intersect, and then energy transfer can occur from mode 2 to mode 3. During this period,

$H, I_1, I_2 + I_3, I_4, \ldots, I_D$ are conserved. By definition, this process is nothing other than Arnol'd Diffusion, since the energy transfer from mode 1 to mode 3 occurred by moving along the resonance web.

Figure 3.1 shows a sample trajectory with $D = 3$. Note that at any given time, either $I_1 + I_2$ and I_3 remain essentially constant, or I_1 and $I_2 + I_3$ remain essentially constant. Thus, the system moves into different resonance zones via Arnol'd Diffusion.

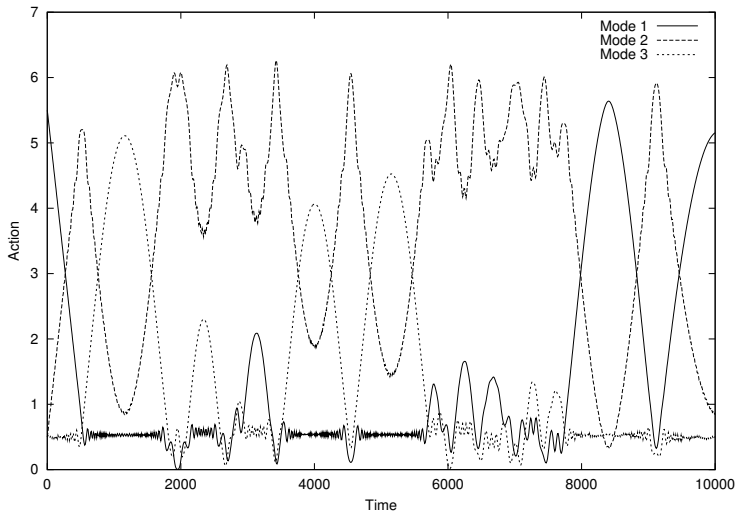

Figure 3.1: Sample trajectory for $D = 3$ showing Arnol'd Diffusion.

Coupling Scheme I only allows for sequential resonant energy transfer. That is, energy can only flow from mode 1 to mode 2 to mode 3, and so

on. Coupling Schemes II and III allow for resonant energy transfer between any two modes of opposite parity. The resulting Arnol'd Webs illustrating the network of resonant energy flow paths for the various schemes is given in Figure 3.2. Note that Coupling Scheme I results in a simple chain, while Coupling Schemes II and III produce an actual web. This web becomes more dense with increasing D.

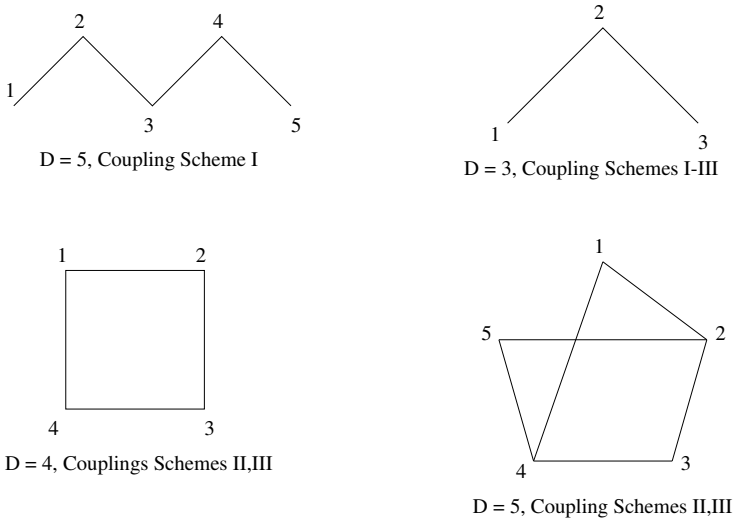

Figure 3.2: Illustration of Arnol'd Webs for various coupling schemes and degrees of freedom.

Care must be taken to choose λ sufficiently small so that the system is indeed quasi-integrable at the energy being studied. If λ is too large,

then rapid energy flow becomes possible via nonresonant chaotic dynamics, which can then account for both classical and quantum energy flow. For our simulations, we set $\lambda = 0.01$. As Figure 3.1 shows, there is essentially no non-resonant energy transfer for this value of the perturbation strength. For $\lambda = 0.1$, a similar inspection of the classical trajectories reveals some non-resonant energy transfer, but overall this is still small, and Arnol'd Diffusion remains essentially the only mechanism for energy flow between resonance zones. The main difference between $\lambda = 0.01$ to $\lambda = 0.1$ is a shortening of the time scales over which the Arnol'd Diffusion occurs. However, already for $\lambda = 1.0$ the dynamics becomes chaotic. While the resonance structure of the Hamiltonian still dictates the dynamics somewhat, the perturbation is sufficiently strong that non-resonant energy flow becomes significant.

Before concluding this section, it should be also pointed out that there is a possibility in our model for some of the frequencies $\omega_i(\mathbf{I}) = \alpha_i - 2\beta_i I_i$ to become negative. For a given value of D, it is possible to choose I_0, ΔI such that all frequencies remain positive during the evolution, corresponding to bound motion at all times. We begin by pointing out that $\sum_{i=1}^{D} I_i$ is conserved by the Hamiltonian, so since our perturbation was chosen so that $I_i \geq 0$ at all times, it follows that $0 \leq I_i \leq \Delta I + DI_0$. For the odd-numbered

modes, $\omega_i(\mathbf{I})$ can become negative if $\alpha - 2\beta(\Delta I + (D-1)I_0) \leq 0 \Rightarrow \alpha/2\beta \leq \Delta I + (D-1)I_0$. For the even-numbered modes, $\omega_i(\mathbf{I})$ can become negative if $\alpha - 2\beta(I_0 + \Delta I) \leq 0 \Rightarrow \alpha/2\beta \leq \Delta I + I_0$. Therefore, assuming $D \geq 2$, we must have $\alpha/2\beta \geq \Delta I + (D-1)I_0$ in order to ensure bound motion. Using the values of α, β in terms of ω, D_e, we get,

$$2D_e \geq \omega(\Delta I + (D-1)I_0) \tag{3.9}$$

3.3 Method of Calculation

In this section, we describe how we compare quantum and classical energy flow rates, and the way this is translated into a comparison of dynamical tunneling vs. Arnol'd Diffusion.

3.3.1 Overview

We run our simulations starting from the torus with quantum numbers $(5, 0, \ldots, 0)$. We let the angles run from 0 to 2π, so the conversion from quantum numbers $(n_1, \ldots, n_D)$ to actions $(I_1, \ldots, I_D)$ is accomplished via $I_i = \hbar(n_i + \frac{1}{2})$. Thus, we have $I_0 = \hbar/2$, $\Delta I = 5\hbar$. For Coupling Scheme I, action can only get into modes 3 and higher via Arnol'd Diffusion. We may

thus plot $\langle I_3(t)\rangle, \ldots, \langle I_D(t)\rangle$ both classically and quantum-mechanically to determine the relative rates of dynamical tunneling and Arnol'd Diffusion for Coupling Scheme I. For Coupling Schemes II and III, action can only get into the odd numbered modes 3 and higher via Arnol'd Diffusion. We may thus plot $\langle I_3(t)\rangle, \langle I_5(t)\rangle, \ldots$ both classically and quantum-mechanically to determine the relative rates of dynamical tunneling and Arnol'd Diffusion.

For all of our simulations, we took $\hbar = 1$, $\lambda = 0.01$, $\omega = 1.0$, $D_e = 5.0$, and $I_c = 0.1$. The condition that we have only bound-state motion becomes, $10 \geq 5 + (D-1)/2$, which gives, $D \leq 11$. Thus, we can run calculations up to 11 degrees of freedom without fear of dissociation. The choice of λ was such that the system was sufficiently quasi-integrable at the energies studied that nonresonant chaotic dynamics was not an issue. This is illustrated in Figure 3.1, where it clear that for this choice of λ, only Arnol'd Diffusion can lead to significant energy redistribution between all three modes. As discussed previously, making λ an order of magnitude larger leads to dynamics showing the first signs of significant non-resonant energy transfer. By making the time steps sufficiently small, we were able to accurately propagate the trajectories out to a time of 2000, which was sufficient to compare the classical and quantum energy flow rates.

3.3.2 Classical Calculations

To determine $\langle I_i(t) \rangle$ classically, we average out $I_i(t)$ for a swarm of trajectories with actions of the initial torus, but differing initial angles. We considered initial angle vectors $(\phi_1, \ldots, \phi_D) = (2\pi i_1/N, \ldots, 2\pi i_D/N)$, where each $i_k = 0, \ldots, N-1$, giving N^D initial trajectories. To determine the optimal N to use, we ran a $D = 3$ calculation and plotted $\langle I_3(t) \rangle$ for $N = 4$, 8, 16, and 32. The results are plotted in Figure 3.3. We deemed the $N = 16$ run sufficiently converged so that we used it for all of our calculations, except for the $D = 5$ simulations. In this case, $N = 16$ required too many trajectories, making the run time prohibitively slow. For $D = 5$, we therefore took $N = 8$. As Figure 3.3 shows, for $N = 8$ the run is not quite converged, but the curve is nevertheless rather smooth, and does not fluctuate greatly from the $N = 16$ or $N = 32$ results.

3.3.3 Quantum Calculations

The quantum results are obtained by solving the time-dependent Schrodinger equation, first by semiclassically quantizing the Hamiltonian. To do this, we consider a basis set of EBK states given by the collection of quantum

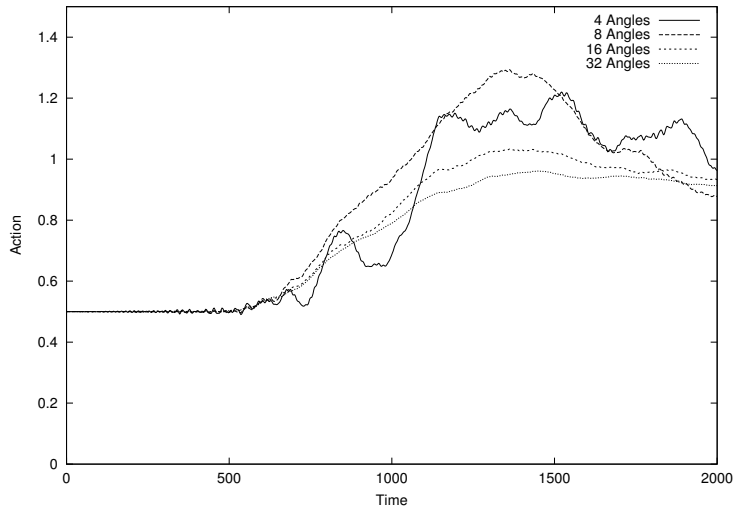

Figure 3.3: Convergence of calculations for $D = 3$.

number vectors $\{(n_1, \ldots, n_D)\}$ corresponding to the actions $\{(I_1 = \hbar(n_1 + \frac{1}{2}), \ldots, I_D = \hbar(n_D + \frac{1}{2})\}$. The zeroth-order energy of the state $|n_1, \ldots, n_D\rangle$ is given by $E_0(n_1, \ldots, n_D) = H_0(I_1, \ldots, I_D)$, and the coupling between two states $|\mathbf{m}\rangle = |m_1, \ldots, m_D\rangle$, $|\mathbf{n}\rangle = |n_1, \ldots, n_D\rangle$ is given by [9],

$$\langle \mathbf{n}|\hat{H}|\mathbf{m}\rangle = H_{\mathbf{n}-\mathbf{m}}(\frac{\mathbf{I_m} + \mathbf{I_n}}{2}) \tag{3.10}$$

where $\mathbf{I_m} = (I_{m_1}, \ldots, I_{m_D}) \equiv (\hbar(m_1+\frac{1}{2}), \ldots, \hbar(m_D+\frac{1}{2}))$, and $\mathbf{I_n} = (I_{n_1}, \ldots, I_{n_D}) \equiv (\hbar(n_1+\frac{1}{2}), \ldots, \hbar(n_D+\frac{1}{2}))$. Also, $\tilde{H}_{\mathbf{k}}$ denotes the $\mathbf{k}$ component in the Fourier expansion of H, given by $H(\phi, \mathbf{I}) = \sum_{\mathbf{k}} \tilde{H}_{\mathbf{k}}(\mathbf{I}) e^{i\mathbf{k}\cdot\phi}$.

3.4 Results and Discussion

We ran numerical calculations on 3, 4, and 5 degree of freedom systems. Five degrees of freedom was the maximum that memory and time constraints permitted. Six degrees of freedom would have required so many trajectories to get reasonably converged calculations (using 8 angles per degree of freedom), that the run time would have taken several months.

3.4.1 Three Degrees of Freedom

Figure 3.4 shows a plot of $\langle I_3(t)\rangle_{classical}$ versus $\langle I_3(t)\rangle_{quantum}$ for Coupling Scheme I. Classical action flow from the first mode into the third mode can only occur via Arnol'd Diffusion. Clearly, the quantum flow dominates the classical energy flow, so that by definition, dynamical tunneling is much faster than Arnol'd Diffusion in this example.

Figure 3.5 shows a plot of $\langle I_3(t)\rangle_{classical}$ versus $\langle I_3(t)\rangle_{quantum}$ for Coupling Scheme III. Coupling Schemes I and II are identical for three degrees of freedom. In this case, the quantum flow is still faster, but the classical flow is comparable. This result appears to be atypical, since as higher dimensional results will show, increasing the number of degrees of freedom seems

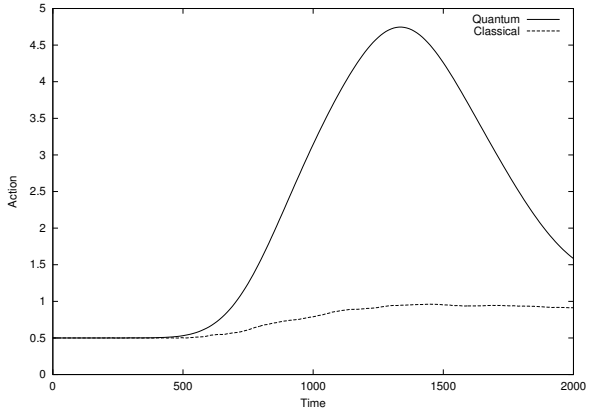

Figure 3.4: Plot of $\langle I_3(t)\rangle_{classical}$ versus $\langle I_3(t)\rangle_{quantum}$ for $D = 3$ for Coupling Scheme I.

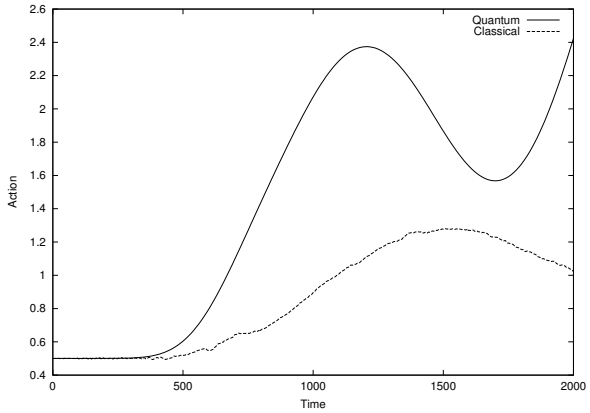

Figure 3.5: Plot of $\langle I_3(t)\rangle_{classical}$ versus $\langle I_3(t)\rangle_{quantum}$ for $D = 3$ for Coupling Scheme III.

to enhance the dynamical tunneling rate relative to the Arnol'd Diffusion rate.

3.4.2 Four Degrees of Freedom

Figure 3.6 shows a plot of $\langle I_3(t)\rangle_{classical}$ versus $\langle I_3(t)\rangle_{quantum}$ for Coupling Scheme I. Once again, dynamical tunneling is dominant. The discrepancy between dynamical tunneling and Arnol'd Diffusion rates becomes even more apparent in Figure 3.7, which shows a plot of $\langle I_4(t)\rangle_{classical}$ versus $\langle I_4(t)\rangle_{quantum}$ for the Coupling Scheme I. In this case, there is hardly any classical energy flow at all.

Figures 3.8, 3.9 show plots of $\langle I_3(t)\rangle_{classical}$ versus $\langle I_3(t)\rangle_{quantum}$ for Coupling Schemes II and III, respectively. Because mode 4 can be accessed from mode 1 via ordinary resonant energy transfer with these coupling schemes, we do not look at $\langle I_4(t)\rangle$, since the quantum and classical results are similar, and do not give any information as to the relative rates of dynamical tunneling versus Arnol'd Diffusion. Note that in comparison to the first coupling scheme, the Arnol'd Diffusion rate has been significantly reduced, so that dynamical tunneling is even more important for these coupling schemes

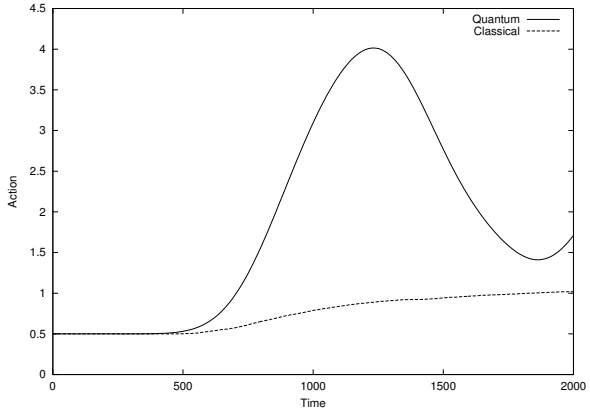

Figure 3.6: Plot of $\langle I_3(t)\rangle_{classical}$ versus $\langle I_3(t)\rangle_{quantum}$ for $D = 4$ for Coupling Scheme I.

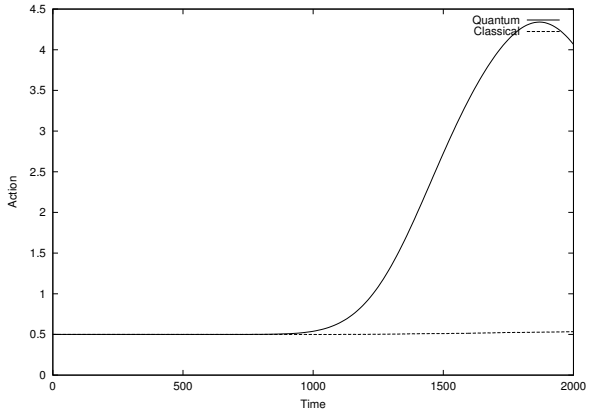

Figure 3.7: Plot of $\langle I_4(t)\rangle_{classical}$ versus $\langle I_4(t)\rangle_{quantum}$ for $D = 4$ for Coupling Scheme I.

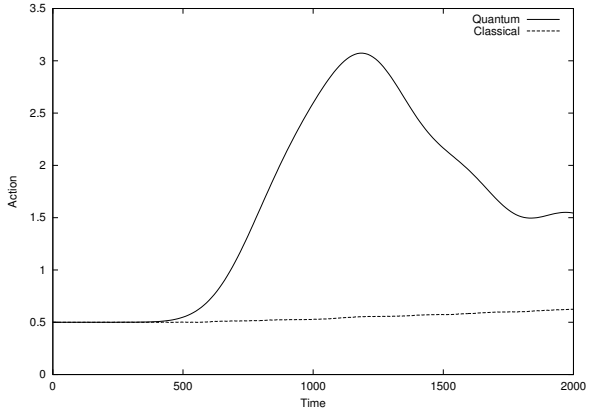

Figure 3.8: Plot of $\langle I_3(t)\rangle_{classical}$ versus $\langle I_3(t)\rangle_{quantum}$ for $D = 4$ for Coupling Scheme II.

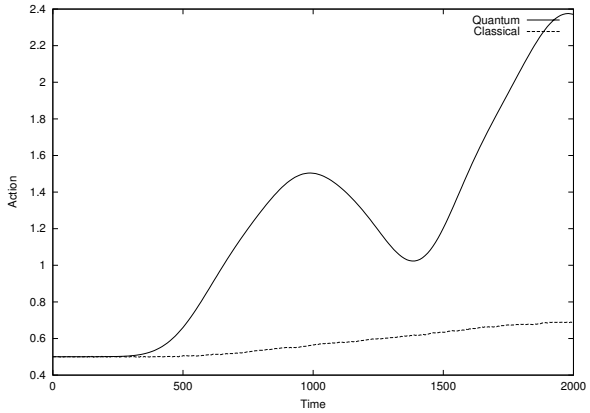

Figure 3.9: Plot of $\langle I_3(t)\rangle_{classical}$ versus $\langle I_3(t)\rangle_{quantum}$ for $D = 4$ for Coupling Scheme III.

than for Coupling Scheme I. This is in contrast to three degrees of freedom, for which the Coupling Scheme III gave Arnol'd Diffusion rates that were comparable to the dynamical tunneling rates.

3.4.3 Five Degrees of Freedom

Figures 3.10-12 show plots of $\langle I_{3,4,5}(t)\rangle_{classical}$ versus $\langle I_{3,4,5}(t)\rangle_{quantum}$ for Coupling Scheme I, respectively. Again, for this coupling scheme, the only way action can flow into modes 3, 4, and 5 from mode 1 is via Arnol'd Diffusion. Dynamical tunneling is dominant once again, though somewhat less so for mode 3. Once again, as is evidenced in Figures 3.13,14, increasing the density of the web with Coupling Schemes II and III greatly suppresses the classical action flow relative to the quantum action flow.

3.5 Mechanism of Quantum Energy Flow

Figure 3.15 shows a plot of the quantum action flow for Coupling Scheme I. The results are for a three degree of freedom system. Note that while it is dynamical tunneling that leads to energy flow from mode 1 into mode 3, nevertheless it can seen that the quantum action flow follows a pattern

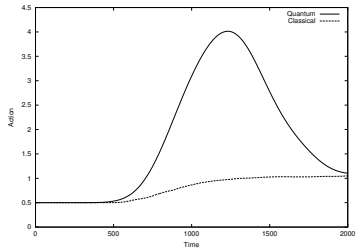

Figure 3.10: Plot of $\langle I_3(t)\rangle_{classical}$ versus $\langle I_3(t)\rangle_{quantum}$ for $D = 5$ for Coupling Scheme I.

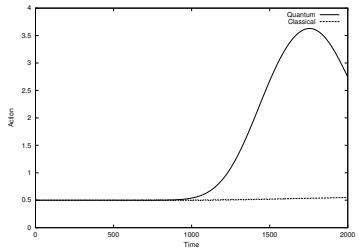

Figure 3.11: Plot of $\langle I_4(t)\rangle_{classical}$ versus $\langle I_4(t)\rangle_{quantum}$ for $D = 5$ for Coupling Scheme I.

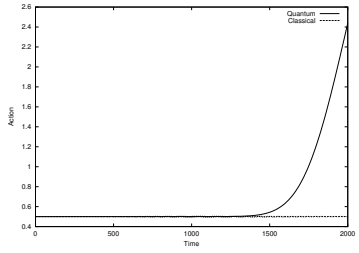

Figure 3.12: Plot of $\langle I_5(t)\rangle_{classical}$ versus $\langle I_5(t)\rangle_{quantum}$ for $D = 5$ for Coupling Scheme I.

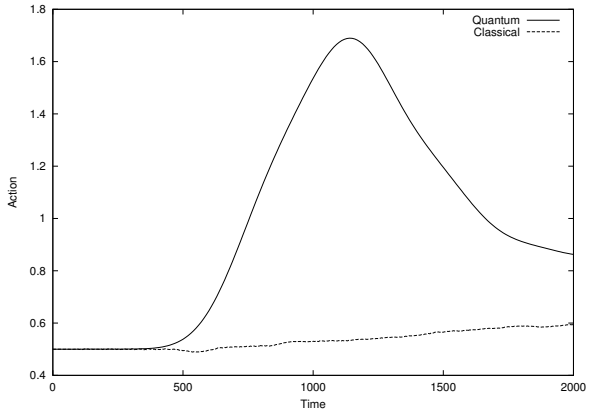

Figure 3.13: Plot of $\langle I_{3,5}(t)\rangle_{classical}$ versus $\langle I_{3,5}(t)\rangle_{quantum}$ for $D = 5$ for Coupling Scheme II.

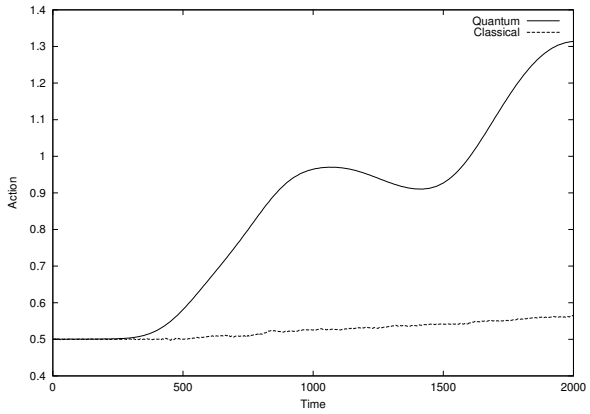

Figure 3.14: Plot of $\langle I_{3,5}(t)\rangle_{classical}$ versus $\langle I_{3,5}(t)\rangle_{quantum}$ for $D = 5$ for Coupling Scheme III.

that is formally the same as the classical action flow. Thus, action first flows from mode 1 into mode 2, and then from mode 2 to mode 3. The reason for this is that moving along a classical resonance corresponds to moving along a degenerate manifold of states quantum-mechanically. This suggests that the classical resonance structure of the Hamiltonian gives rise to a "quantum Arnol'd Diffusion" along the degenerate manifold of states defined by the resonance web. The action flow is due to dynamical tunneling, but nevertheless is the quantum analogue of Arnol'd Diffusion.

3.6 Localization of the Eigenstates

In this section we briefly discuss the issue of eigenstate localization for our Hamiltonian. We begin by introducing a quantity, known as the Inverse Participation Ratio (IPR), that provides a measure for the extent to which an eigenstate is delocalized. The IPR $P(a|a)$ of an initial state $|a\rangle$ is given by,

$$P(a|a) = \lim_{T\to\infty} \frac{1}{T} \int_0^T |\langle a|e^{-i\hat{H}t/\hbar}|a\rangle|^2 dt \tag{3.11}$$

Thus, the IPR measures the time averaged probability of a wavepacket returning to its initial state. The more ergodic the system, the longer the

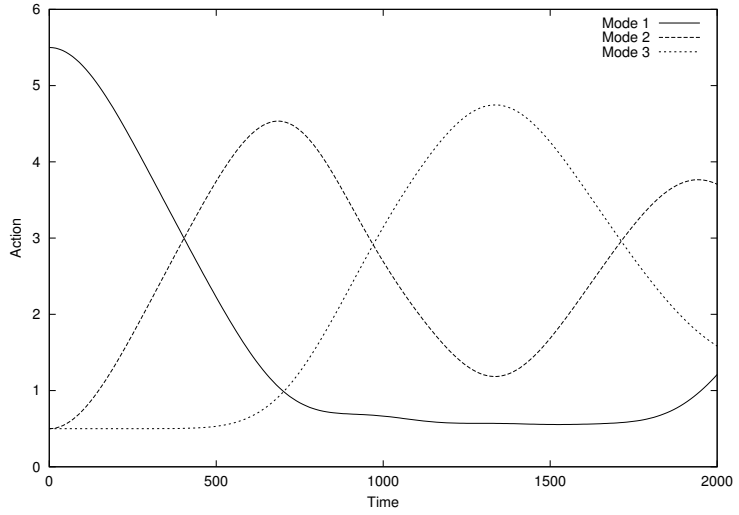

Figure 3.15: Quantum action flow illustrating the quantum analogue of Arnol'd Diffusion.

wavepacket spends away from the initial state, and thus the smaller the IPR. Random Matrix Theory (RMT) predicts an IPR of $\frac{3}{N+2}$, where N denotes the number of available states within an energy interval defined by the Fermi Golden Rule decay width. If the wavepacket samples the surrounding phase-space completely uniformly, then the IPR is $\frac{1}{N}$. Thus, in the large N limit, RMT predicts that about 1/3 of the available phase-space is sampled by the initial state.

An equivalent definition of the IPR is given by,

$$P(a|a) = \sum_n p(n|a)^2 \tag{3.12}$$

where $p(n|a)$ denotes the probability that the zeroth-order state $|a\rangle$ is in eigenstate $|n\rangle$. The more delocalized the eigenstates, then the more a given zeroth-order state is shared amongst the eigenstates. Thus, the IPR provides a convenient measure for the extent of eigenstate delocalization.

For Coupling Scheme I, increasing λ causes the IPR to exhibit a localization to delocalization transition around $\lambda = 1$. Figure 3.16 shows a plot of the number of available states N for an 8 degree of freedom run with a total of 5 quanta. The number of available states remains fairly constant at around 70, and then from around $\lambda = 0.1 - 1.0$ it undergoes a fairly sharp increase

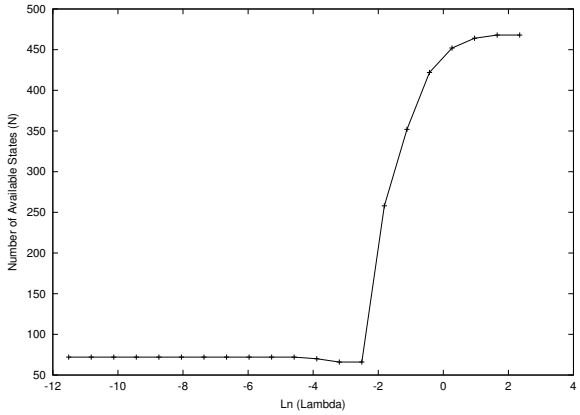

Figure 3.16: Total number of available states N for $D = 8$, 5 quanta, as a function of $\ln \lambda$ (Coupling Scheme I).

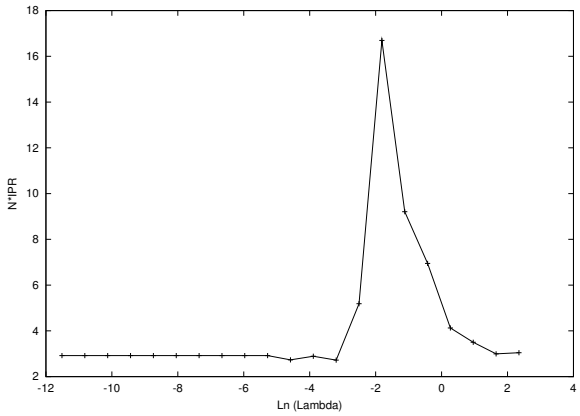

Figure 3.17: Plot of (Number of Available States) $\times$ Inverse Participation Ratio for $D = 8$, 5 quanta, as a function of $\ln \lambda$ (Coupling Scheme I).

to approximately 470. A plot of $N \times IPR$ given in Figure 3.17 parallels this transition. $N \times IPR$ remains essentially constant at right around the RMT prediction of 3. The eigenstates are delocalized along the degenerate chain of states lying along the Arnol'd Web for this coupling scheme. Around $\lambda = 0.1$, the number of available states increases dramatically, but the IPR remains essentially unchanged, indicating that the eigenstates are becoming localized. However, as λ is increased beyond 1, the value of $N \times IPR$ undergoes a localization to delocalization transition. The eigenstates spread to ergodically sample the larger set of states available, and consequently $N \times IPR$ drops to a value slightly larger than predicted by RMT.

Figures 3.18-20 show plots of the local density of states (LDOS) for $\lambda = 0.01, 0.1, 1.0$, corresponding to the three regimes described above. For $\lambda = 0.01$ the structure is not random, which reflects the structure of the Arnol'd Web for our coupling scheme. For $\lambda = 0.1$ we see that the LDOS is sparser, indicating the onset of localization. Finally, for $\lambda = 1.0$ the system is classically chaotic, and this is reflected in the corresponding LDOS.

For Coupling Schemes II and III, the eigenstates have a tendency to localize, independent of λ. Nevertheless, the number of occupied states in the quasi-integrable regime is essentially independent of λ. Only for $\lambda = 0$ is

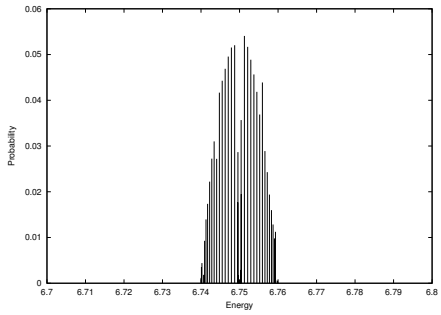

Figure 3.18: LDOS for $D = 8$, 5 quanta, for $\lambda = 0.01$ (Coupling Scheme I).

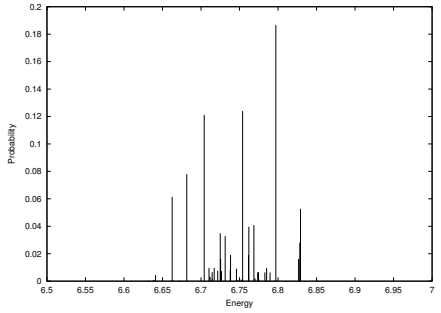

Figure 3.19: LDOS for $D = 8$, 5 quanta, for $\lambda = 0.1$ (Coupling Scheme I).

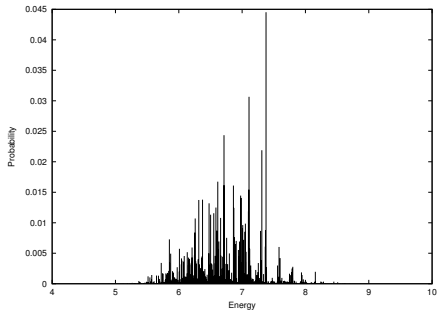

Figure 3.20: LDOS for $D = 8$, 5 quanta, for $\lambda = 1.0$ (Coupling Scheme I).

the IPR exactly 1. Increasing λ by an arbitrarily small ϵ causes the IPR to drop dramatically, indicating some initial delocalization over the manifold of degenerate zeroth-order states.

3.7 Conclusions and Future Research

This chapter studied Arnol'd Diffusion rates and compared them to dynamical tunneling rates using a relatively simple, yet physically motivated, Hamiltonian with a readily constructible Arnol'd Web. In general it was determined that dynamical tunneling is significantly faster than Arnol'd Diffusion. The only major exception to this was a three degree of freedom run using the third coupling scheme. Even for this run, however, the dynamical tunneling was still dominant. In any case, the results suggest that with higher degrees of freedom and an increasingly dense Arnol'd Web, the Arnol'd Diffusion was suppressed with respect to the dynamical tunneling.

The results in this chapter support the claim that it is dynamical tunneling, and not Arnol'd Diffusion, which is the prime culprit for the fine low-energy peak splittings observed in IR spectra of medium-sized polyatomic molecules. While our model does not sample the entire parameter space for

determining whether or not dynamical tunneling is faster than Arnol'd Diffusion, this is impossible to do in any event. In addition, future research will need to determine the roles that classical chaos and mode mixing play in vibrational energy flow at low quantum numbers. As discussed in the Introduction, these mechanisms are believed to be unimportant, but it would be useful to directly test this assumption with numberical and even experimental studies.

We also determined that the quantum action flows according to the underlying resonance structure of the Hamiltonian, giving rise to a mechanism which we call quantum Arnol'd Diffusion. The quantum action flow along the degenerate manifold of states is due to dynamical tunneling, but the dynamics is such that it corresponds to an Arnol'd Diffusion-like energy transfer.

Finally, we addressed the issue of localization in our model, and showed that while Coupling Schemes II and III produce localized eigenstates, Coupling Scheme I exhibits a localization to delocalization transition.

Chapter 4

An Analytically Solvable Stochastic Model for Energy Dispersion Due to Numerous Landau-Zener Transitions

This chapter presents a simple stochastic model for energy dispersion due to numerous Landau-Zener transitions. We consider a Hamiltonian with a dependence on a single parameter λ, whose energy levels form a web of

trajectories as λ is varied. We assume that there are residual perturbative terms in the Hamiltonian which cause intersections of energy level curves to become narrow avoided crossings. The energy gap between successive avoided crossings is assumed constant, and furthermore the hopping probability is assumed to be a constant $p \in [0, 1]$. Assuming stochastic dynamics, we then obtain an analytically solvable model for the dispersion profile. The profile is found to be gaussian, with an energy drift proportional to $\frac{p-\frac{1}{2}}{1-p}$. In particular, the energy drift is found to be independent of the number of avoided crossings. The standard deviation of the gaussian yields a diffusion coefficient proportional to $\frac{p}{1-p}$, in contrast to the biased random-walk result of $p(1-p)$. This means that as $p \to 1$, the Landau-Zener dispersion becomes infinite, while the biased-random walk dispersion becomes zero.

4.1 Introduction

The energy levels of parameter-dependent Hamiltonians are often characterized by the presence of avoided crossings. An avoided crossing occurs when two energy levels become degenerate as a function of the parameter being varied. Instead of being exactly degenerate, residual quantum-mechanical

couplings lead to a breaking of the degeneracy. If the parameter is varied slowly enough, then the adiabatic theorem guarantees that a state prepared in an eigenstate of the initial Hamiltonian will move along the energy contour corresponding to the eigenstate of the varying Hamiltonian. Near avoided crossings, however, the parameter must be varied even more slowly for the adiabatic theorem to hold. If the parameter is varied somewhat faster, then energy transfer can occur between the adjacent states of the avoided crossing. This type of diabatic energy transfer is known as a Landau-Zener transition.

In chemistry, Landau-Zener transitions are often responsible for the breakdown of the Born-Oppenheimer approximation used to analyze nuclear motion. This phenomenon is termed surface hopping in the chemical literature, and allows for transitions between one Born-Oppenheimer electronic potential energy surface to another. Surface hopping can play a crucial role in chemical reaction dynamics. For example, dissociation can occur when a Landau-Zener transition is made from a bound state on one potential energy surface to an unbound state of the same energy on another potential energy surface.

The purpose of this chapter is to analyze the energy spreading when a Hamiltonian is carried through numerous avoided crossings. In particular,

we consider a model consisting of an arbitarily large network of energy levels, with a regular pattern of avoided crossings. It is assumed that the probability for a Landau-Zener jump is p. We assume stochastic dynamics, and develop a recursive formula for computing the dispersion profile as a function of the number of avoided crossings. We then go on to obtain an analytical form to characterize this dispersion profile.

In fairness, it should be pointed out that a similar model and solution was obtained in 1994 by Harmin and Price (Ref. 38). Nevertheless, our result was derived independently and using slightly different techniques, so we felt that it is still interesting and appropriate for this thesis.

4.2 The Model

We have a set of adiabatic energy level curves. We assume that the probability for a Landau-Zener diabatic jump at an avoided crossing is p. We may then ask the following: Assuming a system is taken past N avoided crossings, what is the probability of making k upward moves? An upward (downward) move is one in which the change in energy from one avoided crossing to the next is positive (negative). Figure 4.1 illustrates the energy

level pattern we are considering. A charged particle on a ring with a uniform magnetic field oriented perpendicular to the ring generates a qualitatively similar energy level pattern when the magnetic field strength becomes the variable parameter.

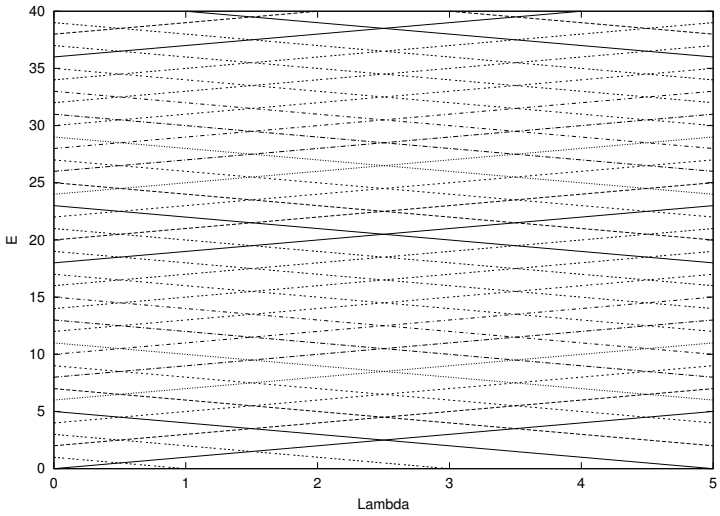

Figure 4.1: Diagram showing network of avoided crossings generated by varying some parameter λ.

We now turn to the solution of our model (Figure 4.2 may be a useful visual tool for following the argument): We begin at an avoided crossing and traverse N in succession. We define $P_{\pm}(k, N)$ to be the probability of having k upward movements if we initially start on the higher/lower adiabat at the

avoided crossing. Note that we are assuming stochastic dynamics, that is, we neglect the effect of phase interference on the dispersion profile.

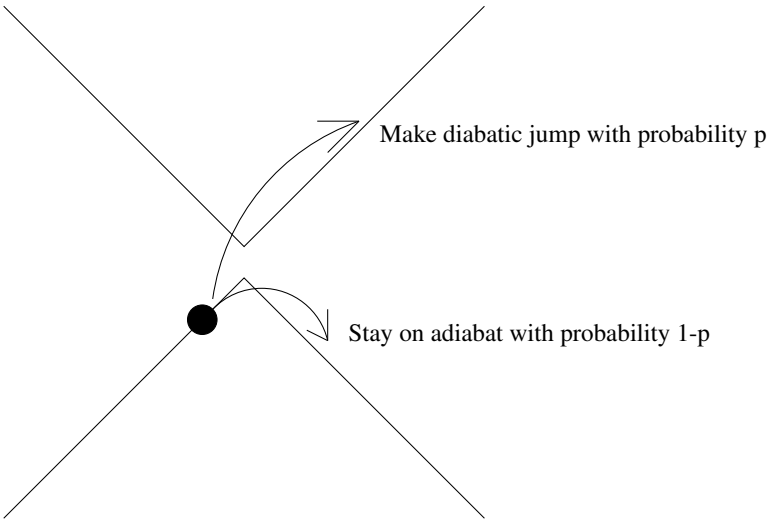

Figure 4.2: Diagram showing possible behaviors at an avoided crossing.

So, suppose we start on the higher adiabat. We can either stay on the adiabat with probability $1 - p$, or we can hop to the lower adiabat with probability p. If we stay on the adiabat, then our energy increases as we head to the next avoided crossing, so that now we only have to make $k - 1$ more upward moves. Our system is thus on the lower adiabat at the next avoided crossing, and here we have to make $k - 1$ upward moves in $N - 1$ steps, with a total probability of $P_{-}(k - 1, N - 1)$. Since the probability of

initially staying at the first avoided crossing was $1-p$, we have a contribution of $(1-p)P_{-}(k-1,N-1)$ to $P_{+}(k,N)$.

So now suppose that, starting at the higher adiabat, we jump to the lower adiabat with probability p. Then our energy decreases as we head to the next avoided crossing, and so we remain on a higher-energy adiabat. Since we still have to make k upward moves, the contribution to $P_{+}(k,N)$ from this possibility is $pP_{+}(k,N-1)$, and so we obtain that,

$$P_{+}(k,N) = pP_{+}(k,N-1) + (1-p)P_{-}(k-1,N-1) \tag{4.1}$$

We now complete the picture by assuming we start at the lower adiabat. We can jump with probability p, so that our energy increases to the next avoided crossing, and so we remain on a lower energy adiabat. Thus the contribution to $P_{-}(k,N)$ from this possibility is $pP_{-}(k-1,N-1)$. Alternatively, with probability $1-p$ we stay on the lower energy adiabat, so that our energy decreases as we head to the next avoided crossing. We are thus on the higher energy adiabat at the next avoided crossing, and we still have to make k upward moves, so the probability from this possibility is $(1-p)P_{+}(k,N-1)$, giving us,

$$P_{-}(k,N) = (1-p)P_{+}(k,N-1) + pP_{-}(k-1,N-1) \tag{4.2}$$

It is easy to establish the following identities: $P_+(0,N) = P_-(N,N) = p^N$, and $P_+(N,N) = P_-(0,N) = (1-p)p^{N-1}$. From this and from our recursion formulas for $P_\pm$ we aim to show that $P_-(k,N) = P_+(N-k,N)$, $0 \leq k \leq N$. For $N = 1$ this is obviously true. So suppose it is true for N. Then for $N+1$ it is certainly true for $k = 0, N+1$. Assume then that $1 \leq k \leq N$. Then we have,

$$\begin{aligned} P_-(k,N+1) &= (1-p)P_+(k,N) + pP_-(k-1,N) \\ &= (1-p)P_-(N-k,N) + pP_+(N+1-k,N) \\ &= pP_+(N+1-k,N) + (1-p)P_-(N+1-k-1,N) \\ &= P_+(N+1-k,N+1) \end{aligned} \tag{4.3}$$

and so our claim is proved. Therefore, we can write,

$$P_+(k,N) = pP_+(k,N-1) + (1-p)P_+(N-k,N-1) \tag{4.4}$$

Combined with $P_+(0,N) = p^N$, $P_+(N,N) = (1-p)p^{N-1}$, and $P_-(k,N) = P_+(N-k,N)$, we can evaluate $P_\pm(k,N)$ for all k, N.

4.3 Moments of the Distribution

We shall now obtain a recursive relation for finding the moments of our distribution $P_+(k,N)$ (since P_- can be obtained from P_+ by the transformation $k \to N-k$, we need only consider one of the P-functions). The m^{th} moment, $m > 0$, is defined via,

$$\langle k^m \rangle_N = \sum_{k=0}^{N} k^m P_+(k,N) \tag{4.5}$$

Our recursive relation is obtained via,

$$\begin{aligned}
\langle k^m \rangle_N &= \sum_{k=1}^{N-1} k^m P_+(k,N) + N^m (1-p) p^{N-1} \\
&= N^m (1-p) p^{N-1} + \sum_{k=1}^{N-1} \left(k^m p P_+(k,N-1) + k^m (1-p) P_+(N-k,N-1) \right) \\
&= N^m (1-p) p^{N-1} + p \langle k^m \rangle_{N-1} + (1-p) \times \\
&\quad \sum_{k=1}^{N-1} (k-N+N)^m P_+(N-k,N-1) \\
&= N^m (1-p) p^{N-1} + p \langle k^m \rangle_{N-1} \\
&\quad + (1-p) \sum_{k=1}^{N-1} P_+(N-k,N-1) \sum_{l=0}^{m} \binom{m}{l} (-1)^l (N-k)^l N^{m-l} \\
&= N^m (1-p) p^{N-1} + p \langle k^m \rangle_{N-1} + (1-p) \Big(\sum_{l=1}^{m} \binom{m}{l} (-1)^l N^{m-l} \langle k^l \rangle_{N-1} \\
&\quad + \sum_{k=1}^{N-1} N^m P_+(N-k,N-1) \Big) \\
&= N^m (1-p) p^{N-1} + p \langle k^m \rangle_{N-1} + (1-p) \Big(\sum_{l=1}^{m} \binom{m}{l} (-1)^l N^{m-l} \langle k^l \rangle_{N-1}
\end{aligned}$$

$$
\begin{aligned}
& +N^m(1-p^{N-1})) \\
= \; & p\langle k^m\rangle_{N-1} + (1-p)(-1)^m\langle k^m\rangle_{N-1} + (1-p)\sum_{l=1}^{m-1}\binom{m}{l}(-1)^l N^{m-l}\langle k^l\rangle_{N-1} \\
& +N^m(1-p) \\
= \; & (p+(-1)^m(1-p))\langle k^m\rangle_{N-1} + (1-p)\sum_{l=1}^{N-1}\binom{m}{l}(-1)^l N^{m-l}\langle k^l\rangle_{N-1} \\
& +N^m(1-p) \qquad (4.6)
\end{aligned}
$$

and so, we see that,

$$
\langle k^m\rangle_N = (p+(-1)^m(1-p))\langle k^m\rangle_{N-1} + (1-p)\sum_{l=1}^{m-1}\binom{m}{l}(-1)^l N^{m-l}\langle k^l\rangle_{N-1} + N^m(1-p) \qquad (4.7)
$$

4.4 Dispersion Profile

Our goal will to determine the distribution profile for the net displacement $n \equiv 2k - N$, having started on the lower adiabat. By the Central Limit Theorem, the distribution of n becomes gaussian in the limit of large N. To completely characterize this gaussian, we have to compute the mean $\langle n\rangle$, and standard deviation σ. This will first require us to compute $\langle k\rangle_N$ and $\langle k^2\rangle_N$.

So we begin by setting $m = 1$ in the relation obtained in the previous

section. This gives,

$$\langle k\rangle_N = (2p-1)\langle k\rangle_{N-1} + N(1-p) \tag{4.8}$$

For large N we shall make the assumption that $\langle k\rangle_N$ is an analytical function of p, so that we can expand it in a Taylor series about $p = \frac{1}{2}$. Plugging into our recursive formula, we immediately obtain that at $p = \frac{1}{2}$, $\langle k\rangle_N = \frac{N}{2}$. Differentiating with respect to p gives $\frac{d\langle k\rangle_N}{dp} = 2\langle k\rangle_{N-1} + (2p-1)\frac{d\langle k\rangle_{N-1}}{dp} - N$. Substituting $p = \frac{1}{2}$ gives $\langle k\rangle'_N(\frac{1}{2}) = 2\frac{N-1}{2} - N = -1$.

Continuing this process, we get $\frac{d^2\langle k\rangle_N}{dp^2} = 4\frac{d\langle k\rangle_{N-1}}{dp} + (2p-1)\frac{d^2\langle k\rangle_{N-1}}{dp^2}$. By repeatedly differentiating, we obtain for $N \geq 2$ that,

$$\frac{d^n\langle k\rangle_N}{dp^n} = 2n\frac{d^{n-1}\langle k\rangle_{N-1}}{dp^{n-1}} + (2p-1)\frac{d^n\langle k\rangle_{N-1}}{dp^n} \tag{4.9}$$

Therefore, $\langle k\rangle_N^{(n)}(\frac{1}{2}) = 2n\langle k\rangle_{N-1}^{(n-1)}(\frac{1}{2})$. Now, from $\langle k\rangle_N^{(1)}(\frac{1}{2}) = -1$ we have,

$$\langle k\rangle_N^{(n)}(\frac{1}{2}) = -2^{n-1}n!, n \geq 2 \tag{4.10}$$

Note that this formula also works for $n = 1$. Therefore, in the large N limit we obtain that,

$$\begin{aligned}\langle k\rangle_N(p) &= \frac{N}{2} - \sum_{n=1}^{\infty} 2^{n-1}(p-\frac{1}{2})^n \\ &= \frac{N}{2} - \frac{1}{2}\sum_{n=1}^{\infty}(2p-1)^n\end{aligned}$$

$$= \frac{N}{2} - \frac{1}{2}\frac{2p-1}{2-2p}$$
$$= \frac{1}{2}(N - \frac{p-\frac{1}{2}}{1-p}) \tag{4.11}$$

This is the mean value of upward moves having started on the higher adiabat. Thus, the mean value of downward moves is $\langle N-k\rangle = N - \langle k\rangle = \frac{1}{2}(N + \frac{p-\frac{1}{2}}{1-p})$. This is exactly the mean value of upward moves having started on the lower adiabat. Therefore, $\langle n\rangle = \langle 2k-N\rangle = 2\langle k\rangle - N = N + \frac{p-\frac{1}{2}}{1-p} - N = \frac{p-\frac{1}{2}}{1-p}$, and so we can write, in the limit of large N, that,

$$\langle n\rangle = \frac{p-\frac{1}{2}}{1-p} \tag{4.12}$$

Setting $m = 2$ in our recursion relation gives,

$$\langle k^2\rangle_N = (p+1-p)\langle k^2\rangle_{N-1} + (1-p)(-1)(2)N\langle k\rangle_{N-1} + N^2(1-p)$$
$$= \langle k^2\rangle_{N-1} - 2N(1-p)\langle k\rangle_{N-1} + N^2(1-p) \tag{4.13}$$

Once again, for N large we shall assume that $\langle k^2\rangle_N$ is an analytic function of p. At $p = \frac{1}{2}$ we have $\langle k^2\rangle_N = \langle k^2\rangle_{N-1} - N\langle k\rangle_{N-1} + \frac{1}{2}N^2 = \langle k^2\rangle_{N-1} - \frac{N(N-1)}{2} + \frac{1}{2}N^2 = \frac{N}{2} + \langle k^2\rangle_{N-1}$. Therefore, $\langle k^2\rangle_N = \frac{1}{2}(N + N - 1 + \cdots + 1) = \frac{N(N+1)}{4}$.

Differentiating with respect to p gives,

$$\frac{d\langle k^2\rangle_N}{dp} = \frac{d\langle k^2\rangle_{N-1}}{dp} + 2N\langle k\rangle_{N-1} - 2N(1-p)\frac{d\langle k\rangle_{N-1}}{dp} - N^2 \tag{4.14}$$

We then obtain $\langle k^2\rangle'_N(\frac{1}{2}) = \langle k^2\rangle'_{N-1}(\frac{1}{2}) + 2N\frac{N-1}{2} - 2N\frac{1}{2}(-1) - N^2 = \langle k^2\rangle'_{N-1}(\frac{1}{2}) + N^2 - N + N - N^2 = \langle k^2\rangle'_{N-1}(\frac{1}{2})$. Therefore, $\langle k^2\rangle'_N(\frac{1}{2}) = \langle k^2\rangle'_1(\frac{1}{2})$. Now, $\langle k^2\rangle_1(p) = 1 - p$, and so $\langle k^2\rangle'_1(\frac{1}{2}) = -1$.

Differentiating again gives, $\frac{d^2\langle k^2\rangle_N}{dp^2} = \frac{d^2\langle k^2\rangle_{N-1}}{dp^2} + 4N\frac{d\langle k\rangle_{N-1}}{dp} - 2N(1-p)\frac{d^2\langle k\rangle_{N-1}}{dp^2}$. Continuing in this way, we see that for $n \geq 2$,

$$\frac{d^n\langle k^2\rangle_N}{dp^n} = \frac{d^n\langle k^2\rangle_{N-1}}{dp^n} + 2nN\frac{d^{n-1}\langle k\rangle_{N-1}}{dp^{n-1}} - 2N(1-p)\frac{d^n\langle k\rangle_{N-1}}{dp^n} \qquad (4.15)$$

Therefore at $p = \frac{1}{2}$ we get,

$$\begin{aligned}
\langle k^2\rangle_N^{(n)}(\frac{1}{2}) &= \langle k^2\rangle_{N-1}^{(n)}(\frac{1}{2}) + 2nN(-2^{n-2}(n-1)!) - N(-2^{n-1}n!) \\
&= \langle k^2\rangle_{N-1}^{(n)}(\frac{1}{2}) - 2^{n-1}n!N + 2^{n-1}n!N \\
&= \langle k^2\rangle_{N-1}^{(n)}(\frac{1}{2}) \qquad (4.16)
\end{aligned}$$

Now, from $\langle k^2\rangle_1(p) = 1 - p$ we have that $\langle k^2\rangle_1^{(n)}(p) = 0$ for $n \geq 2$, and so $\langle k^2\rangle_N^{(n)}(\frac{1}{2}) = 0$ for $n \geq 2$. Thus the Taylor expansion for $\langle k^2\rangle_N$ is,

$$\langle k^2\rangle_N(p) = \frac{N(N+1)}{4} - (p - \frac{1}{2}) \qquad (4.17)$$

This is $\langle k^2\rangle_N$ for upward moves starting on the higher adiabat. For the downward moves starting at the higher adiabat, we look at

$$\langle (N-k)^2\rangle = N^2 - 2N\langle k\rangle + \langle k^2\rangle$$

$$
\begin{aligned}
&= N^2 - 2N\frac{1}{2}(N - \frac{p-\frac{1}{2}}{1-p}) + \frac{N^2}{4} + \frac{N}{4} - (p - \frac{1}{2}) \\
&= N^2 - N^2 + N\frac{p-\frac{1}{2}}{1-p} + \frac{N^2}{4} + \frac{N}{4} - (p - \frac{1}{2}) \\
&= \frac{N}{4}(\frac{4p-2}{1-p} + 1) + \frac{N^2}{4} - (p - \frac{1}{2}) \\
&= \frac{N}{4}\frac{3p-1}{1-p} + \frac{N^2}{4} - (p - \frac{1}{2}) \qquad (4.18)
\end{aligned}
$$

This is $\langle k^2 \rangle_N$ for upward moves starting on the lower adiabat. Therefore,

$$
\begin{aligned}
\langle n^2 \rangle = \langle (2k - N)^2 \rangle &= 4\langle k^2 \rangle - 4N\langle k \rangle + N^2 \\
&= N\frac{3p-1}{1-p} + N^2 - (4p-2) - 2N(N + \frac{p-\frac{1}{2}}{1-p}) + N^2 \\
&= N\frac{3p-1}{1-p} + N^2 - (4p-2) - 2N^2 - 2N\frac{p-\frac{1}{2}}{1-p} + N^2 \\
&= N\frac{3p-1-2p+1}{1-p} - (4p-2) \\
&= N\frac{p}{1-p} - (4p-2) \qquad (4.19)
\end{aligned}
$$

and so, for our Gaussian profile, we get that $\sigma^2 = N\frac{p}{1-p} - (4p-2) - (\frac{p-\frac{1}{2}}{1-p})^2$. For large N, this becomes,

$$\sigma = \sqrt{N\frac{p}{1-p}} \qquad (4.20)$$

The equation for our Gaussian is therefore,

$$P_N(n) = \frac{2}{\sigma\sqrt{2\pi}} \exp(-\frac{(n - \langle n \rangle)^2}{2\sigma^2}) \qquad (4.21)$$

The factor of 2 is included since we are working with a probability here, not a probability density, and as k runs from 0 to N, n runs from $-N$ to N in steps of 2.

4.5 Numerical Test and Discussion

To demonstrate our formula, we ran a numerical test with $N = 500$ and $p = 0.95$. The results are plotted in Figure 4.3. Note that our gaussian fit matches the exact result perfectly. It turns out that that the gaussian fit is pretty good even when we start to see a diabatic spike at $n = N$. For a small spike the gaussian hugs the broad part of the distribution reasonably well. For a large spike, deviations are more significant, but so much of the probability is already clustered at N that the discrepancy between the gaussian fit and the broad part of the profile is not that noticeable. In any event, for finite N the gaussian fit is expected to break down for p sufficiently close to 1. The presence of a diabatic spike renders our analyticity assumption incorrect, and it is this assumption that was used to derive the parameters for our gaussian profile. However, for a fixed p, by making N sufficiently large, we can get rid of the diabatic spike and recover the gaussian profile.

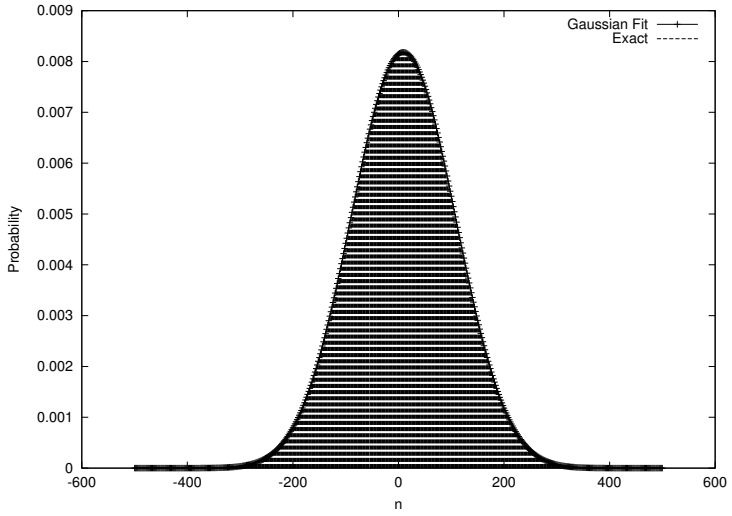

Figure 4.3: Comparison of analytical versus numerical dispersion profiles due to stochastic motion on the network of avoided crossings.

It should also be noted that our stochastic model is not the same as a simple random walk model. The reason for this is that in the case of a random walk, the probability for an upward jump is always a fixed $p \in [0, 1]$. In the case of Landau-Zener dynamics, the hopping probability p corresponds to an upward jump only if we start on the lower adiabat. If we happen to stay on the lower adiabat, then at the next avoided crossing we are on the higher adiabat, and so the hopping probability p corresponds to a downward jump.

To make everything concrete, for the random-walk with a probability for

an upward hop of p, we have,

$$\langle n \rangle = (2p - 1)N \tag{4.22}$$

and,

$$\sigma = 2\sqrt{p(1-p)N} \tag{4.23}$$

Note that compared to the random-walk model, the net Landau-Zener energy drift is relatively insensitive to the hopping probability. In fact, it is independent of N, while the random-walk energy drift scales linearly with N. This is because once a trajectory stays on an adiabat instead of hopping, the bias for moving in a given direction switches to the opposite direction. This same switching effect also accounts for the enhanced energy dispersion in the Landau-Zener model as opposed to the random-walk model. In the random-walk case, $\sigma \to 0$ as $p \to 1$, while in the Landau-Zener case, $\sigma \to \infty$.

4.6 Conclusions

Our Landau-Zener transitions model is probably the simplest one could construct for the type of energy spreading we are considering. In general, the hopping probability is not constant, and quantum interference effects can

change the dispersion profile from what would be expected if the dynamics was truly stochastic. However, if the system is immersed in a bath, then decoherence can destroy any quantum interference effects, leading back to essentially stochastic dynamics. Furthermore, while a constant hopping probability is not generic, we believe that the spreading which our analytical model predicts is generic. That is, as the probability for a diabatic jump approaches 1, the net energy drift and spreading increases as well.

Chapter 5

A Perturbative Approach to Vibrational Predissociation Rates: Application to ArHF

This chapter presents a perturbative model for the vibrational predissociation dynamics of inert gas hydrogen halide (RgHX) complexes. The predissociation is modelled as a Fermi Golden Rule (FGR) process from a bound-state residing on a two-parameter potential energy surface (PES) obtained by averaging over the HX vibrational state of interest, to a series of one-parameter

exit channels obtained by averaging over the HX rovibrational state of interest. This model is applied to ArHF, for which a high quality ab initio interaction potential is available. In particular, we focus on the $v \to v-1$ transition for the bound states (1000), (2000), (2110), (3000) and (3110). We confirm the experimental observation that the product HF tends to come off at the highest accessible j-state, which is $j = 13$ for this system. This indicates a strong angular anisotropy in the ArHF interaction potential which couples low-j and high-j HF states. The basic mechanism for this high-j preference is determined to be the suppression of the low-j exit channels arising from highly oscillatory low-j outgoing wavefunctions. We also observed that the tails of the bound-state wavefunctions, in the inner wall region of the interaction potential, gave the main contribution to the predissociation rate, indicating that the vibrational predissociation process is due to tunneling and is therefore a purely quantum effect. The calculations also confirm the strong v-dependence of the predissociation rates, as well as the stabilization of the complex that occur when energy is placed into the HF bending mode. For the (1000) and (2110) states, we obtain rates well below $1,600\ \mathrm{sec}^{-1}$, which is consistent with the observation by Miller [56, 57] that the vibrational predissociation rates are too slow to be measured. The (2000) state does give

a measurable rate, with a computed decay into the $j = 13$ exit channel of $14,000\ \mathrm{sec}^{-1}$. The (3000) state gives a corresponding rate of $200,000\ \mathrm{sec}^{-1}$, in good agreement with the overall dissociation rate of $250,000\ \mathrm{sec}^{-1}$. The (3110) rate is slower, with a value of $12,000\ \mathrm{sec}^{-1}$. While this rate seems somewhat small, given that the lifetime of the (3110) state was measured to only be twice as long as that of the (3000) state, this rate and all our rates are within an order of magnitude of the measured rates.

5.1 Introduction

The study of the vibrational predissociation of van der Waals and hydrogen-bonded complexes has been an active field of experimental and theoretical research for the past twenty five years. Vibrational predissociation, as a mechanism for converting vibrational energy into translational and rotational energy, may play an important role in relaxation dynamics in gases and liquids, so a proper understanding of it is important.

Some of the most extensively studied complexes are the inert gas hydrogen halide complexes (RgHX). These are the simplest complexes which can have both vibration to rotation and vibration to translation energy transfer. Fur-

thermore, the hydrogen halide complexes have the interesting property that they tend to predissociate with the maximum allowable rotational energy. This is due to the relatively large rotational constants of the HX diatomics, in contrast to the RgX_2 complexes, which tend to predissociate with high translational energy [43]. This pattern is a classic example of the Ewing momentum gap law [51], which basically states that energy in some initial donor state is transferred preferentially to the final acceptor state (or states) with the least nodal character. This makes sense since highly oscillatory wavefunctions tend to have little coupling with the initial state. An equivalent formulation of this principle is that energy flows into the state which minimizes the momentum transfer. The HX diatomics have relatively large rotational energy gaps, so minimizing the nodal character of the outgoing waves means placing the excess energy into rotation. The X_2 diatomics have much smaller rotational energy gaps, so minimizing the nodal character of the outgoing waves means placing the excess energy into translation.

Another feature of the RgHX complexes is that their predissociation rates are particularly slow [44, 47], making it difficult to accurately compute their rates. In an early theoretical study, Hutson [49] attempted to calculate the vibrational predissociation rates of ArHCl for $v_{HCl} = 1$ bound-states, but

his results were off by at least two orders of magnitude [58]. In another early study, Halberstadt [48] modelled the $(HF)_2$ dimer as an RgHF complex in order to calculate the predissociation rates. However, it is known that complexes with higher degrees of freedom, such as Ar_3HF, $(HF)_2$, and N_2HF, have predissociation rates which are typically several orders of magnitude faster than the RgHF complexes [47], so it is not clear that modelling $(HF)_2$ as an RgHF complex is accurate.

One of the most commonly studied RgHX complexes is ArHF. ArHF bound-states have been synthesized up to [46] $v_{HF} = 4$, while predissociation rates have been studied for [44, 46, 57] $v_{HF} = 1 - 3$. The predissociation rates show a strong dependence on v_{HF}. Furthermore, the bound-states of ArHF are significantly stabilized when energy is placed into the HF bending mode. The $v_{HF} = 1$ rates were too slow ($< 1,600\ s^{-1}$) to be observed in measurements by Miller [56]. Some of the $v_{HF} = 2$ rates were measurable [57], though the rates were still too slow for a value to be assigned. For $v_{HF} = 3$ the rates are sufficiently high to calculate a rotational distribution for the predissociation [44].

The first attempt to model the predissociation of ArHF via a completely ab initio model was done in Ref. 43 by Buchachenko, Stepanov, Grigorenko,

and Nemukhin. Buchachenko et al. model the predissociation process using a semi-empirical ArHF PES obtained using the diatomics-in-molecule approach. While their approach confirmed the propensity of the HF to come off rotationally hot upon predissociation, and the stabilization of the bound-states when energy is placed into HF bending, other features of the model did not agree well with experiment. First of all, experimentally it has been observed that the rotational distribution of product HF decays more or less exponentially from the highest accessible j-state, which is $j = 13$ for our system, while Ref. 43 predicted a bimodal distribution. Secondly, the computed lifetimes were generally an order of magnitude too low. Finally, the lowest energy bound-state for $v = 3$ of ArHF is predicted to have a highest accessible exit channel corresponding to $j = 12$. Thus, Ref. 43 predicts a sudden, significant drop in the predissociation rate from $v = 2$ to $v = 3$, resulting from the closing of the $j = 13$ channel. Experimentally, $j = 13$ is known to remain open all the way through $v = 4$.

Despite their deficiencies, the recent work by Buchachenko et al., and the early work by Hutson and Halberstadt (and others, see Refs.) are all important, because they illustrate the difficulty in computing the rates of the RgHX complexes. The slowness of the rates makes it necessary to use

a relatively high quality ab initio potential, in order to obtain reasonable agreement with experiment. This was simply not available at the time to Hutson, Halberstadt, or even to Buchachenko et al. Hutson has since developed an accurate ab initio potential for ArHF [50] (the H6 (4,3,2) potential), which is essentially a series of two-parameter, v_{HF}-dependent potentials.

One of us (K.G.H.), generated a high quality ab initio potential for ArHF using the CCSD(T) method and basis sets developed by Dunning and coworkers [52, 53, 54] (a more detailed discussion can be found in Ref. 45). This potential energy surface (PES) is not averaged over the vibrational states of HF, but is rather a three-dimensional potential given in terms of the standard Jacobi coordinates of ArHF. The purpose of this study is to develop a model for the predissociation of RgHX complexes which, in conjunction with the ab initio ArHF potential provided by K.G.H, can qualitatively and quantitatively predict a number of key features of the ArHF predissociation.

The predissociation is modelled as a Fermi Golden Rule (FGR) process from a bound-state residing on a PES with the ArHF van der Waals stretch and HF rotation as the slow variables, to outgoing product states residing on PES's with the ArHF stretch as the only slow variable. This approach involves a diabatic separation of the fast HF vibration from the other co-

ordinates of the ArHF complex. The rates are sufficiently slow so as to be indicative of a relatively weak interaction potential. Thus, a perturbative scheme, i.e. FGR, should be the proper approach to this problem. It should be emphasized here that this model is not restricted to ArHF, but rather any RgHX complex for which a three-dimensional PES is available.

this chapter is organized as follows: In Section 5.2 we describe in detail our quantum model for the predissociation dynamics of ArHF. In Section 5.3 we present the results and discussion. We analyze the results obtained, comparing them with what is known experimentally, and also address some numerical issues involved in computing the predissociation rates. Finally, we conclude in Section 5.4 with a summary of our main results and discuss future research.

5.2 The Model

All calculations were done in a dimensionless system of units with a reference mass of 1 a.m.u, a reference length of 1 Å, and a reference wavenumber of $1,000\ \mathrm{cm}^{-1}$. Subsection 2.1 presents the Hamiltonian governing the dynamics of the ArHF complex. Subsection 2.2 presents the diabatic approach

used to compute the bound-states of interest in this chapter. Subsection 2.3 presents the method to determine the outgoing states. Subsection 2.4 gives the FGR formula for the predissociation rates into the various exit channels. Finally, Subsection 2.5 presents a semi-analytic approach to evaluate the FGR formula using the Wigner transform. The purpose of this approach is to supplement the direct calculations, in order to circumvent numerical difficulties associated with extracting slow rates from highly oscillatory integrals.

5.2.1 The Hamiltonian

We define μ to denote a reduced mass, and set $\mu_r = \mu_{HF}$, and $\mu_R = \mu_{ArHF}$. We shall neglect the overall rotational motion of the complex, so that we can work in a body-fixed coordinate axis. Finally, by multiplying our wavefunctions by Rr, where $R \equiv |\vec{R}|$, $r \equiv |\vec{r}|$, our Hamiltonian becomes,

$$\hat{H} = \frac{\hat{p}_R^2}{2\mu_R} + \frac{\hat{p}_r^2}{2\mu_r} + u(r) - \frac{\hbar^2}{2\mu_r r^2}\left(\frac{1}{\sin\theta}\frac{\partial}{\partial\theta}\left(\sin\theta\frac{\partial}{\partial\theta}\right) + \frac{1}{\sin^2\theta}\frac{\partial^2}{\partial\phi^2}\right) + V(R, r, \theta) \tag{5.1}$$

where $u(r)$ denotes the HF interaction potential, and $V(R, r, \theta)$ is the interaction between Ar and HF.

Note that since $L_z \equiv -i\hbar\frac{\partial}{\partial\phi}$ commutes with the ArHF Hamiltonian, we need only worry about couplings amongst identical m (HF bending) states. Thus, all calculations in this chapter are carried out at constant m, which is dictated by the bound-state of interest. The bound-states are characterized as $(vjmn)$, where v is the HF vibrational quantum number, j corresponds to $\mathbf{L}^2$ for HF in the limit of infinite ArHF bond distance, m corresponds to L_z, and n is the vibrational quantum number for the Ar $\cdots$ HF stretch.

The ab initio potential, $V(R, r, \theta)$, was generated on a grid with $R = 2.5, 2.7, 2.9, 3.1, 3.3, 3.5, 3.7, 3.9, 4.1, 4.3, 4.5, 5.0, 5.5, 6.0, 6.5, 7.0, 8.0, 9.0, 10.0$, $r = 0.6, 0.7159, 0.85, 0.9168, 0.9326, 0.9648, 0.998, 1.0324, 1.06357, 1.09816$, $1.2, 1.31807, 1.4, 1.5, 1.6, 1.7$, all in Å, and $\theta = 0^\circ - 180^\circ$ in 15° intervals. The energies were given in units of cm^{-1}, but we converted the potential data to our dimensionless coordinates. A detailed discussion on the calculation of the free-HF basis and the evaluation of the potential couplings may be found in Appendix C.

5.2.2 Determining the Bound-States

For low rotational quantum numbers j, both R and θ are slow variables with respect to r. Thus, the low-j bound-states of ArHF (the only ones we are interested in for this study) reside on a two-parameter PES obtained by averaging over the vibrational quantum state of interest. To determine the bound-states for a given vibrational quantum number v, we proceed as follows: We write the full ArHF Hamiltonian as,

$$\hat{H} = \frac{\hat{p}_R^2}{2\mu_R} + \hat{H}_{HF}(r,\theta) + V(R,r,\theta) \tag{5.2}$$

The eigenstates are expanded in the product basis $|n\rangle|v,j\rangle$, where $|v,j\rangle$ denote the free-HF wave-functions, while $|n\rangle$ denotes the particle-in-a-box states for $R \in [L_1, L_2]$, where $[L_1, L_2]$ is a user-specified interval. The energies of these states are $E_n = \frac{\hbar^2\pi^2n^2}{2\mu_R L^2}$, where $L \equiv L_2 - L_1$. This is admittedly an unusual choice of basis. However, because our potential data is only given over a limited range, we wanted to be able to force the bound-states to vanish outside this range to make the numerical integrations exact. The tails of the bound-states are sufficiently small outside the range of potential data that this is a valid assumption. We reemphasize that m does not need to be expressly specified, since we only consider couplings amongst identical m

states. The matrix elements are then given by,

$$\langle n'|\langle v', j'|\hat{H}|v, j\rangle|n\rangle = (E_n + E_{vj})\delta_{nn'}\delta_{vv'}\delta_{jj'} + \langle n'|\langle v', j'|V(R, r, \theta)|v, j\rangle|n\rangle \tag{5.3}$$

For the bound-state lying on the PES corresponding to a given vibrational quantum number v, we take $v' = v$, and so the matrix elements on this PES are given by, $(E_n + E_{vj})\delta_{nn'}\delta_{jj'} + \langle n'|\langle v, j'|V(R, r, \theta)|v, j\rangle|n\rangle$. The couplings $\langle n'|\langle v, j'|V(R, r, \theta)|v, j\rangle|n\rangle$ are evaluated numerically by using a linear interpolation to $\langle v, j'|V(R, r, \theta)|v, j\rangle$ in R.

We then diagonalize in this basis to obtain the bound-states within the fixed-v subspace. A given bound-state is expressible as $\sum_{n,j} c_{nj}|n\rangle|v, j\rangle = \sum_j \sum_n c_{nj}|n\rangle|v, j\rangle$. Now, $\sum_n c_{nj}|n\rangle$ describes a wave-function $\psi_j(R)$, so that our bound-state may be written as, $\sum_j \psi_j(R)|v, j\rangle$.

This method is not the standard Born-Oppenheimer approach for finding the bound-states when R, θ are slow variables compared to r. Rather, we make a diabatic separation of the fast HF vibration coordinate r from the slow variables R, θ. The geometry of the problem is well-suited to such an approach. The reason for this is that the ArHF binding energy of ≈ 100 cm^{-1} is small compared to the HF vibrational energy spacing of ≈ 3000 cm^{-1}.

Thus, the ArHF interaction only weakly distorts the fast HF vibration.

For the R coordinate particle-in-a-box states, we used two sets of box dimensions and basis set sizes for the bound-state calculations. In the first set, we made the dimensions and basis set size as small as possible without affecting the energy of the desired bound-state. This was done so as to eliminate any residual small oscillations at the wave-function tails. In the second set, we used larger box dimensions, but used the smallest basis set possible to get the same energies as in the first set. While the two sets of bound-states appear identical, residual oscillations at the tails of the second set could lead to different dissociation rates. We computed the dissociation rates using both sets of bound-states, in order to determine the numerical stability of the final answers.

In Table 5.1 we present the calculated energies for the (1000), (2000), (2110), (3000), and (3110) bound-states. These are the bound-states whose predissociation rates we consider in this chapter. We also present the experimentally measured energies, which are also given in Ref. 3. In addition, we give the box dimensions and basis set size used to obtain these energies. Note that convergence is fairly rapid, requiring no more than 40 basis states. This is to be expected, since the ArHF interaction is fairly weak (as compared

State	Ab Initio	Experiment	L^1_{min}	L^1_{max}	N_1	L^2_{min}	L^2_{max}	N_2
(1000)	-99.99	-111.35	2.8	4.6	25	2.6	6.0	35
(2000)	-108.66	-122.61	2.8	4.7	25	2.6	6.0	40
(2110)	-38.06	-46.35	2.8	4.8	25	2.6	6.0	30
(3000)	-118.84	-135.47	2.9	4.5	20	2.6	6.0	30
(3110)	-42.86	-52.13	2.8	4.7	10	2.6	6.0	15

Table 5.1: Energies of a sample of ArHF bound-states (in cm^{-1}) with respect to the corresponding $v, j = 0$ free-HF state. Column 2: The calculated energies. Column 3: The experimental energies. Columns 4 & 5: The first set of box dimensions. Column 6: The maximum particle-in-a-box energy level in the basis used for the first set of box dimensions ($n = 1 - N_{\max}$). Column 7 & 8: The second set of box dimensions. Column 9: The maximum particle-in-a-box energy level in the basis used for the second set of box dimensions.

with the HF potential).

The agreement between theory and experiment is fairly good; however, as with the free-HF states, we use the experimental values for the energies in the dissociation calculations in this chapter. The reasons for this are discussed in the Conclusions and in Appendix C.1 on the free-HF basis.

5.2.3 Determining the Outgoing States

To determine the dissociated wavefunction corresponding to product HF exiting with energy E in the state $|v,j\rangle$, we average the Hamiltonian over the state $|v,j\rangle$ of interest, thereby obtaining a PES depending only on R, on which we can construct the outgoing wave. For the high-j states, the rotational energy gaps are on the order of 500 cm^{-1}, while the translational energy gaps are on the order of a few 10's of cm^{-1}. Thus, at high-j, both r and θ are fast variables, so that this approach is exactly the crude Born-Oppenheimer approximation. We expect negligible mixing amongst the high-j channels, so that the decay rates into them are equivalent to the decay rates into the corresponding product HF states. For the lower j states, only r is a fast variable, so that this approach neglects mixing amongst the low-j chan-

nels. Thus, while the couplings to these channels are sufficiently small so that the decay rates into them are given by an FGR approach, interchannel mixing makes these decay rates different from the decay rates into the corresponding product HF states. Nevertheless, since we expect the product HF to be rotationally hot, the decay rates into the low-j channels should be negligible, rendering interchannel mixing irrelevant. Thus, this method is directly applicable only to the RgHX complexes. For the RgX_2 complexes the decay rates are predominantly into the low-j channels, so channel mixing needs to be taken into account in order to properly determine the rotational distribution.

The one-parameter Hamiltonian becomes,

$$\hat{H}_R = \frac{-\hbar^2}{2\mu_R}\frac{d^2}{dR^2} + V_{vj}(R) + E_{vj} \tag{5.4}$$

where $V_{vj}(R) \equiv \langle v, j|V|v, j\rangle$. To obtain a solution $f(R)$ of energy E, we numerically integrate the following pairs of equations:

$$\frac{df}{dR} = g \tag{5.5}$$

$$\frac{dg}{dR} = -\frac{2\mu_R}{\hbar^2}(E - E_{vj} - V_{vj}(R))f \tag{5.6}$$

The only issue here is obtaining a set of initial conditions. The potential data only goes from some $R_{min} > 0$ to some R_{max}, so we only find the out-

going waves over this range. For simplicity, set $V_{vj}(R) = V_{vj}(R_{min})$ for $R \in [0, R_{min}]$, with the stipulation that f must vanish at $R = 0$. The vanishing of f at $R = 0$ is accomplished by assuming a hard wall at $R = 0$ (the difference is negligible if R is simply allowed to go to $-\infty$ and $V_{vj}(R) = V_{vj}(R_{min})$ for $R \in (-\infty, R_{min}]$). The initial conditions are obtained by solving for f in the range $[0, R_{min}]$. Setting $f(R_{min}) = 1$, combined with the requirement that $f(0) = 0$, is sufficient to determine $g(R_{min}) = f'(R_{min})$.

After we obtain the solution to our system of ODE's, we need to normalize the wavefunction so that the outgoing states have the $\delta(E - E')$ normalization convention. This requires that the wavefunction have an oscillation amplitude of $(\frac{2m}{\pi^2\hbar^2(E-E_{vj})})^{\frac{1}{4}}$ in the large R limit.

5.2.4 Computing the Dissociation Rate

The dissociation rate is computed using Fermi's Golden Rule. For a bound-free dissociation process in which the outgoing continuum states have the $\delta(E - E')$ normalization, the FGR formula gives a decay rate into a given exit channel of,

$$\Gamma = \frac{2\pi}{\hbar} |\langle \phi_o | \hat{H} | \phi_b \rangle|^2 \tag{5.7}$$

where $|\phi_b\rangle$ denotes the bound state, and $|\phi_o\rangle$ denotes the given exit channel outgoing state with energy equal to the bound-state energy. The key feature to note here is that the predissociation is from a bound-state obtained from a Hamiltonian with two slow variables, to outgoing states obtained from a Hamiltonian with one slow variable. Nevertheless, the FGR rate is obtained by inserting the full Hamiltonian $\hat{H}$ between the bound-state and a given outgoing state. The basic idea is that although the bound and outgoing states are generated from different Hamiltonians, they lie on surfaces with different free-HF vibrational quantum numbers, and so the only term in the Hamiltonian which couples the bound and outgoing states is the ArHF interaction $V(R, r, \theta)$.

The bound state is given by $\sum_j \psi_j(R)|v, j\rangle$, and since we look at $v \to v-1$ transitions, the outgoing state is given by $\phi_{j'}(R)|v-1, j'\rangle$. We evaluate the coupling integral numerically, by using linear interpolation on $\phi_{j'}$, ψ_j, and $V_{(v-1)vj'j}$, where $V_{(v-1)vj'j}(R) \equiv \langle v-1, j'|V|v, j\rangle$. The bound-states were evaluated on a $1,000$-point equally spaced grid from $R = 2.5 - 10.0$ Å, and the outgoing states were evaluated on a $600,000$-point equally spaced grid from $R = 2.5 - 10.0$ Å. A qualitative illustration of the coupling between a bound-state and a given exit channel is given in Figure 5.1.

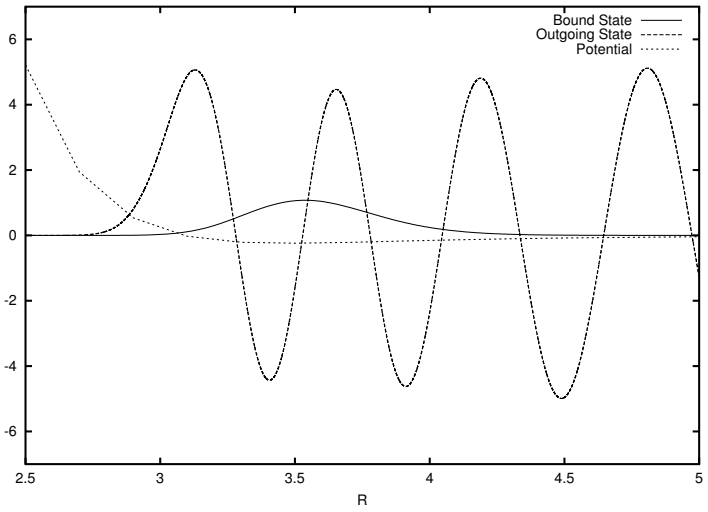

Figure 5.1: Qualitative illustration of the coupling between a bound-state and a given exit channel. The plot is of some $\psi_j(R)$ component of a given bound-state, some outgoing wave $\phi_{j'}(R)$, and the coupling $V_{(v-1)vj'j}(R)$.

5.2.5 Semi-Analytical Model

As we shall see in the Results and Discussion, the highly oscillatory outgoing wavefunctions make it difficult to accurately compute the lower j predissociation rates. The result of this is that the numerics prevent us from extracting the rotational distribution predicted by the model. It would be desirable to supplement our calculations with another integration technique which more faithfully reproduces the rotational distribution. To this end, we begin by

defining $|\psi_{vj'}\rangle$ via $\langle R|\psi_{vj'}\rangle = \psi_{vj'}(R) = \sum_j \psi_j(R) V_{(v-1)vj'j}(R)$. Then,

$$\langle \phi_o|\hat{H}|\phi_b\rangle = \int_{-\infty}^{\infty} dR \phi_{j'}(R)\psi_{vj'}(R) = \langle \phi_{j'}|\psi_{vj'}\rangle \tag{5.8}$$

where $\phi_{j'}(R) = \psi_{vj'}(R) = 0$ for $R \in \mathbf{R}/[R_{min}, R_{max}]$. The FGR rate into the $|v-1, j'\rangle$ channel is then given by $\frac{2\pi}{\hbar}|\langle \phi_{j'}|\psi_{vj'}\rangle|^2$. We can eliminate the oscillatory nature of the overlap integral by applying the Wigner transform to both $\psi_{vj'}(R)$ and $\phi_{j'}(R)$. Briefly, the Wigner transform converts a wavefunction $\psi(R)$ into a two-dimensional phase-space distribution function $\rho_{W,\psi}(R, p_R)$. It is given by,

$$\rho_{W,\psi}(R, p_R) = \frac{1}{2\pi\hbar}\int_{-\infty}^{\infty} ds \psi(R+s)\bar{\psi}(R-s)\exp(-2ip_R s/\hbar) \tag{5.9}$$

The FGR rate may then be written as,

$$\Gamma = 16\pi^2 \int_{-\infty}^{\infty}\int_{-\infty}^{\infty} dR dp_R \rho_{W,\psi_{vj'}}(R, p_R)\rho_{W,\phi_{j'}}(R, p_R) \tag{5.10}$$

At first glance, it may appear that we've simply complicated the problem by introducing two integration variables, instead of just one. However, because $\phi_{j'}(R)$ is the eigenstate of energy E of the one-dimensional Hamiltonian,

$$H_{vj'}(R, p_R) = \frac{p_R^2}{2\mu_R} + V_{vj'}(R) + E_{vj'} \tag{5.11}$$

to lowest-order in $\hbar$ it can be shown that $\rho_{W,\phi_{j'}}(R,p_R) = \frac{1}{4\pi\hbar}\delta(E-H_{vj'}(R,p_R))$, that is, $\rho_{W,\phi_{j'}}$ is simply proportional to the classical microcanonical distribution. Thus, the oscillatory nature of the overlap integral has been eliminated. Furthermore, the initial state distribution $\psi_{vj'}(R)$ may be reasonably approximated with a gaussian, so that its Wigner transform is itself a gaussian. This results in an integral that can be readily evaluated using MATHEMATICA.

The above approach to this particular system was developed in Ref. 59. This reference also contains a good review of the Wigner transform formalism.

5.3 Results and Discussion

5.3.1 The Dissociation Rates

The FGR predissociation rates were computed for the (1000), (2000), (2110), (3000) and (3110) states. Two sets of rates were computed, corresponding to the two sets of bound-states obtained. The results are presented in Tables 5.2-6.

We begin by noting that only the $j = 13$ rates are relatively stable. The rates show significant discrepancies between the two sets of bound-states

Product State	Decay Rate 1 (s^{-1})	Decay Rate 2 (s^{-1})
$\|0, 13\rangle$	1.67×10^2	1.67×10^2
$\|0, 12\rangle$	8.95×10^0	1.13×10^1
$\|0, 11\rangle$	1.66×10^0	1.59×10^0
$\|0, 10\rangle$	1.04×10^1	1.14×10^1
$\|0, 9\rangle$	8.01×10^2	4.01×10^2
$\|0, 8\rangle$	2.09×10^2	4.01×10^1
$\|0, 7\rangle$	1.68×10^1	5.61×10^1
$\|0, 6\rangle$	2.37×10^2	3.19×10^2
$\|0, 5\rangle$	1.49×10^3	1.23×10^3
$\|0, 4\rangle$	6.64×10^3	5.30×10^3
$\|0, 3\rangle$	4.14×10^4	3.23×10^4
$\|0, 2\rangle$	1.40×10^5	1.29×10^5
$\|0, 1\rangle$	1.83×10^5	2.04×10^5
$\|0, 0\rangle$	5.62×10^4	5.19×10^4

Table 5.2: Dissociation rates for the (1000) state. Column 1 gives the rates corresponding to the bound-state computed using the first set of box dimensions. Column 2 gives the rates corresponding to the bound-state computed using the second set of box dimensions.

Product State	Decay Rate 1 (s^{-1})	Decay Rate 2 (s^{-1})
$\|1,13\rangle$	1.39×10^4	1.39×10^4
$\|1,12\rangle$	8.06×10^1	7.17×10^1
$\|1,11\rangle$	1.34×10^3	1.29×10^3
$\|1,10\rangle$	3.00×10^3	2.56×10^3
$\|1,9\rangle$	1.11×10^2	4.72×10^1
$\|1,8\rangle$	7.76×10^1	8.28×10^0
$\|1,7\rangle$	7.56×10^2	1.19×10^3
$\|1,6\rangle$	1.08×10^3	1.23×10^2
$\|1,5\rangle$	2.65×10^2	4.56×10^2
$\|1,4\rangle$	2.47×10^3	5.52×10^2
$\|1,3\rangle$	9.51×10^3	1.41×10^4
$\|1,2\rangle$	1.13×10^4	1.80×10^4
$\|1,1\rangle$	4.57×10^4	3.44×10^4
$\|1,0\rangle$	7.97×10^4	8.72×10^4

Table 5.3: Dissociation rates for the (2000) state. Column 1 gives the rates corresponding to the bound-state computed using the first set of box dimensions. Column 2 gives the rates corresponding to the bound-state computed using the second set of box dimensions.

Product State	Decay Rate 1 (s^{-1})	Decay Rate 2 (s^{-1})
$\|1,13\rangle$	6.24×10^{1}	6.31×10^{1}
$\|1,12\rangle$	7.05×10^{1}	9.35×10^{1}
$\|1,11\rangle$	7.83×10^{2}	6.07×10^{2}
$\|1,10\rangle$	3.42×10^{1}	9.38×10^{0}
$\|1,9\rangle$	5.65×10^{2}	3.98×10^{2}
$\|1,8\rangle$	8.20×10^{1}	1.07×10^{2}
$\|1,7\rangle$	3.61×10^{1}	3.17×10^{0}
$\|1,6\rangle$	4.47×10^{1}	3.51×10^{-2}
$\|1,5\rangle$	9.45×10^{-1}	6.95×10^{1}
$\|1,4\rangle$	3.83×10^{3}	3.74×10^{3}
$\|1,3\rangle$	4.61×10^{2}	4.18×10^{2}
$\|1,2\rangle$	3.91×10^{3}	2.74×10^{3}
$\|1,1\rangle$	1.11×10^{4}	1.21×10^{4}

Table 5.4: Dissociation rates for the (2110) state. Column 1 gives the rates corresponding to the bound-state computed using the first set of box dimensions. Column 2 gives the rates corresponding to the bound-state computed using the second set of box dimensions.

Product State	Decay Rate 1 (s^{-1})	Decay Rate 2 (s^{-1})
$\|2, 13\rangle$	1.99×10^5	1.98×10^5
$\|2, 12\rangle$	4.31×10^3	3.82×10^3
$\|2, 11\rangle$	2.54×10^3	4.24×10^3
$\|2, 10\rangle$	2.16×10^4	1.72×10^4
$\|2, 9\rangle$	2.54×10^4	1.56×10^4
$\|2, 8\rangle$	1.20×10^4	1.28×10^4
$\|2, 7\rangle$	9.71×10^3	9.10×10^3
$\|2, 6\rangle$	4.71×10^2	7.04×10^2
$\|2, 5\rangle$	5.60×10^3	2.51×10^1
$\|2, 4\rangle$	1.07×10^4	9.10×10^3
$\|2, 3\rangle$	5.43×10^4	2.92×10^4
$\|2, 2\rangle$	1.38×10^5	1.24×10^5
$\|2, 1\rangle$	6.76×10^4	1.92×10^5
$\|2, 0\rangle$	4.09×10^4	2.16×10^4

Table 5.5: Dissociation rates for the (3000) state. Column 1 gives the rates corresponding to the bound-state computed using the first set of box dimensions. Column 2 gives the rates corresponding to the bound-state computed using the second set of box dimensions.

Product State	Decay Rate 1 (s^{-1})	Decay Rate 2 (s^{-1})
$\|2, 13\rangle$	1.21×10^4	1.24×10^4
$\|2, 12\rangle$	1.48×10^2	4.72×10^2
$\|2, 11\rangle$	1.83×10^3	1.62×10^2
$\|2, 10\rangle$	3.87×10^3	2.04×10^4
$\|2, 9\rangle$	1.08×10^3	1.14×10^3
$\|2, 8\rangle$	6.45×10^2	7.55×10^1
$\|2, 7\rangle$	2.54×10^0	6.83×10^3
$\|2, 6\rangle$	3.33×10^0	6.65×10^3
$\|2, 5\rangle$	5.59×10^2	4.29×10^3
$\|2, 4\rangle$	4.82×10^2	6.82×10^3
$\|2, 3\rangle$	3.18×10^4	4.71×10^4
$\|2, 2\rangle$	2.29×10^4	3.61×10^4
$\|2, 1\rangle$	5.06×10^3	6.23×10^3

Table 5.6: Dissociation rates for the (3110) state. Column 1 gives the rates corresponding to the bound-state computed using the first set of box dimensions. Column 2 gives the rates corresponding to the bound-state computed using the second set of box dimensions.

already at $j = 12$. We will discuss the reasons for this later in this section. We should note that our semi-analytic model using the Wigner transform deals with this problem quite well. We will also return to this later, but for now we should note that it indicates that the rates drop off sharply with decreasing j, so that essentially all of the dissociation occurs into the $j = 13$ channel. The experimental distribution is considerably broader. Possible reasons for this discrepancy will be discussed. For now, however, we will focus on the $j = 13$ rates for the various bound- states, since we believe that these are the only ones that are significant.

The predissociation rate from the (1000) state to the $|0, 13\rangle$ exit channel was determined to be $\approx 170\ \mathrm{s}^{-1}$. Using our semi-analytic Wigner transform approach, we obtained a corresponding rate of $1,570\ \mathrm{s}^{-1}$. Both these rates are below $1,600\ \mathrm{s}^{-1}$, which is currently around the lower limit for an experimentally measurable rate. Thus, we have managed to confirm the experimental observation that the (1000) predissociation rate is too slow to be measured [56]. Note that even though the exact and semi-analytic results differ by a factor of ten in this case, they are experimentally equivalent, because all one can say at this point about the (1000) state is that its predissociation rate is less than $1,600\ \mathrm{s}^{-1}$.

For the (2000) state, we get a vibrational predissociation rate into the $|1, 13\rangle$ channel of $\approx 14,000\ \mathrm{s}^{-1}$, which is measurable. The semi-analytic value is $16,000\ \mathrm{s}^{-1}$. Indeed, the (2000) decay rate has been measured by Miller [57], although an actual number was not given. Therefore, all we can say about the (2000) state at this point is that our numerics are consistent with the fact that this state has a measurable predissociation rate.

For the (2110) state, we get a vibrational predissociation rate into the $|1, 13\rangle$ channel of $\approx 60\ \mathrm{s}^{-1}$, which is much too small to be measured. The semi-analytic value is $1,070\ \mathrm{s}^{-1}$. Again, while the two rates are off by an order of magnitude, they are both experimentally equivalent, since they both predict that the predissociation rate is too slow to be measured. Indeed, it has been observed experimentally by Miller that the (2110) state predissociates too slowly to have a measurable rate.

We calculated the predissociation rate of the (3000) state into the $|2, 13\rangle$ exit channel to be $\approx 200,000\ \mathrm{s}^{-1}$, as compared with the experimentally measured value of $120,000\ \mathrm{s}^{-1}$. The corresponding semi-analytic result is $160,000\ \mathrm{s}^{-1}$. Our computed rate is thus well within the order of magnitude of the measured rate.

Finally, the vibrational predissociation rate of the (3110) state into the

$|2,13\rangle$ exit channel was calculated to be $\approx 12,000\ \mathrm{s}^{-1}$. The semi-analytic value was $7,600\ \mathrm{s}^{-1}$. These values, while within an order of magnitude of the measured rate, seem somewhat low, given that the (3110) lifetime is only twice as long as the (3000) lifetime [44]. We don't have an explanation for this discrepancy, since the numerics seem fairly clear cut. One possibility on the computational side has to do with the fact that the wavefunction tails are the main contributors to the predissociation rates. This tends to make the rates somewhat sensitive to the shape of the bound-states. Given that our bound-state energies typically have errors on the order of $10-15\%$, there could be sufficient errors at the tails to significantly affect the computed rates.

Another reason for the low (3110) rate may lie in the ab initio potential itself. We distorted the PES according to the equation $V_{new}(R,r,\theta) = V_{eq} + (1+\delta)(V_{old}(R,r,\theta) - V_{eq})$, where $V_{eq} = -202.928\ \mathrm{cm}^{-1}$ is the value of the PES at the equilibrium ArHF configuration, and δ is a dilation parameter. For $\delta = 0.1$ we found that the $j = 13$ rates increased by a factor of 2 for the (3110) state, and by about 50% for the (3000) state. For $\delta = 0.2$, the $j = 13$ rate increased by another factor of 2 for the (3110) state, and by 33% for the (3000) state. For $\delta = -0.1$, the $j = 13$ rates for both (3110) and (3000)

dropped by a factor of 2, and then again by another factor of 2 for $\delta = -0.2$. A factor of 2 or 4 increase in our computed $j = 13$ rate brings the value up to $24,000\ \mathrm{s}^{-1}$ or $48,000\ \mathrm{s}^{-1}$, which is already in much better agreement with experiment. Note that the distortion is relatively small around the equilibrium ArHF configuration, and so only becomes appreciable where the ArHF potential becomes large, that is, for small R. This suggests that there could be errors at small R in the ab initio PES that would account for the rate discrepancies with experiment. Certainly the above results indicate that this requires further investigation.

Two features of interest are the strong v-dependence of the predissociation rates, and the stabilizing effect that occurs when m is increased from 0 to 1. The first feature can be explained by noting that as v is increased, the average HF bond length increases, and so the HF experiences more of the anharmonicity of the ArHF interaction. The result is an increased coupling to the outgoing states, and consequently a faster predissociation rate. The effect is dramatic: The (3000) predissociation rate is $2-3$ orders of magnitude larger than the (1000) predissociation rate (depending on whether one uses the exact or semi-analytic (1000) result). Indeed, Klemperer and coworkers have argued that a v^4 power law describes the pattern of the (v000)

predissociation rates [44].

The second feature can be explained by noting that increasing m from 0 to 1 places some of the HF rotation into the plane perpendicular to the ArHF van der Waals vector $\vec{R}$. This reduces the extent to which the HF samples the anisotropy of the ArHF interaction inside the potential well. Thus, while this results in the $m = 1$ bound-states being more weakly bound than the $m = 0$ bound-states, their lifetimes are considerably longer. This accounts for the (2000) predissociation rate being measurable, but the computed rate for (2110) being too slow to be measurable. As noted above, our calculations may be overestimating this effect, since the computed predissociation rate of the (3000) state is approximately 20 times larger than that of the (3110) state.

5.3.2 The Rotational Distribution

As mentioned previously, we encountered numerical difficulties computing the predissociation rates already for $j = 12$. This will be addressed shortly, but for now we should note that the semi-analytic approach based on the Wigner transform did not encounter any such numerical difficulties. To

get an idea of what our computed rotational distribution should look like, we computed the predissociation rates for the (3000) bound-state into the $|v = 2, j = 12, 11, 10, 9$ exit channels. The semi-analytic results are $\Gamma = 25\ \mathrm{s}^{-1}, 0.12\ \mathrm{s}^{-1}, 0.0015\ \mathrm{s}^{-1}, 0.00019\ \mathrm{s}^{-1}$ respectively. A similar pattern was obtained with the other states, which persists all the way down to the low-j channels. Given that the semi-analytic approach quantitatively reproduces the $j = 13$ rates, we believe that this is strong evidence that numerically essentially all of the predissociation occurs into the $j = 13$ channel, and that there is a sharp, continuous decay in the predissociation rates with decreasing j.

It is possible that the Wigner-based approach somewhat underestimates the $j = 12$ and lower rates. The main contribution to the predissociation rate comes from the inner tail region of the bound-states. This is due to two factors: First, the interaction potential becomes large in the inner tail region where R is small. Second, for R smaller than the classical inner turning point of the outgoing channels, the outgoing wavefunctions are no longer oscillatory, so that the coupling with the bound-state does not get cancelled. The lower j, the smaller R required to be in the classically forbidden region, and hence the smaller the corresponding tails of the bound-states. Already for $j = 12$,

the important integration region is sufficiently deep in the inner tail region that the relatively rapidly decaying gaussian fit could underestimate the value of the initial state distribution. The problem with correcting this is that the tails are already sufficiently small that the discrepancy is not very noticeable. This is not particular to the Wigner approach, but rather reflects one source of difficulty in computing lower j rates: The lower j rates get their main contribution from the far tail regions of the bound-states. The tails are so small here that there is significant uncertainty associated with them, making the computed rates unreliable. Another major difficulty involving oscillatory integrals is discussed in the next subsection.

In any event, our model successfully captures the experimental observation that the ArHF complex preferentially predissociates into the highest accessible rotational channel. The main discrepancy with experiment is that our rotational distribution is considerably sharper than that observed experimentally. One possible source of this discrepancy is our neglect of interchannel coupling at high-j. Thus, it could be that the $j = 13$ channel serves as a gateway for FGR decay into the lower j channels. To check this, we computed the interchannel couplings for the various bound-states. Because we are dealing with $\delta(E - E')$ normalization in the outgoing channels,

the interchannel couplings are dimensionless. To use a specific case, for the (3000) state the $j = 13/j = 12$ coupling was ≈ 0.006. Since the relevant parameter for FGR is $|V|^2$ as opposed to $|V|$, we get that the rate into the $j = 12$ channel should be on the order of $0.006^2 \times 200,000\ \mathrm{s}^{-1} = 7.2\ \mathrm{s}^{-1}$, where $200,000\ \mathrm{s}^{-1}$ is the rate into the $j = 13$ channel. As a comparison, the $j = 1/j = 0$ coupling was ≈ 0.17. This gives a $|V|^2$ which is 800 times larger than that for the $j = 13/j = 12$ coupling. A similar pattern was observed for the other states, so we obtain that interchannel coupling appears to give a negligible contribution to the rates at high-j. At low-j interchannel coupling becomes significant, but is unimportant since the low-j predissociation rates are negligible.

The interplay of three factors results in a rotationally hot product HF. First of all, the more excess vibrational energy is placed into translation, the more oscillatory the corresponding outgoing wave. This results in a suppression of the predissociation rates as one goes from high-j to low-j. Of course, placing energy into rotation results in an oscillatory angular component to the outgoing wavefunction. This would have a tendency to suppress the high-j rates relative to the low-j rates. However, the lightness of H gives HF a relatively large rotational constant, so that for a given energy, the oscilla-

tory character of the outgoing wave is minimized by placing the energy into rotation. Finally, the ArHF interaction potential has a strong θ anisotropy, which monotonically increases with $|r - r_{eq}|$. Indeed, a plot of V as a function of θ revealed a sharply peaked gaussian about $\theta = 0°$. This allows for effective coupling between the low-j components of the bound-states to the high-j outgoing waves. While the low-j/low-j couplings are significantly stronger, the anisotropy makes the low-j/high-j couplings sufficiently strong that, combined with the previous two effects suppressing the low-j channels relative to the high-j ones, results in a rotationally hot product HF.

5.3.3 Numerical Issues

We may note that the two sets of rates given in Tables 5.2-6 already show significant discrepancies at $j = 12$, in some case differing by $2 - 3$ orders of magnitude! This can be explained fairly simply: As we go to lower j, the outgoing states have more translational energy, making them more oscillatory. Furthermore, the (r, θ) couplings from the low-j states comprising the bound-states to the outgoing states increase by several orders of magnitude as we drop to lower j. The result is that as we go to lower j, the numerical

integration involves adding larger and larger numbers of more rapidly varying sign. While we expect the oscillatory nature of the outgoing waves to essentially kill the coupling at lower j, the numerical precision on the computer is insufficient to cancel out the additions and subtractions of the larger couplings to the extent required to give an accurate result for the integration. For the higher j states, the integral is less oscillatory, and the couplings are much smaller, so the additions and subtractions do not need to be as exact as for the lower j in order to get an accurate rate. This explains why no matter what the $j = 13$ rate is for all the bound states, the lower j rates tend to jump to values on the order of $10^3 - 10^5$ s^{-1}. In our dimensionless system of units, this corresponds to a rate on the order of $10^{-11} - 10^{-9}$. The numerical precision available on our computer can only cancel out the lower j coupling terms to this level.

In Ref. 43 Buchachenko et al. obtained a rotational distribution which had a bimodal character. Their calculations gave bound-state lifetimes which were typically an order of magnitude too low. We believe that this bimodal distribution, as well as the low lifetimes, is at least partly due to the numerical issues described here. As can be seen in Tables 2a-e, the numerical integrations give a bimodal distribution, and significantly overestimate the

low-j rates, so that the total predissociation rates are an order of magnitude or more larger than those measured experimentally.

5.4 Conclusions and Future Research

This chapter developed a model for the vibrational predissociation dynamics of RgHX complexes as an FGR decay from a bound-state residing on a two-parameter PES to a series of one-parameter exit channels. Using a high quality ab initio ArHF PES, we applied this model to the ArHF complex. This model gave rates for the (1000) and (2110) states that were consistent with the observation that predissociation of these bound-states is too slow to be currently measured. The computed rate for the (2000) state was found to be consistent with its predissociation being observable, though no actual experimental value has been given to date. For the (3000) state, the computed $j = 13$ predissociation rate of $200,000\ \mathrm{s}^{-1}$ is in good agreement with the overall predissociation rate of $250,000\ \mathrm{s}^{-1}$. Indeed, of the five bound-states considered in this paper, the only problematic state is the (3110) state, whose computed predissociation rate into the $j = 13$ channel of $12,000\ \mathrm{s}^{-1}$ is somewhat low, though still within an order of magnitude of experiment.

Numerical tests with a distorted potential suggest that this rate discrepancy may have nothing to do with our theoretical approach to the problem, but rather may be due to errors in the ab initio PES for ArHF, in particular at small R.

While our approach was not a pure ab initio one, in that we adjusted the free-HF and bound-state energies to the experimentally calculated ones (see Appendix A.1), we should note that a full ab initio approach would nevertheless have given similar results to the ones obtained in this chapter. To illustrate, using adjusted free-HF and bound-state energies gave a predissociation rate from the (3000) to the $|v = 2, j = 13\rangle$ exit channel of $200,000$ s^{-1}, with a product HF translational energy of 87 cm^{-1}. A pure ab initio calculation, with no parameters adjusted, gave a corresponding decay rate of $160,000$ s^{-1} and a translational energy of 54 cm^{-1}.

Our model successfully predicts the strong v-dependence of the predissociation rates, as well as the stabilization of the bound-states that occurs when energy is placed into HF bending, i.e., when m is increased from 0 to 1. Combined with the semi-analytic results, we also managed to confirm the experimental observation that the product HF tends to come off with the highest accessible j, which was $j = 13$ for the bound-states considered. As

mentioned in the previous section, this results from the interplay of three factors: (1) The relatively large rotational constant of HF. (2) A strong angular anisotropy in the ArHF interaction potential (the gaussian in θ mentioned in the previous section). (3) Highly oscillatory low-j outgoing waves, as compared to high-j outgoing waves, which suppress the predissociation rates into the low-j channels as compared to the high-j ones. We should note that this explanation is not original, having been noted, for instance, in Ref. 1. However, we felt it should be restated here, since it is a conclusion which follows from our investigations. In fact, as discussed in the Introduction, it can be argued that this explanation is actually due to Ewing (up to some details particular to this system).

The main discrepancy between our model and experiment is that our model predicts essentially all of the predissociation to occur into the $j = 13$ channel. The semi-analytic computations give a sharp, more or less exponential decay in the rates with decreasing j. Experimentally the distribution is considerably broader, with significant probability in the $j = 9 - 13$ range. The experimental decay is also essentially exponential, with a slight exception for the (3110) state, which shows a slightly larger $j = 12$ rate than the $j = 13$ rate. Our current numerical evidence suggests that interchannel

mixing has a negligible effect on the rotational distribution, so that at this point we don't have a good explanation for these discrepancies. A higher level of theory may be required to properly address this situation, either in the computation of the bound-states, or in the outgoing channels, or both. The simplicity of our current model makes it a convenient springboard for more complicated, and hopefully more accurate, approaches. We leave this for future work.

As mentioned previously, it may also be necessary to obtain a more accurate ab initio PES. It should be re-emphasized that the slowness of the predissociation rates make their numerical evaluation difficult. This is especially true for the lower j rates, where their slowness complicates their accurate evaluation due to oscillatory integrals. Thus, although the current ab initio ArHF PES is of relatively high quality, it is not clear that we could have obtained much better results with it using a higher level of theory.

On the experimental side, we should note that one of us (W.K.) has reason to believe that the current measurements on the $v = 3$ bound-states of ArHF may overestimate the lower j populations. This is therefore an issue which may also require further experimental investigation. It could very well happen that the true rotational distributions fall somewhere between the

current theoretical and experimental results.

We should also restate here that the main contribution to the bound-free coupling is in the inner wall region of the ArHF potential, at the bound-state tails. This means that the bulk of the bound-free coupling is in the classically forbidden region, so that the predissociation process is due to tunneling and is therefore a purely quantum effect. Classical simulations will fail to take the inner wall region of the ArHF potential into account, and so will give predissociation rates which are too low.

Our current model can be used to study other RgHX complexes, provided that an ab initio potential can be obtained for those. In particular, one complex of interest is KrHF, whose predissociation even at $v_{HF} = 3$ is too slow to be measured. One possible explanation for this is that the KrHF interaction potential is signficantly stronger than the ArHF interaction. This could result in a bound-state energy sufficiently low to close the $j = 13$ channel, leading to a sharp drop in the predissociation rates.

Future research plans involve extending our model to study other van der Waals complexes, such as CO-HF, N_2HF, $(HF)_2$, and Ar_3HF. These complexes have predissociation rates which are several orders of magnitude larger than those of ArHF, and it would be interesting to see if this can be

confirmed numerically. Although these systems are computationally more difficult to work with because they have more degrees of freedom, it may be possible to more accurately extract the predissociation rates because they are much larger. Finally, we hope to develop the Wigner approach and see if it is possible to bring it into quantitative agreement with the numerics for all the bound-states considered. Because the Wigner-based approach does not suffer from the same numerical instabilities that direct integration does, such an approach could replace the direct integration as a method for computing the predissociation rates. The Wigner-based approach has the additional advantage that it provides physical insight, by giving a phase-space picture of the predissociation process.

Chapter 6

Determination of Bound-Free Dissociative Couplings Via Classical Fourier Coefficients

This chapter presents an approach to compute couplings between bound and unbound wavefunctions using only classical Fourier coefficients of the Hamiltonian. This approach is an extension of the well-known technique of using Fourier coefficients in the action-angle representation to compute bound-state to bound-state couplings. We develop the analogous bound-free approach for

one-dimensional Hamiltonians and demonstrate it for several coupling potentials. The generalization to higher dimensions is also discussed.

6.1 Introduction

Let $H(\phi, \mathbf{I})$ denote a D degree-of-freedom Hamiltonian expressed in some action-angle basis $(\phi, \mathbf{I})$, $\phi \in [0,1]^D$. The EBK semiclassical quantization method associates a wavefunction with those actions $\mathbf{I} = (I_1, \ldots, I_D)$ satisfying $I_i = 2\pi\hbar(n_i + \alpha_i/4)$, where each n_i is a nonnegative integer, and the α_i denote the Maslov indices. Usually $\alpha_i = 2$.

These semiclassical wavefunctions may be characterized by their quantum numbers $(n_1, \ldots, n_D)$, and give rise to a basis set $\{|n_1, \ldots, n_D\rangle\}$ which may be used in quantum calculations. The coupling between two semiclassical wavefunctions $|\mathbf{n}\rangle = |n_1, \ldots, n_D\rangle$ and $|\mathbf{m}\rangle = |m_1, \ldots, m_D\rangle$ is given by [9],

$$\langle \mathbf{m}|\hat{H}|\mathbf{n}\rangle = H_{\mathbf{m}-\mathbf{n}}(\frac{\mathbf{I_m} + \mathbf{I_n}}{2}) \tag{6.1}$$

$I_\mathbf{m}$, $I_\mathbf{n}$ denote the action vectors corresponding to the quantum numbers $\mathbf{m}$, $\mathbf{n}$, respectively, and $H_\mathbf{k}(\mathbf{I})$ denotes the $\mathbf{k}$ Fourier component of H evaluated

at $\mathbf{I}$, defined via the expansion,

$$H(\phi, \mathbf{I}) = \sum_{\mathbf{k}} H_{\mathbf{k}}(I) e^{2\pi i \mathbf{k} \cdot \phi} \tag{6.2}$$

This semiclassical coupling formula is well-known, and has proven useful in semiclassical approaches to the quantum dynamics of bound systems [1, 2, 3, 7, 9].

What about dissociative processes? That is, given a bound-state and a continuum state which are both eigenstates of some zeroth-order Hamiltonian H_0, and a perturbation V, is it possible to express the V-induced dissociative coupling between the two in terms of the classical Fourier coefficients of V? Such a formula would be useful for extending semiclassical analyses based on classical Fourier coefficients to problems involving bond breaking (vibrational predissociation is one good example). Because semiclassical representations of the Hamiltonian based on classical Fourier coefficients grew out of the EBK method, these approaches required an action-angle representation of the Hamiltonian, and were therefore limited to bound-bound processes. In addition, the traditional focus within this area of semiclassical methods has been on energy spectra, so there has not been a major impetus to develop an analogous semiclassical formula for dissociative processes.

For unbound-unbound processes, Maitra and Heller [11] developed an approach based on the use of WKB wavefunctions as a distorted-wave basis. Specifically, they considered the problem of above-barrier reflection in one-dimension, and showed that the use of the WKB wavefunctions worked well at essentially all above-barrier energies as a distorted-wave basis in the first-order Born approximation. While their coupling formula was not given in terms of classical Fourier coefficients of the Hamiltonian, it is possible to show that, in a sufficiently semiclassical limit, the coupling formula may be given in such a form.

In their paper, Maitra and Heller discussed the idea of obtaining a general method to assign a semiclassical quantum coupling between any two contours in phase-space. In particular, such a formula would include the ability to compute couplings between wavefunctions corresponding to bound and unbound phase-space contours.

The difficulty in generalizing the bound-bound coupling formula to the bound-free case is that there is a sudden change in the topology of the phase-space in going from the bound regime to the unbound regime. In the bound regime it is possible to semiclassically characterize the wavefunctions by quantum numbers corresponding to definite values of the classical action,

while in the unbound regime this is not possible. Thus, it is not immediately obvious in what canonical basis to Fourier expand the Hamiltonian.

This chapter presents a successful approach to this problem. Specifically, we extend the bound-bound formula to the bound-free case for D-dimensional separable systems, where the potential for each degree of freedom has a repulsive inner wall, and supports both bound and unbound states. This approach therefore includes most chemically interesting systems, since chemical bonds are often describable with such potentials (e.g. the Morse potential).

This chapter is organized as follows: In Section 6.2, we develop the one-dimensional system which we will consider. We go on in Section 6.3 to construct the semiclassical bound and unbound states, and in Section 6.4 we derive the semiclassical coupling between them. We test our formula with some numerical examples in Section 6.5. We discuss how the coupling formula may be generalized and applied to dissociation processes in Section 6.6. Finally, we present our conclusions in Section 6.7.

6.2 The Hamiltonian

Consider the one-dimensional Hamiltonian,

$$H_0(q,p) = \frac{p^2}{2m} + V(q) \tag{6.3}$$

We assume that V has the following properties: (1) $\lim_{q\to-\infty} V(q) = \infty$. (2) $\lim_{q\to\infty} V(q) = V_0$. (3) V attains its global minimum at some q_{min}, and is monotone decreasing for $q < q_{min}$ and monotone increasing for $q > q_{min}$.

The Morse oscillator ($V(q) = D(1 - e^{-\beta x})^2$) is a good example of such a system. Such a Hamiltonian admits bound states up to the dissociation energy V_0, and outgoing states above V_0. Below V_0, we may assume that the bound-states are given by quantum numbers $\{n\}$, corresponding to actions $I_n = 2\pi\hbar(n + \frac{1}{2})$, according to WKB theory in one dimension. Above V_0, the Hamiltonian admits outgoing states for all energies $E > V_0$.

Suppose we add a perturbative potential $V^{(1)}(q)$ which can induce couplings between the eigenstates. Our goal is to write down a semiclassical expression for $\langle E|\hat{V}^{(1)}|n\rangle$, where $|E\rangle$ denotes an outgoing state, and $|n\rangle$ denotes a bound state. To do this, we must first write down a semiclassical expression for the bound and unbound wavefunctions.

6.3 The Energy-Time Representation

A representation which is ideally suited to the Hamiltonian H_0 is the energy-time representation. In this canonical basis, the canonical momentum is given by the energy $E = H_0(q,p)$, and the canonical position is the transit time from the inner turning point at energy E to (q,p). If we define $t(E)$ to be the time it takes a trajectory to go from the inner turning point to the outer turning point at energy E, then any point on the $H_0(q,p) = E$ phase-space contour may be uniquely characterized by some $t \in [-t(E), t(E)]$. Because $(\pm t, E)$ represents some $(q, \pm p)$, it follows that in the energy-time representation of $V^{(1)}(q)$ we have $V^{(1)}(t,E) = V^{(1)}(-t,E)$.

The generating function from the (q,p) system to the (t,E) system is given via,

$$S(q,E) = \int_{q^-(E)}^{q} p(q',E)dq' \tag{6.4}$$

where $q^-(E)$ denotes the inner turning point at energy E, and p denotes the momentum, given by $p(q,E) = \sqrt{2m(E-V(q))}$. The conversion from the (q,p) to the (t,E) representation may be obtained from the equations [27],

$$p(q,E) = \frac{\partial S}{\partial q}(q,E) \tag{6.5}$$

$$t(q,E) = \frac{\partial S}{\partial E}(q,E) \tag{6.6}$$

It may be simply shown that $t(q,E)$ is the time it takes for a particle starting at the inner turning point at energy E to reach the point q. In contrast to the (ϕ, I) representation, the (t,E) representation can be used to represent both the bound and unbound eigenfunctions of H_0. The WKB wavefunctions are real and may be given by,

$$\psi_E(q) = A(E)\sqrt{\Big|\frac{\partial^2 S}{\partial q \partial E}\Big|}\,(\exp[iS(q,E)/\hbar] + \exp[-iS(q,E)/\hbar]) \tag{6.7}$$

where $A(E)$ is some normalization constant which we now determine. In reality, this formula breaks down near the turning points. However, in the semiclassical limit we will assume (as with the analogous derivations for the case of action-angle representations) that only contributions from the classically allowed region are important, in which case the above formula holds.

If $E < V_0$, then $E = E(n) = H_0(I_n)$, and we want the normalization $\langle n'|n\rangle = \delta_{nn'}$. Without loss of generality we may assume that $E_n < E_{n'}$. Thus, we obtain,

$$\delta_{nn'} \approx |A_n \bar{A}_{n'}| \int_{q_n^-}^{q_n^+} dq' \Big|\frac{\partial^2 S}{\partial q' \partial E}\Big|\,(e^{i(S(q',E_{n'})-S(q',E_n))/\hbar} + e^{-i(S(q',E_{n'})-S(q',E_n))/\hbar}) \tag{6.8}$$

since we are neglecting the classically forbidden region. Note that we also neglect the terms involving $S(q', E_n)+S(q', E_{n'})$. In the semiclassical limit we assume that $\hbar$ is small, so the corresponding exponentials oscillate sufficiently rapidly that the integrals are essentially 0. By the same argument, we need only consider $S(q', E_{n'}) - S(q', E_n)$ for $E_{n'} \approx E_n$. We thus make a linear approximation about E_n, to get,

$$\delta_{nn'} \approx |A_n|^2 \int_{q_n^-}^{q_n^+} dq' \left| \frac{\partial^2 S}{\partial q' \partial E} \right| (e^{i\frac{\partial S}{\partial E}\Big|_{E_n}(E_{n'}-E_n)/\hbar} + e^{-i\frac{\partial S}{\partial E}\Big|_{E_n}(E_{n'}-E_n)/\hbar}) \tag{6.9}$$

Now, using $t = \frac{\partial S}{\partial E}$, we get that $dt = |\frac{\partial^2 S}{\partial q \partial E}| dq$ at constant E. Since we are considering the turning points at energy E_n, then changing variables from (q, p) to (t, E) gives,

$$\begin{aligned} \delta_{nn'} &= |A_n|^2 (\int_0^{t_n} dt' e^{i(E_{n'}-E_n)t'/\hbar} + \int_0^{t_n} dt' e^{-i(E_{n'}-E_n)t'/\hbar}) \\ &= |A_n|^2 \int_{-t_n}^{t_n} dt' e^{i(E_{n'}-E_n)t'/\hbar} \end{aligned} \tag{6.10}$$

Now, since we are in the bound regime, $E_n = E(I_n)$, where $I_n = 2\pi\hbar(n + \frac{1}{2})$ is the action. At energy E_n, or equivalently, at action I_n, we have $\phi = \nu(I)t$, where $\nu(I) \equiv \frac{dE}{dI}$. Again, since $E_{n'} \approx E_n$, we obtain,

$$\delta_{nn'} = \frac{|A_n|^2}{\nu(I_n)} \int_{-\frac{1}{2}}^{\frac{1}{2}} d\phi e^{2\pi i(n-n')}$$

$$= \frac{|A_n|^2}{\nu(I_n)}\delta_{nn'} \tag{6.11}$$

so we obtain $A_n = \sqrt{\nu(I_n)}$.

This takes care of the bound state normalization. For the outgoing states, we want $\langle E'|E\rangle = \delta(E - E')$. We can follow a similar procedure as above, remembering that in the unbound regime, t can go to ∞, giving,

$$\begin{aligned} \delta(E - E') &= |A(E)|^2 \int_{-\infty}^{\infty} dt e^{i(E'-E)t/\hbar} \\ &= 2\pi\hbar|A(E)|^2\delta(E - E') \end{aligned} \tag{6.12}$$

giving, $A(E) = \frac{1}{\sqrt{2\pi\hbar}}$.

6.4 The Coupling Formula

We now wish to evaluate the semiclassical coupling $\langle E|\hat{V}^{(1)}|n\rangle$ between the bound state $|n\rangle$ and the outgoing state $|E\rangle$. Following the derivation for the bound-bound couplings, we assume that $E \approx E_n$. Consider, then, some energy $E_m \in [E_n, E]$. We can then write $S(q, E) - S(q, E_n) \approx \frac{\partial S}{\partial E}\Big|_{E_m}(E - E_n)$.

Then we integrate from $q^-(E_m)$ to $q^+(E_m)$, where $q^+(E_m)$ may very well

be ∞ if $E_m > V_0$. The semiclassical coupling is then,

$$\begin{aligned}
\langle E|\hat{V}^{(1)}|n\rangle &= \sqrt{\frac{\nu(I_n)}{2\pi\hbar}}\int_{q^-(E_m)}^{q^+(E_m)} dq' V^{(1)}(q') \Big| \Big(\frac{\partial^2 S}{\partial q' \partial E}\Big|_{E_m}\Big)\Big| \times \\
&\quad \Big(e^{i\frac{\partial S}{\partial E}\Big|_{E_m}(E-E_n)/\hbar} + e^{-i\frac{\partial S}{\partial E}\Big|_{E_m}(E-E_n)/\hbar}\Big) \\
&= \sqrt{\frac{\nu(I_n)}{2\pi\hbar}}\int_0^{t(E_m)} dt V^{(1)}(t,E_m)\big(e^{i(E-E_n)t/\hbar} + e^{-i(E-E_n)t/\hbar}\big) \\
&= \sqrt{\frac{\nu(I_n)}{2\pi\hbar}}\int_{-t(E_m)}^{t(E_m)} dt V^{(1)}(t,E_m) e^{-i(E-E_n)t/\hbar} \\
&= \sqrt{\frac{\nu(I_n)}{2\pi\hbar}}\tilde{V}^{(1)}_{\frac{E-E_n}{2\pi\hbar}}(E_m) \qquad (6.13)
\end{aligned}$$

where $\tilde{V}_k^{(1)}(E) \equiv \int_{-t(E)}^{t(E)} dt V^{(1)}(t,E) e^{-2\pi i k t}$. Thus, we have developed an expression for the bound-free coupling in terms of the Fourier coefficients of $V^{(1)}$ in the energy-time basis.

6.5 Numerical Tests

We tested our coupling formula numerically for the zeroth-order Hamiltonian,

$$H_0(q,p) = \frac{p^2}{2\mu} + D(1-e^{-\beta q})^2 \qquad (6.14)$$

using $V^{(1)}(q) = e^{-\alpha q^2}$. H_0 has a zeroth-order harmonic frequency ω_0 given by $\frac{1}{2}\mu\omega_0^2 = D\beta^2$. We took $\mu = 1.0$, $\omega_0 = 1.0$, $D = 10.0$ and $\hbar = 1.0$. This Hamiltonian supports 20 bound states, with energies given by, $E_n = (n+\frac{1}{2})\hbar\omega_0(1 - \frac{(n+\frac{1}{2})\hbar\omega_0}{4D})$, where $n = 0, 1, 2, \ldots, 19$.

Figures 6.1-4 plot the couplings between all the bound-states to the outgoing state with energy $E = 11.0$, for $\alpha = 0.01$, 0.1, 1.0, and 10.0, respectively. Three values of E_m were used: $E_m = E_n$, the energy of the bound-state, $E_m = E$, the energy of the outgoing state, and $E_m = \frac{E_n+E}{2}$, the energy midway between the two states. It should be noted the the absolute value of the coupling is being plotted, for two reasons. First, this avoids any ambiguities associated with differences in wavefunction sign. Second, the bound-free dissociative dynamics is generally a Fermi Golden Rule (FGR) decay out of a bound state into a manifold of outgoing states with energy close to the bound-state energy. Thus, the relevant parameter is the absolute value of the coupling squared, so the sign and any phase factors are unimportant.

We may note for all four graphs, that, as the quantum number increases, the semiclassical couplings all converge on the quantum result, which is to be expected, since at higher energy the semiclassical approximation, as well as the linearization of the generating function S, become more accurate. Nevertheless, we may note that certain choices for E_m are better than others depending on the potential. For $\alpha = 0.01$, the $E_m = E$ graph ("SC Free") is quantitative over the entire range of bound-states. The $E_m = \frac{E_n+E}{2}$ graph ("SC Middle") only becomes quantitative for bound-states with quantum

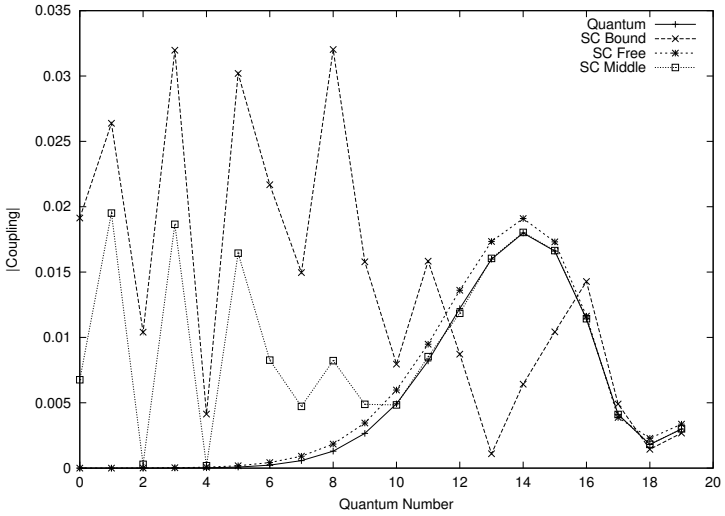

Figure 6.1: Quantum versus semiclassical couplings for $\alpha = 0.01$.

numbers around 10 or higher. The $E_m = E_n$ graph ("SC Bound") takes the longest to become quantitative, at a quantum number of 16.

For $\alpha = 0.1$, all graphs remain fairly quantitative, except for $E_m = E_n$ for $n \in [0, 4]$. The best fit is for $E_m = \frac{E_n + E}{2}$, which is essentially indistinguishable from the quantum result.

A similar pattern persists for $\alpha = 1.0$, though this time the "SC Bound" and "SC Free" graphs take somewhat longer to become quantitative than previously. Nevertheless, the "SC Middle" graph remains quantitative for all quantum numbers.

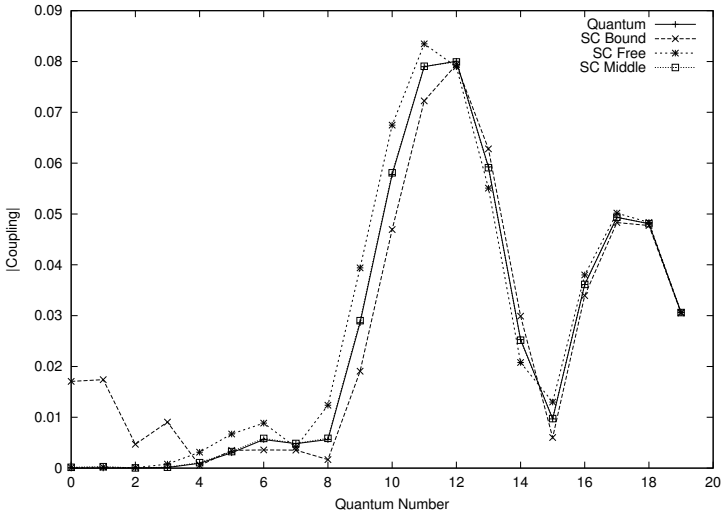

Figure 6.2: Quantum versus semiclassical couplings for $\alpha = 0.1$.

Finally, for $\alpha = 10.0$, we see that all three semiclassical graphs become quantitative around $n = 5$, though once again it appears that the "SC Middle" graph is more accurate than the rest.

There are several patterns to note here. First of all, of the three prescriptions for choosing E_m, the choice $E_m = \frac{E_n+E}{2}$ was the most accurate, with the notable exception for $\alpha = 0.01$, for which $E_m = E$ was the most accurate. Both results are easy to explain. In general, using $E_m = \frac{E_n+E}{2}$ should be more accurate than using $E_m = E_n$ or E, because the expression $S(q, E) - S(q, E_n) = \frac{\partial S}{\partial E}(q, E_m)(E - E_n)$ is accurate to third-order in $E - E_n$

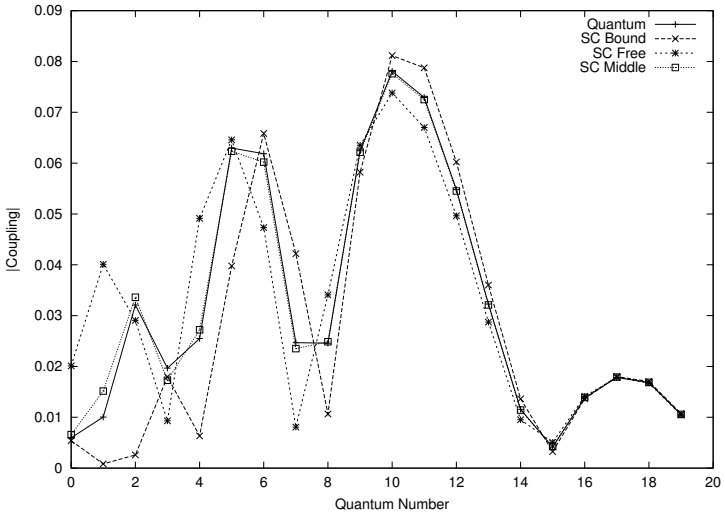

Figure 6.3: Quantum versus semiclassical couplings for $\alpha = 1.0$.

for $E_m = \frac{E_n+E}{2}$, but only accurate to second-order in $E - E_n$ for $E_m = E_n, E$. In the case of $\alpha = 0.01$, however, the potential is sufficiently spread out that using $E_m = E_n, \frac{E+E_n}{2}$ results in integration over too narrow a range for the lower quantum numbers to accurately capture all the coupling. Because for $E_m = E$ the integration range is infinite, it captures the whole potential, leading to a more accurate expression for the coupling.

Finally, while the semiclassical coupling graphs for $\alpha = 0.01, 0.1, 1.0$ become essentially indistinguishable from the quantum results for the higher quantum numbers, a small discrepancy persists for $\alpha = 10.0$ all the way up

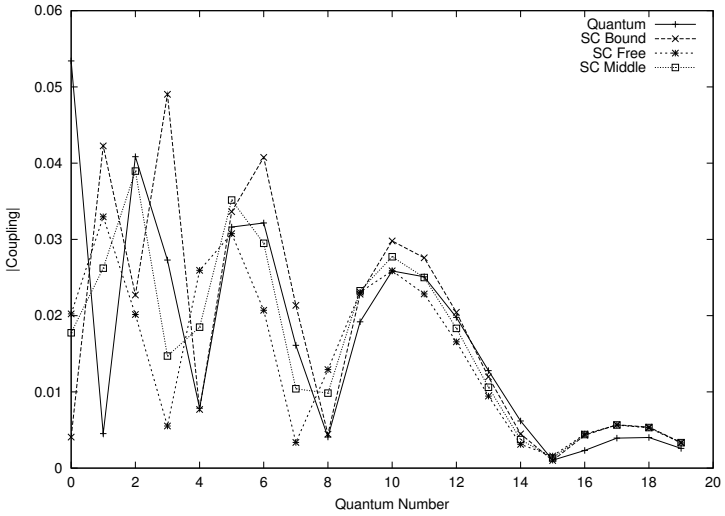

Figure 6.4: Quantum versus semiclassical couplings for $\alpha = 10.0$.

to $n = 19$. The reason for this is that the potential at this point is so narrow that the effective integration range for the coupling is fairly narrow. However, semiclassical approaches are expected to be accurate in regimes where $\hbar$ is small, or equivalently, when the characteristic wavelength is short compared to the length scales of the problem. In this case, the potential is so sharp that the effective range of the potential is on the order of a wavelength or less, leading to observable (though small) discrepancies between the quantum and semiclassical result.

6.6 Application to Dissociation Processes

While the bound-free semiclassical formula was developed for one-dimensional systems, the generalization to separable systems is immediate. Specifically, given a D degree-of-freedom Hamiltonian,

$$H_0(q_1,\ldots,q_D,p_1,\ldots,p_D) = \sum_{i=1}^{D}(\frac{p_i^2}{2\mu_i} + V_i(q_i)) \tag{6.15}$$

which produces an energy-time representation of phase-space given by $(t_1,\ldots,t_D,E_1,\ldots,E_D)$, then given some potential $V^{(1)}(q_1,\ldots,q_D)$ we obtain the semiclassical result,

$$\langle E_1,\ldots E_D|\hat{V}^{(1)}|n_1,\ldots,n_D\rangle = (2\pi\hbar)^{-\frac{D}{2}}\sqrt{\Pi_{i=1}^{D}\nu(I_{n_i})}\tilde{V}^{(1)}_{\frac{\mathbf{E}-\mathbf{E_n}}{2\pi\hbar}}(\mathbf{E_m}) \tag{6.16}$$

where $\mathbf{E} \equiv (E_1,\ldots,E_D)$, $\mathbf{E_n} \equiv (E_{n_1},\ldots,E_{n_D})$, and $\mathbf{E_m} \equiv (E_{m_1},\ldots,E_{m_D})$.

For non-separable systems, the formula is in principle the same, as long as it is possible to find a canonical representation of the phase space which can be used to construct the semiclassical basis functions in both the bound and unbound regimes.

Our one-dimensional coupling formula, as written, does not explicitly give the bound-free coupling for a dissociative process, because the formula couples two states of differing energies. As mentioned previously, dissociative

processes typically involve a Fermi Golden Rule decay from a bound-state to an unbound-state of equal energy. However, to illustrate how the semiclassical bound-free formula may be applied to dissociation, consider the simplest case of a two-dimensional dissociative process from some bound state $|v\rangle|E_n\rangle$ to an unbound state $|v-1\rangle|E\rangle$. This process corresponds to a vibrational predissociation process, where one quantum of vibration (the "v" states) is transferred to a translational degree of freedom, with sufficient energy to cause dissociation. If we assume that bound states have the $\delta_{nn'}$ normalization, and unbound states have the $\delta(E-E')$ normalization, then if V denotes the perturbation leading to dissociation, then the dissociative coupling is given semiclassically by,

$$\langle v-1, E|\hat{V}|v, E_n\rangle = \sqrt{\frac{\nu(I_n)}{2\pi\hbar}}\tilde{V}_{(-1,\frac{E-E_n}{2\pi\hbar})}(2\pi\hbar v, E_m) \tag{6.17}$$

Here $\tilde{V}$ denotes the Fourier expansion of V, where the vibrational coordinates are expanded in action-angle variables, and the translational coordinates are expanded in an energy-time representation. $\nu(I_n)$ denotes the zeroth-order frequency for the translational motion in the bound-state with quantum number n.

The type of vibrational predissociation process described above is known

as "T-shaped" predissociation, as it does not include rotational effects. Thus, what we have presented is a simplification of the true predissociation dynamics. Nevertheless, the purpose is to give a concrete example, illustrating how the bound-free semiclassical coupling formula may be applied to actual systems.

6.7 Conclusions

This chapter presented a semiclassical approach for computing the bound-free couplings for one-dimensional systems using classical Fourier coefficients. The result is a partial generalization of the formula for bound-bound couplings. The key difference is that while the bound-bound couplings are generally given as Fourier coefficients from an action-angle representation of the Hamiltonian, in the bound-free case the Fourier coefficients come from an energy-time representation of the Hamiltonian. Such a representation is valid in both the bound and unbound regimes, though the range of the time variable is energy-dependent (in contrast to action-angle variables, for which the range of the angle variable is an interval of length 1). Numerical tests for several potentials confirmed the semiclassical formula.

The bound-free semiclassical coupling formula could prove useful in analyzing dissociation processes such as the vibrational predissociation of van der Waals complexes. Because the semiclassical couplings are obtained from Fourier coefficients of a classical Hamiltonian, they are in general easier to compute than the quantum couplings, which would require the numerical integration of wavefunctions.

Appendix A

Numerically Stable Implementation of the GDA Method

A.1 Propagating H One Time Step

In this section, we describe how we numerically integrate the PDE for H (as presented in Chapter 2) one time step forward. First of all, it should be noted that since we are considering all terms of the form $\mathbf{k} \cdot \nabla_{\mathbf{I}} H_0$, we are simultaneously evolving potential terms corresponding to resonances and

fast terms. Thus, there is a variety of time scales in our system, so that stiffness becomes a problem. One way around this is to employ an implicit integration scheme to achieve stability, but we have a different method which takes advantage of the fact that our perturbation is small.

The first-order approximation to our evolution equation was shown to be $\frac{\partial H_n}{\partial t} = -(\mathbf{n}\cdot\nabla_{\mathbf{I}}H_0)^2 H_n$, giving $H_n(\mathbf{I}, t+\tau) = H_n(\mathbf{I}, t)e^{-(\mathbf{n}\cdot\nabla_{\mathbf{I}}H_0)^2\tau}$. Therefore, for small τ we may write,

$$\begin{aligned}\frac{\partial H_n(\mathbf{I}, t+\tau)}{\partial \tau} &= -\sum_{\mathbf{k}\neq\mathbf{0}}[(\mathbf{k}\cdot\nabla_{\mathbf{I}}H_{\mathbf{n}-\mathbf{k}}(\mathbf{I}, t))H_k(\mathbf{I}, t) - \\ &\quad ((\mathbf{n}-\mathbf{k})\cdot\nabla_{\mathbf{I}}H_k(\mathbf{I}, t))H_{\mathbf{n}-\mathbf{k}}(\mathbf{I}, t)] \times \\ &\quad (\mathbf{k}\cdot\nabla_{\mathbf{I}}H_0)e^{-((\mathbf{k}\cdot\nabla_{\mathbf{I}}H_0)^2+((\mathbf{n}-\mathbf{k})\cdot\nabla_{\mathbf{I}}H_0)^2)\tau} \qquad \text{(A.1)}\end{aligned}$$

so integrating τ from 0 to DT gives,

$$\begin{aligned}H_n(\mathbf{I}, t+DT) &= H_n(\mathbf{I}, t) - \sum_{\mathbf{k}\neq\mathbf{0}}(1 - e^{-((\mathbf{k}\cdot\nabla_{\mathbf{I}}H_0)^2+((\mathbf{n}-\mathbf{k})\cdot\nabla_{\mathbf{I}}H_0)^2)DT})(\mathbf{k}\cdot\nabla_{\mathbf{I}}H_0) \times \\ &\quad \frac{(\mathbf{k}\cdot\nabla_{\mathbf{I}}H_{\mathbf{n}-\mathbf{k}}(\mathbf{I}, t))H_k(\mathbf{I}, t) - ((\mathbf{n}-\mathbf{k})\cdot\nabla_{\mathbf{I}}H_k(\mathbf{I}, t))H_{\mathbf{n}-\mathbf{k}}(\mathbf{I}, t)}{(\mathbf{k}\cdot\nabla_{\mathbf{I}}H_0)^2 + ((\mathbf{n}-\mathbf{k})\cdot\nabla_{\mathbf{I}}H_0)^2} \qquad \text{(A.2)}\end{aligned}$$

Of course, if $\alpha \equiv (\mathbf{k}\cdot\nabla_{\mathbf{I}}H_0)^2 + ((\mathbf{n}-\mathbf{k})\cdot\nabla_{\mathbf{I}}H_0)^2$ is too close to 0, then the computer will give a floating exception error if we try to evaluate $\frac{1-e^{-\alpha DT}}{\alpha}$ directly. We thus evaluate this term as follows: We define $x = \alpha DT$, and

rewrite our expression as $DT\frac{1-e^{-x}}{x}$. We then evaluate $\frac{1-e^{-x}}{x}$ via its Taylor expansion, given by $\sum_{n=0}^{\infty}\frac{(-x)^n}{(n+1)!}$.

By expanding the exponential out to first-order, we see that this approach reduces to the ordinary one-step explicit Euler method for sufficiently small DT. However, the above method is superior to using an explicit Euler method since we can now take larger time steps more appropriate to the slow terms arising from resonances or near-resonances. These larger time steps do not lead to numerical instability, since the more non-resonant terms (corresponding to the shorter time scales requiring smaller time steps to maintain stability in the explicit Euler scheme) are attentuated by the exponential factor. In fact, since we want to kill off the non-resonant terms in any case, there is an optimum time step which kills off the non-resonant terms as much as possible without sacrificing accuracy.

A.2 Numerical Propagation of S

If H is given analytically, then the derivatives of H can also be determined analytically. Therefore, it can be seen from Eqs. (1.37) and (1.38) that the numerical propagation of S only requires the numerical evaluation of the

partial derivatives of S. This is done using centered differences.

At time $t = 0$, S is simply the identity transformation, so that $S(\mathbf{q}, \mathbf{P}; 0) = \mathbf{q} \cdot \mathbf{P}$. Thus, S is not periodic in each q_i with period L_i. Define $\mathbf{nL} = (n_1 L_1, \ldots, n_D L_D)$, and note, however, that $S(\mathbf{q} + \mathbf{nL}, \mathbf{P}; 0) = \mathbf{P} \cdot \mathbf{nL} + S(\mathbf{q}, \mathbf{P}; 0)$. We claim that this property is preserved by the evolution. We shall assume this for what follows, and then prove it at the end of this section. Thus, although S is not periodic in the q_i's, we still need only track S for $\mathbf{q}$ in a D-dimensional box of side lengths $L_1, \ldots, L_D$.

The $\mathbf{q}$-grid is given by $\{(n_1 L_1/N, \ldots, n_D L_D/N) | n_i = 0, \ldots, N-1\}$, giving N^D grid points. We track all $\mathbf{P}$ on a grid of canonical momenta about some central momentum $\mathbf{P}_0$, where our grid consists of all canonical momenta $\mathbf{P_k} = \mathbf{P}_0 + DX\mathbf{k}$, with $\mathbf{k} = (k_1, \ldots, k_D)$ satisfying $|k_1| + \ldots + |k_D| \leq GDSZ$. Let us denote this set by $\Omega(\mathbf{P}_0, GDSZ)$. Since our evolution involves a first-derivative in $\mathbf{P}$ of S, we cannot compute $\frac{\partial S}{\partial t}$ at the boundary of the $\mathbf{P}$-grid. The result is that we can only propagate on $\Omega(\mathbf{P}_0, GDSZ - 1)$, so that at each iteration the value of $GDSZ$ shrinks by 1. This collapsing boundary method is described in further detail in Ref. 2, since it also arises naturally in the numerical implementation of the H evolution. The absence of any boundary condition for the $\mathbf{P}$-grid is due to the fact that there are simply no

physically natural boundary conditions to impose. This is in contrast to the heat equation, for example, where fixing the temperature at the boundary is physically realized by immersing the system in a constant temperature bath.

Once $\frac{\partial S}{\partial t}$ has been evaluated on all possible grid points, the propagation by some time step DT is done using the Explicit Euler method, which means that we set $S(\mathbf{q}, \mathbf{P}_k; t + DT) = S(\mathbf{q}, \mathbf{P}_k; t) + DT \frac{\partial S}{\partial t}(\mathbf{q}, \mathbf{P}_k; t)$.

Finally, suppose we are considering a system with unbound degrees of freedom, that is, some of the $L_i = 0$. Then we track those $q_i \in \{q_{i0} \pm n\Delta | n = 0, \ldots, N_i\}$. At each time step, we can only compute $\frac{\partial S}{\partial t}$ up to $n = N_i - 1$, so that after each time step we shrink our set of q_i by decreasing N_i by one. While in this case it may be possible to impose more natural boundary conditions on the system, in practice it is numerically most stable to have a free boundary, as is done with the $\mathbf{P}$-grid.

We will now prove that $S(\mathbf{q} + \mathbf{nL}, \mathbf{P}; t) = \mathbf{P} \cdot \mathbf{nL} + S(\mathbf{q}, \mathbf{P}; t)$. To do this, we make the key assumption that the numerical propagation outlined above converges to the exact solution of the PDE in the limit of the time and spatial steps approaching 0. Specifically, given some time $T > 0$ to which we wish to propagate the PDE, we divide the time grid into step sizes of length $DT = T/N$, where N is an integer that we let go to ∞. At

some $\mathbf{q}, \mathbf{P}$, we construct $S(\mathbf{q}, \mathbf{P}; t)$ by constructing $S_n(\mathbf{q}, \mathbf{P}) \equiv S(\mathbf{q}, \mathbf{P}; nDT)$, where $n = 0, \ldots, N$, and for $t \in [0, T]$ we define $S(\mathbf{q}, \mathbf{P}; t)$ to be the linear interpolation of $(S_0(\mathbf{q}, \mathbf{P}), \ldots, S_N(\mathbf{q}, \mathbf{P}))$ on $[0, T]$. Clearly, if we can show that $S_n(\mathbf{q} + \mathbf{nL}, \mathbf{P}) = \mathbf{P} \cdot \mathbf{nL} + S_n(\mathbf{q}, \mathbf{P})$, then by interpolation our claim holds $\forall t \in [0, T]$. We prove this by induction.

By definition, $S_n(\mathbf{q} + \mathbf{nL}, \mathbf{P}) = \mathbf{P} \cdot \mathbf{nL} + S_n(\mathbf{q}, \mathbf{P})$ for $n = 0$, so assume the result holds for some $n \geq 0$. To prove that it holds for $n + 1$, we may note that,

$$\begin{aligned} S_{n+1}(\mathbf{q} + \mathbf{nL}, \mathbf{P}) &= S_n(\mathbf{q} + \mathbf{nL}, \mathbf{P}) + \frac{\partial S}{\partial t}(\mathbf{q} + \mathbf{nL}, \mathbf{P}; nDT)DT \\ &= \mathbf{P} \cdot \mathbf{nL} + S_n(\mathbf{q}, \mathbf{P}) + \frac{\partial S}{\partial t}(\mathbf{q} + \mathbf{nL}, \mathbf{P}; nDT)DT \end{aligned} \tag{A.3}$$

Now, from $S_n(\mathbf{q} + \mathbf{nL}, \mathbf{P}) = \mathbf{P} \cdot \mathbf{nL} + S_n(\mathbf{q}, \mathbf{P})$ we obtain that $\frac{\partial S}{\partial \mathbf{P}}(\mathbf{q} + \mathbf{nL}, \mathbf{P}; nDT) = \mathbf{nL} + \frac{\partial S}{\partial \mathbf{P}}(\mathbf{q}, \mathbf{P}; nDT)$, so the periodicity of G then implies that $\frac{\partial S}{\partial t}(\mathbf{q} + \mathbf{nL}, \mathbf{P}; nDT) = \frac{\partial S}{\partial t}(\mathbf{q}, \mathbf{P}; nDT)$. Then Eq. (A.3) becomes,

$$\begin{aligned} S_{n+1}(\mathbf{q} + \mathbf{nL}, \mathbf{P}) &= \mathbf{P} \cdot \mathbf{nL} + S_n(\mathbf{q}, \mathbf{P}) + \frac{\partial S}{\partial t}(\mathbf{q}, \mathbf{P}; nDT)DT \\ &= \mathbf{P} \cdot \mathbf{nL} + S_{n+1}(\mathbf{q}, \mathbf{P}) \end{aligned} \tag{A.4}$$

thereby completing the induction step, and proving our claim.

A.3 Propagation Time

Recall from Eq. (1.30) that the first-order expression for the evolution of H in Fourier space is,

$$\frac{\partial H_{\mathbf{k}}}{\partial t} = 2\pi i(\mathbf{k} \cdot \nabla_{\mathbf{P}} H^{(0)}) G_{\mathbf{k}} \tag{A.5}$$

This equation was then used to obtain the gradient-descent prescription for choosing G in the first-order limit. For weak perturbations, this prescription no longer coincides with the gradient-descent approach, but should still shrink the nonzero Fourier components of H. This will occur as long as the right side of Eq. (A.5) (or Eq. (1.30)) is sufficiently dominant compared to the remaining terms in the full PDE for H. Note then that for resonances and near-resonances this condition does not hold. However, for sufficiently non-resonant terms this condition does hold. Thus, in general, for a weak perturbation, our PDE-based approach starts out by decreasing the more non-resonant terms of H. The $\mathbf{Q}$-dependence of H starts decreasing, and so the rate of change of S decreases as well as the evolution proceeds. Eventually, the sufficiently non-resonant terms of H are reduced to a point where higher-order terms become important, so that our first-order gradient-descent prescription for choosing G will no longer work to reduce the $\mathbf{Q}$-dependence

of H. The rate of change of S then begins to increase after this point, and eventually the PDE becomes numerically unstable. By tracking $\sqrt{\langle(\partial S/\partial t)^2\rangle}$ on the grid, it is possible to stop the evolution where the rate of change of S reaches its minimum, and consequently where the canonical basis has been optimized. The H evolution is also terminated using an analogous criterion to the one used for S.

Of course, the weaker the perturbation, the closer a given $\mathbf{k}$ must be to a resonance for our choice of G to no longer work to reduce the corresponding $H_{\mathbf{k}}$. Futhermore, the weaker the perturbation, the longer it is possible to propagate the PDE before $\sqrt{\langle(\partial S/\partial t)^2\rangle}$ reaches its minimum, and the closer this minimum will correspond to a steady-state. It would be interesting to develop a simple criterion to estimate at what time this minimum occurs, and how far away the system is from steady-state at the minimum.

Appendix B

An Additional First-Order Result

In this section we derive the first-order result for $H(\mathbf{q}, \frac{\partial S}{\partial \mathbf{q}}; 0)$. Following the procedure in Chapter 1, we write $S = \mathbf{q} \cdot \mathbf{P} + \tilde{G}(\mathbf{q}, \mathbf{P}; t)$. We also write $H(\mathbf{q}, \mathbf{p}; 0) = H^{(0)}(\mathbf{p}; 0) + H^{(1)}(\mathbf{q}, \mathbf{p}; 0)$. Using $\mathbf{p} = \frac{\partial S}{\partial \mathbf{q}} = \mathbf{P} + \nabla_{\mathbf{q}} \tilde{G}(\mathbf{q}, \mathbf{P}; t)$, we get to first-order that,

$$H(\mathbf{q}, \mathbf{p}; 0) = H^{(0)}(\mathbf{P}; 0) + \nabla_{\mathbf{P}} H^{(0)}(\mathbf{P}; 0) \cdot \nabla_{\mathbf{q}} \tilde{G}(\mathbf{q}, \mathbf{P}; t) + H^{(1)}(\mathbf{q}, \mathbf{P}; 0) \quad \text{(B.1)}$$

For simplicity, we assume that G was chosen using $H^{(0)}(\mathbf{P}) = H^{(0)}(\mathbf{P}; 0)$. As mentioned before, in the first-order limit all three prescriptions for choosing

G are equivalent. Using the other two prescriptions will lead to at most second-order corrections in our final result. From Eq. (1.45) we get that,

$$\begin{aligned}\nabla_{\mathbf{P}} H^{(0)} \cdot \nabla_{\mathbf{q}} \tilde{G}(\mathbf{q}, \mathbf{P}; t) &= -\frac{1}{V} \sum_{\mathbf{k} \neq 0} H_{\mathbf{k}}^{(1)} (1 - e^{-4\pi^2 (\mathbf{k} \cdot \nabla_{\mathbf{P}} H^{(0)})^2 t}) e^{2\pi i \mathbf{k} \cdot \mathbf{q}} \\ &= -H^{(1)} + \frac{1}{V} \sum_{\mathbf{k} \neq 0} H_{\mathbf{k}}^{(1)} e^{-4\pi^2 (\mathbf{k} \cdot \nabla_{\mathbf{P}} H^{(0)})^2 t} e^{2\pi i \mathbf{k} \cdot \mathbf{q}}\end{aligned} \tag{B.2}$$

and so we obtain,

$$H(\mathbf{q}, \frac{\partial S}{\partial \mathbf{q}}(\mathbf{q}, \mathbf{P}; t); 0) = H^{(0)}(\mathbf{P}; 0) + \frac{1}{V} \sum_{\mathbf{k} \neq 0} H_{\mathbf{k}}^{(1)}(\mathbf{P}; 0) e^{-4\pi^2 (\mathbf{k} \cdot \nabla_{\mathbf{P}} H^{(0)})^2 t} e^{2\pi i \mathbf{k} \cdot \mathbf{q}} \tag{B.3}$$

Appendix C

Numerical Details for the Vibrational Predissociation Calculations

In this Appendix, we present some numerical details for the calculations in Chapter 5. These calculations were not regarded as sufficiently interesting to be included in the main body of the chapter. They are included here to aid interested researchers in reproducing our results and possibly refining and extending the predissociation model.

C.1 The Free-HF Basis

The rovibrational states of HF were obtained by assuming a Morse interaction potential, with a ground-state harmonic frequency $\omega = 4138.32$ cm^{-1}, and a dissociation energy of $D = 47,628$ cm^{-1}. We obtained our free-HF eigenfunctions for $v = 0 - 4$, $j = 0 - 14$. The equilibrium bond length r_{eq} of HF is also known and is equal to 0.9168 Å. The actual free-HF energies differ slightly from those obtained using the Morse potential approximation. An excellent fit, accurate to within 1 cm^{-1}, is given by the Dunham expression [60],

$$\begin{aligned} E_{vj} &= (Y_{10}(v+\frac{1}{2}) + Y_{20}(v+\frac{1}{2})^2 + Y_{30}(v+\frac{1}{2})^3) + \\ &\quad (Y_{01} + Y_{11}(v+\frac{1}{2}) + Y_{21}(v+\frac{1}{2})^2)j(j+1) + \\ &\quad (Y_{02} + Y_{12}(v+\frac{1}{2}) + Y_{22}(v+\frac{1}{2})^2)(j(j+1))^2 \end{aligned} \tag{C.1}$$

where $Y_{10} = 4138.32, Y_{20} = -89.88, Y_{30} = 0.90, Y_{01} = 20.9557, Y_{11} = -0.798, Y_{21} = 0.0127, Y_{02} = 0.002151, Y_{12} = -6.8 \times 10^{-5}, Y_{22} = 2.8 \times 10^{-6}$, all in units of cm^{-1}.

Because the corrections to the free-HF energies computed with the Morse potential are small (at most a few percent), we decided that the free-HF eigenfunctions computed from the Morse potential were sufficiently accurate

for the calculations in Chapter 5. However, since a highly accurate expression for the free-HF spectrum is available, we decided to use it to compute the free-HF energies once our Morse potential calculations converged.

C.2 Potential Couplings

To determine the representation at a given R of $V(R, r, \theta)$ in the free-HF basis, we start by writing the free-HF states $|v, j\rangle$ as $\sum_k c_{vk}|k\rangle|j, m\rangle$, where $\{|k\rangle\}$ are the harmonic-oscillator eigenfunctions corresponding to the ground-state harmonic frequency of the Morse potential. Then the coupling $\langle v', j'|V|v, j\rangle$ is given by $\sum_{k,k'} c_{v'k'}c_{vk}\ \langle j', m|\langle k'|V|k\rangle|j, m\rangle$. This proved to be a convenient way to compute the couplings, since harmonic-oscillator eigenstates are relatively easy to handle.

We converted from the r representation of the HF bond length to the $\rho = r - r_{eq}$ representation in terms of equilibrium displacement. We also converted from the angle θ to $y \equiv \cos\theta - 1$. We next made the expansion $V(R, r, \theta) = \sum_s a_s(R, \rho)y^s$. Since we have 13 data points for y for each R, r pair, we make our fit out to 12^{th} order. Then,

$$\langle j', m|V|j, m\rangle = \sum_s a_s(R, \rho)\langle j', m|y^s|j, m\rangle \tag{C.2}$$

and so,

$$\langle k'|\langle j', m|V|j, m\rangle|k\rangle = \sum_s \langle k'|a_s(R,\rho)|k\rangle\langle j', m|y^s|j, m\rangle \qquad \text{(C.3)}$$

The evaluation of $\langle j', m|y^s|j, m\rangle$ is performed analytically (with some help from MATHEMATICA). The evaluation of $\langle k'|a_s(R,\rho)|k\rangle$ is done numerically, using linear interpolation on $a_s(R,\rho)$ in ρ. While we could only perform the integration over a finite ρ range for which potential data was available, we presume that the wavefunctions decay sufficiently rapidly outside this range that such an integration yields accurate results.

Appendix D

Angular Couplings

In this Appendix, we shall show how we compute couplings of the form, $\langle j', m|y^n|j, m\rangle$, where $y \equiv \cos\theta - 1$. We start by writing,

$$\begin{aligned}\langle\theta, \phi|j, m\rangle &= Y_j^m(\theta, \phi) \\ &= \frac{(-1)^j}{2^j j!}\sqrt{\frac{2j+1}{4\pi}\frac{(j+m)!}{(j-m)!}}e^{im\phi}\frac{1}{\sin^m\theta}\frac{d^{j-m}}{d(\cos\theta)^{j-m}}(\sin\theta)^{2j}\end{aligned} \tag{D.1}$$

As explained in Chapter 5, our potential does not induce transitions between different m states. Thus, we can forget about the $e^{im\phi}$ term, and

reexpress our equation in terms of y. This gives us,

$$f_j^m(y) = \frac{1}{2^j j!}\sqrt{\frac{2j+1}{4\pi}\frac{(j+m)!}{(j-m)!}}\frac{1}{(-y(y+2))^{\frac{m}{2}}}\frac{d^{j-m}}{dy^{j-m}}(y(y+2))^j \qquad \text{(D.2)}$$

Remembering that the integration of ϕ from 0 to 2π simply produces a factor of 2π, we obtain that,

$$\begin{aligned}\langle j', m|y^n|j, m\rangle &= \frac{1}{2^{j+j'+1}j!j'!}\sqrt{(2j+1)(2j'+1)}\sqrt{\frac{(j+m)!}{(j-m)!}\frac{(j'+m)!}{(j'-m)!}} \times \\ &\int_{-2}^{0} dy \frac{y^n}{(-y(y+2))^m}\frac{d^{j-m}}{dy^{j-m}}(y(y+2))^j\frac{d^{j'-m}}{dy^{j'-m}}(y(y+2))^{j'}\end{aligned} \qquad \text{(D.3)}$$

We apply the change of variable $y = -2u$, which after some reshuffling of powers of 2, results in the equation,

$$\begin{aligned}\langle j', m|y^n|j, m\rangle &= \frac{(-1)^n 2^n}{j!j'!}\sqrt{(2j+1)(2j'+1)}\sqrt{\frac{(j+m)!}{(j-m)!}\frac{(j'+m)!}{(j'-m)!}} \times \\ &\int_0^1 du u^{n-m}(1-u)^{-m}\frac{d^{j-m}}{du^{j-m}}(u(1-u))^j\frac{d^{j'-m}}{du^{j'-m}}(u(1-u))^{j'}\end{aligned} \qquad \text{(D.4)}$$

Now, $(x+a)^j = \sum_{k=0}^{j}\binom{j}{k}x^k a^{j-k}$, so $x^j(x+a)^j = \sum_{k=0}^{j}\binom{j}{k}x^{j+k}a^{j-k}$, and hence,

$$\frac{d^{j-m}}{dx^{j-m}}(x(x+a))^j = \sum_{k=0}^{j}\binom{j}{k}(j+k)\cdots(k+m+1)x^{k+m}a^{j-k}$$

$$
\begin{aligned}
&= x^m a^j \sum_{k=0}^{j} \binom{j}{k} \frac{(j+k)!}{(k+m)!} \frac{(j-m)!}{(j-m)!} x^k a^{-k} \\
&= x^m a^j (j-m)! \sum_{k=0}^{j} \binom{j}{k} \binom{j+k}{j-m} x^k a^{-k} \qquad \text{(D.5)}
\end{aligned}
$$

Define $y = x + a$ (this y should be understood as distinct from the y defined as $\cos\theta - 1$). Then,

$$
\begin{aligned}
\frac{d^{j-m}}{dx^{j-m}}(x(x+a))^j &= \frac{d^{j-m}}{dy^{j-m}}(y(y-a))^j \\
&= y^m (-1)^j a^j (j-m)! \sum_{k=0}^{j} \binom{j}{k} \binom{j+k}{j-m} y^k (-1)^k a^{-k} \\
&= (-1)^j a^j (j-m)! (x+a)^m \sum_{k=0}^{j} \binom{j}{k} \binom{j+k}{j-m} \times \\
&\quad (-1)^k a^{-k} (x+a)^k \qquad \text{(D.6)}
\end{aligned}
$$

The sum is just,

$$
\begin{aligned}
\sum_{k=0}^{j} \binom{j}{k} \binom{j+k}{j-m} (-1)^k a^{-k} \sum_{k'=0}^{k} \binom{k}{k'} x^{k'} a^{k-k'} &= \sum_{k=0}^{j} \binom{j}{k} \binom{j+k}{j-m} (-1)^k \times \\
&\quad \sum_{k'=0}^{k} \binom{k}{k'} x^{k'} a^{-k'} \\
&= \sum_{k'=0}^{j} x^{k'} a^{-k'} \times \\
&\quad \sum_{k=k'}^{j} \binom{k}{k'} \binom{j}{k} \binom{j+k}{j-m} (-1)^k \\
&= \sum_{k=0}^{j} x^k a^{-k} \times \\
&\quad \sum_{k'=k}^{j} \binom{k'}{k} \binom{j}{k'} \binom{j+k'}{j-m} (-1)^{k'}
\end{aligned}
$$

(D.7)

Now, $\binom{k'}{k}\binom{j}{k'} = \frac{k'!}{k!(k'-k)!}\frac{j!}{k'!(j-k')!} = \frac{j!}{k!(j-k)!}\frac{(j-k)!}{(j-k')!(k'-k)!} = \binom{j}{k}\binom{j-k}{j-k'}$, so we get, $\sum_{k=0}^{j}\binom{j}{k}x^k a^{-k}\sum_{k'=k}^{j}\binom{j-k}{j-k'}\binom{j+k'}{j-m}(-1)^{k'}$. This has a root of multiplicity m at $x=0$, so this is just,

$$\sum_{k=m}^{j}\binom{j}{k}x^k a^{-k}\sum_{k'=0}^{j-k}\binom{j-k}{j-k-k'}\binom{j+k+k'}{j-m}(-1)^{k+k'} =$$

$$x^m a^{-m}\sum_{k=0}^{j-m}\binom{j}{k+m}x^k a^{-k}\sum_{k'=0}^{j-k-m}\binom{j-k-m}{j-k-m-k'}\binom{j+k+k'+m}{j-m}(-1)^{k+k'+m} =$$

$$(-1)^m x^m a^{-m}\sum_{k=0}^{j-m}\binom{j}{k+m}(-1)^k x^k a^{-k}\sum_{k'=0}^{j-k-m}\binom{j-k-m}{k'}\binom{j+m+k+k'}{j-m}(-1)^{k'} \tag{D.8}$$

Define $k'' = j-m-k-k'$, so $k' = j-m-k-k''$, giving,

$$(-1)^m x^m a^{-m}\sum_{k=0}^{j-m}\binom{j}{k+m}(-1)^k x^k a^{-k}\times$$

$$\sum_{k''=0}^{j-m-k}\binom{j-m-k}{j-m-k-k''}\binom{2j-k''}{j-m}(-1)^{j-m-k-k''} =$$

$$x^m a^{-m}(-1)^j\sum_{k=0}^{j-m}\binom{j}{k+m}x^k a^{-k}\sum_{k'=0}^{j-m-k}\binom{j-m-k}{k'}\binom{2j-k'}{j-m}(-1)^{k'} \tag{D.9}$$

We thus obtain,

$$\begin{aligned}\frac{d^{j-m}}{dx^{j-m}}(x(x+a))^j &= a^{j-m}(j-m)!x^m(x+a)^m\sum_{k=0}^{j-m}\binom{j}{k+m}x^k a^{-k}\times \\ &\quad \sum_{k'=0}^{j-m-k}\binom{j-m-k}{k'}\binom{2j-k'}{j-m}(-1)^{k'}\end{aligned} \tag{D.10}$$

Therefore, the coupling becomes,

$$\sqrt{\frac{(j+m)!}{(j-m)!}\frac{(j'+m)!}{(j'-m)!}}\frac{(-1)^n 2^n}{j!j'!}\sqrt{(2j+1)(2j'+1)}(-1)^{m+j+j'} \times$$
$$\int_0^1 du u^n (-1)^{j+m}(j-m)! \sum_{k=0}^{j-m}\binom{j}{k+m}x^k a^{-k}\sum_{k'=0}^{j-m-k}\binom{j-m-k}{k'}\binom{2j-k'}{j-m}(-1)^{k'} \times$$
$$u^m (-1)^{j'}(j'-m)!\sum_{k''=0}^{j'}\binom{j'}{k''}\binom{j'+k''}{j'-m}u^{k''}(-1)^{k''} =$$

$$\frac{(-1)^n 2^n}{j!j'!}\sqrt{(2j+1)(2j'+1)(j+m)!(j-m)!(j'+m)!(j'-m)!} \times$$
$$\int_0^1 du \sum_{k=0}^{j-m}\binom{j}{k+m}(-1)^k\sum_{k'=0}^{j-m-k}\binom{j-m-k}{k'}\binom{2j-k'}{j-m}(-1)^{k'} \times$$
$$\sum_{k''=0}^{j'}\binom{j'}{k''}\binom{j'+k''}{j'-m}(-1)^{k''}u^{k+k''+m+n} \tag{D.11}$$

and so integrating everything out gives us that,

$$\begin{aligned}\langle j', m|y^n|j,m\rangle &= \frac{(-1)^n 2^n}{j!j'!}\sqrt{(2j+1)(2j'+1)(j+m)!(j-m)!(j'+m)!(j'-m)!} \times \\ &\sum_{k=0}^{j-m}\binom{j}{k+m}(-1)^k\sum_{k'=0}^{j-m-k}\binom{j-m-k}{k'}\binom{2j-k'}{j-m}(-1)^{k'} \times \\ &\sum_{k''=0}^{j'}\binom{j'}{k''}\binom{j'+k''}{j'-m}\frac{(-1)^{k''}}{k+k''+m+n+1}\end{aligned} \tag{D.12}$$

While cumbersome, this equation is readily evaluated using MATHEMATICA.

Bibliography

[1] E. Tannenbaum, "A PDE-Based Approach to Classical Phase-Space Deformations", Phys. Rev. E (scheduled to appear in June, 2002).

[2] E. Tannenbaum and E.J. Heller, J. Phys. Chem. A **105**, 2803 (2001).

[3] M. Carioli, E.J. Heller, and K.B. Moller, J. Chem. Phys. **106**, 8564 (1997).

[4] S. Chapman, B.C. Garrett, and W.H. Miller, J. Chem. Phys. **64**, 502 (1976).

[5] O. Brodier, P. Schlagheck, and D. Ullmo, Phys. Rev. Lett. **87**, 064101 (2001).

[6] R.L. Warnock and R.D. Ruth, Physica **26D**, 1 (1987).

[7] E.J. Heller, J. Phys. Chem. **99**, 2625 (1995).

[8] R.A. Pullen and A.R. Edmonds, J. Phys. A Math. Gen. **14**, L477 (1981).

[9] C. Jaffé and P. Brumer, J. Chem. Phys. **82**, 2330 (1985); C. Jaffé, *ibid.* **88**, 7603 (1988)

[10] A.A. Stuchebrukhov and R.A. Marcus, J. Chem. Phys. **98**, 6044 (1993).

[11] N.T. Maitra and E.J. Heller, Phys. Rev. A. **54**, 4763 (1996).

[12] M. Kaasalainen and J. Binney, Phys. Rev. Lett. **73**, 2377 (1994).

[13] D.M. Leitner and P.G. Wolynes, Phys. Rev. Lett. **79**, 55 (1997).

[14] B. Ramachandran and K.G. Kay, J. Chem. Phys. **99**, 3659 (1993).

[15] E.L. Sibert III, J. Chem. Phys. **88**, 4378 (1988).

[16] E.L. Sibert III and A. B. McCoy, J. Chem. Phys. **105**, 469 (1996).

[17] R.E. Wyatt, Adv. Chem. Phys. **73**, 231 (1989).

[18] R.E. Wyatt, C. Iung, and C. Leforestier, J. Chem. Phys. **75**, 3458 (1992); **75**, 3477 (1992).

[19] S.M. Lederman and R.A. Marcus, J. Chem. Phys. **88**, 6312 (1988).

[20] S.M. Lederman, S.J. Kippenstein, and R.A. Marcus, Chem. Phys. Lett. **146**, 7 (1988).

[21] R.T. Lawton and M.S. Child, Mol. Phys. **37**, 1799 (1979); **44**, 709 (1981).

[22] M.J. Davis and E.J. Heller, J. Chem. Phys. **75**, 246 (1981).

[23] D. Farelly and T. Uzer, J. Chem. Phys. **85**, 308 (1986).

[24] A.M. Ozorio de Almeida, J. Phys. Chem. **88**, 6139 (1984).

[25] W.H. Miller, Adv. Chem. Phys. **25**, 69 (1974).

[26] Edward Ott. *Chaos in Dynamical Systems* Cambridge University Press, New York, NY, 1993.

[27] Herbert Goldstein. *Classical Mechanics:* 2^{nd} *Ed.* Addison Wesley, Reading, MA, 1980.

[28] V.I. Arnold. *Mathematical Methods of Classical Mechanics:* 2^{nd} *Ed.* Springer-Verlag, New York, NY, 1989.

[29] James E. Bayfield. *Quantum Evolution: An Introduction to Time-Dependent Quantum Mechanics.* John Wiley & Sons, Inc., New York, NY, 1999.

[30] Martin C. Gutzwiller. *Chaos in Classical and Quantum Mechanics.* Springer-Verlag, New York, NY, 1990.

[31] W.H. Press, S.A. Teukolsky, W.T. Vetterling, B.P. Flannery. *Numerical Recipes in C:* 2^{nd} *Ed.* Cambridge University Press, New York, NY, 1992.

[32] A.J. Lichtenberg and A.M. Aswani, Phys. Rev. E. **57**, 5325 (1998).

[33] G. Haller, Phys. Lett. A **200**, 34 (1995).

[34] J. von Milczewski, G.H.F. Diercksen and T. Uzer, Phys. Rev. Lett. **76**, 2890 (1996).

[35] G. Tsaur and J. Wang, Phys. Rev. E. **54**, 4657 (1996).

[36] J. DeLuca, A.J. Lichtenberg and S. Ruffo, Phys. Rev. E. **51**, 2877 (1995).

[37] D.A. Harmin, Phys. Rev. A. **56**, 232 (1997).

[38] D.A. Harmin and P.N. Price, Phys. Rev. A. **49**, 1933 (1994).

[39] W. Harshawardhan and G.S. Agarwal, Phys. Rev. A. **55**, 2165 (1997).

[40] Z. Chaoyuan and H. Nakamura, J. Chem. Phys. **106**, 2599 (1997).

[41] R. Huebner and R. Graham, Phys. Rev. B. **53**, 4870 (1996).

[42] D. Waxman, Ann. Phys. **236**, 205 (1994).

[43] A.A. Buchachenko, N.F. Stepanov, B.L. Grigorenko, and A.V. Nemukhin, J. Chem. Phys. **111**, 2470 (1999).

[44] C.C. Chuang, S.N. Tsang, W. Klemperer, and H.C. Chang, J. Chem. Phys. **109**, 8836 (1998).

[45] C.C. Chuang, K.J. Higgins, H.C. Fu, and W. Klemperer, J. Chem. Phys. **112**, 7022 (2000).

[46] C.C. Chuang and W. Klemperer, J. Chem. Phys. **113**, 4116 (2000).

[47] C.C. Chuang, S.N. Tsang, W. Klemperer, and H.C. Chang, J. Chem. Phys. **109**, 484 (1998).

[48] N. Halberstadt, P. Brechignac, J.A. Beswick, and M. Shapiro, J. Chem. Phys. **84**, 170 (1986).

[49] J.M. Hutson, J. Chem. Phys. **81**, 2357 (1983).

[50] J.M. Hutson, J. Chem. Phys. **96**, 6752 (1992).

[51] G.E. Ewing, J. Chem. Phys. **71**, 3143 (1979)

[52] D.E. Woon and T.H. Dunning, Jr., J. Chem. Phys. **98**, 1358 (1993).

[53] T.H. Dunning, Jr., J. Chem. Phys. **90**, 1007 (1989).

[54] R.A. Kendall, T.H. Dunning, Jr., and R.J. Harrison, J. Chem. Phys. **96**, 6796 (1992).

[55] R.V. Krems, N. Markovic, A.A. Buchachenko, and S. Nordholm, J. Chem. Phys. **114**, 1249 (2001).

[56] R.E. Miller, in *Structure and Dynamics of Weakly Bound Molecular Complexes*, edited by A. Weber (Reidel, Dordrecht, 1987), p. 131.

[57] P.A. Block and R.E. Miller, Chem. Phys. Lett. **226**, 317 (1994).

[58] L. Oudejans, K. Nauta, and R.E. Miller, J. Chem. Phys. **105**, 10410 (1996).

[59] B. Segev and E.J. Heller, J. Chem. Phys. **112**, 4004 (2000).

[60] J.L. Dunham, Phys. Rev. **41**, 713 (1932).

[61] J.A. Beswick and J. Jortner, Adv. Chem. Phys. **47**, 363 (1981).

[62] N. Halberstadt, S. Serna, O. Roncero, and K.C. Janda, J. Chem. Phys. **97**, 341 (1992).

[63] G.T. Fraser and A.S. Pine, J. Chem. Phys. **85**, 2502 (1986).

[64] H.C. Chang, F.M. Tao, W. Klemperer, C. Healey, and J.M. Hutson, J. Chem. Phys. **99**, 9337 (1993).

[65] H.C. Chang and W. Klemperer, Chem. Phys. Lett. **98**, 2497 (1993).

[66] C.C. Chuang, S.N. Tsang, W. Klemperer, and H.C. Chang, J. Phys. Chem. A. **101**, 6702 (1997).

[67] S.N. Tsang, C.C. Chuang, R. Mollaaghababa, W. Klemperer, and H.C. Chang, J. Chem. Phys. **105**, 4385 (1996).

[68] E.J. Bohac, M.D. Marshall, and R.E. Miller, J. Chem. Phys. **96**, 6681 (1992).

[69] C.A. Taatjes and S.R. Leone, J. Chem. Phys. **89**, 302 (1988).

[70] A.S. Pine, J. Mol. Spectrosc. **82**, 435(1980); A.S. Pine, J. Chem. Phys. **101**, 3444 (1994).

[71] C.C. Chuang, S.N. Tsang, W. Klemperer, and H.C. Chang, J. Chem. Phys. **109**, 484 (1998).

[72] F.M. Tao and W. Klemperer, J. Chem. Phys. **101**, 1129 (1994).

[73] D.T. Andersen, S. Davis, and D.J. Nesbitt, J. Chem. Phys. **105**, 4488 (1996).

[74] D.J. Nesbitt, Faraday Discuss. **97**, 1 (1994).

[75] T. van Mourik and T.H. Dunning, Jr., J. Chem. Phys. **107**, 2451 (1997).

[76] C.M. Lovejoy, M.D. Schuder, and D.J. Nesbitt, Chem. Phys. Lett. **127**, 374(1986); J. Chem. Phys. **85**, 4890 (1986).

[77] Z.S. Huang, K.W. Jucks, and R.E. Miller, J. Chem. Phys. **85**, 6905 (1986).

[78] C.M. Lovejoy and D.J. Nesbitt, J. Chem. Phys. **91**, 2790 (1989).

[79] A. McIlroy and D.J. Nesbitt, Chem. Phys. Lett. **187**, 215 (1991); J.T. Farrell, Jr., O. Sneh, A. McIlroy, A.E. Knight, and D.J. Nesbitt, J. Chem. Phys. **97**, 7967 (1992).

[80] C.M. Lovejoy, J.M. Hutson, and D.J. Nesbitt, J. Chem. Phys. **97**, 8009 (1992).

[81] A. Ernesti and J.M. Hutson, Phys. Rev. A. **51**, 239 (1995).

[82] L. Oudejans, D. Olson, and R.E. Miller, J. Chem. Phys. **105**, 8515 (1996).

[83] M.D. Schuder, C.M. Lovejoy, R. Lascola, and D.J. Nesbitt, J. Chem. Phys. **99**, 4346 (1993).

[84] J.L. McHale. *Molecular Spectroscopy.* Prentice-Hall, Upper Saddle River, NJ, 1999.

[85] J.J. Sakurai. *Modern Quantum Mechanics: Revised Ed.*. Addison-Wesley, Reading, MA, 1994.